Doctoral Dissertations                                                Graduate School

8-2017

# Electronic and Magnetic Materials Under External Stimuli

Kenneth Robert O'Neal
*University of Tennessee, Knoxville*, koneal5@vols.utk.edu

### Recommended Citation

To the Graduate Council:

I am submitting herewith a dissertation written by Kenneth Robert O'Neal entitled "Electronic and Magnetic Materials Under External Stimuli." I have examined the final electronic copy of this dissertation for form and content and recommend that it be accepted in partial fulfillment of the requirements for the degree of Doctor of Philosophy, with a major in Chemistry.

<div align="right">Janice L. Musfeldt, Major Professor</div>

We have read this dissertation and recommend its acceptance:

Charles Feigerle, David Jenkins, Veerle Keppens

<div align="right">Accepted for the Council:

<u>Dixie L. Thompson</u>

Vice Provost and Dean of the Graduate School</div>

(Original signatures are on file with official student records.)

# Electronic and Magnetic Materials

# Under External Stimuli

A Dissertation Presented for the

Doctor of Philosophy

Degree

The University of Tennessee, Knoxville

Kenneth Robert O'Neal

August 2017

# Acknowledgments

First and foremost I wish to thank my advisor, Professor Janice L. Musfeldt, for guiding me to become a stronger scientist by teaching me spectroscopy, discussing problems, and pushing me to do my best. You have been a big influence on both my personal and professional development.

I am grateful to Professors Charles Feigerle, David Jenkins, and Veerle Keppens for serving on my committee, as well as for all of their interest, help, and advice.

I wish to acknowledge all the members of our research group: Dipanjan Mazumdar, Judy Cherian, Amal al-Wahish, Tatiana Brinzari, Qi Sun, Peng Chen, Brian Holinsworth, Michael Yokosuk, Amanda Clune, Kendall Hughey, Shiyu Fan, Nathan Harms, Kevin Smith, Henok Mikre, Lakenzie Crawford, Joshua Bleu Wright, and Brandon Chapman for their help, encouragement, and collaboration. I am grateful to all the faculty and staff of the Chemistry Department who shared their knowledge with me and helped in a variety of ways during my graduate program.

I would also like to thank Jonathan Patete, Jacqueline Smith, Nara Lee, Sang-Wook Cheong, Stanislaus Wong, Carlos Marques, Megan Aronson, Zhenxian Liu, Joel Miller, Randy Fishman, Chunli Ma, Santanab Giri, John Schlueter, Qian Wang, Puru Jena, Alla Zak, Reshef Tenne, Jian Zhou, Mark Turnbull, Chris Landee, Zhiguo Chen, Peter Peterson, Kimberly Carreiro, Jamie Manosn, Myung-Hwan Whangbo, Zhiqiang Li, Jun Hee Lee, and M. Kim for their excellent collaboration during these years.

Finally, I thank my parents, family, and friends for always believing in and supporting me. I could not have finished my degree without your help, patience, and understanding.

# Abstract

The interaction between spin, charge, and lattice degrees of freedom leads to exotic and useful properties in multifunctional materials. This delicate balance of energy scales allows external stimuli such as temperature, magnetic field, or pressure to drive to novel phases. As a local probe technique, spectroscopy can provide insight into the microscopic mechanism of the phase transitions. In this dissertation I present spectroscopic studies of functional materials under extreme conditions.

Nanomaterials have attracted attention because nanoscale confinement affects various material properties and often reduces energy scales or suppress phase transitions. Combining Raman and infrared spectroscopies reveals that the breakdown mechanism of tungsten disulfide nanowires, a dichalcogenide widely used as a solid state lubricant, under compression is mainly driven by a breathing mode as revealed by its high sensitivity to compression. The optical properties of nanoscale hematite, a model antiferromagnet, reveal a size-dependent vibronic coupling behind the activation of the iron on-site excitation. Moreover, spin-charge coupling is enhanced below a critical size until the superparamagnetic limit is reached.

Molecule-based magnets offer opportunities to probe coupling processes due to their soft lattices and overall low energy scales. As an example, I reveal how the antiferromagnetic to ferromagnetic crossover of a copper halide coordination polymer originates from the formation of hydrogen bonds with applied pressure that increase the dimensionality of the copper-copper magnetic superexchange network.

Finally, combining temperature and pressure spectroscopy techniques with theoretical calculations of manganese dicyanimide revealed a temperature-pressure-magnetic field phase diagram that contains many competing magnetoelastic phases, and indicates possible quantum behavior despite the typical classical treatment of Mn(II). Together, these studies provide insight on structure-property relations, spin-charge-lattice coupling, and phase transitions in nanomaterials and molecule-based magnets, and by extension higher energy scale materials like bulk oxides.

# Table of Contents

# List of Tables

# List of Figures

# Chapter 1

# Introduction: Multifunctional materials in extreme conditions

## 1.1 Phase transitions in multifunctional materials

Multifunctional materials exhibit more than one useful property, such as magnetism or electric conductivity, and are the subject of intense interdisciplinary research including chemistry, physics, and materials science. This combination of functionalities stems from coupling of the degrees of freedom, such that a change in one drives a change in another. In ferroic materials, for example, the coupling of the spin, charge, and lattice leads to technologically useful properties (Fig. 1.1). A major initiative of modern research is to understand these materials and to be able to design novel systems with exotic properties.

Exploring phase transitions can yield insight into the conditions necessary for a material to exhibit a functional property. By understanding the changes that occur within a material as a property is established, the underlying interactions can begin to be understood. Thus, probing phase transitions in many different systems is crucial to being able to design novel materials that are tailored for particular application
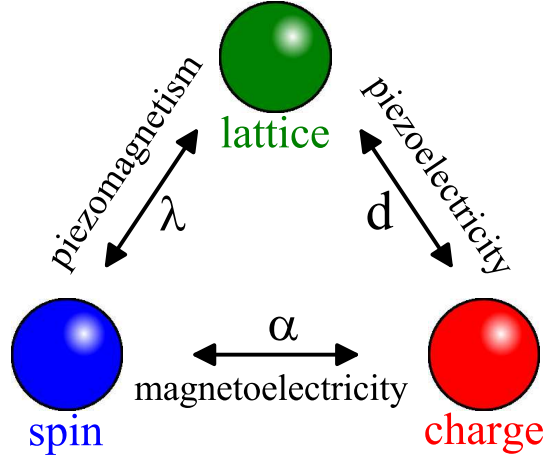
Figure 1.1: Schematic representation of spin-charge-lattice coupling in ferroic materials. Arrows represent mixing between the colored degrees of freedom and are labeled with (inside) coupling constants, $\alpha$, $\lambda$, and $d$, and (outside) the subsequent functionalities.

needs. This involves exploring materials with a variety of tuning parameters using any number of a wide range of measurement techniques depending on the material and property of interest. Table 1.1 summarizes several well-known tuning parameters and the commonly targeted phase transitions. Below, we discuss a few of the external stimuli pertinent to this dissertation.

One way to control a material is by applying an external stimulus, the most common of which is temperature. Lowering the temperature of a system reduces thermal fluctuations and can allow for new phases to emerge. In these cases typical thermodynamic rules apply. Superconductivity and long-range magnetic ordering are

Table 1.1: Common tuning parameters and representative phase transitions than can be explored.

| tuning parameter | phase transitions of interest |
|---|---|
| temperature | magnetic ordering, ferroelectricity, superconductivity |
| magnetic field | spin-flop, metamagnetic, quantum phase transition |
| pressure | structural transition, spin crossover, metallization |
| chemical doping | superconductivity, magnetic ordering |
| confinement | collective phase transitions, emergent properties |

prime examples. Each material has its own energy scales due to the strength of the intrinsic interactions, resulting in different critical temperatures. This dependence can be easily observed by comparing the drastically different Néel temperatures of $Ni_3TeO_6$ (55 K) [1] and $\alpha$-$Fe_2O_3$ (955 K) or the superconducting temperatures of $MgB_2$ (39 K) [2] and $YBa_2Cu_3O_7$ (93 K). [3] Moreover, structural crossovers, ferroelectricity, and superconductivity can be explored with temperature as an external stimulus. When combined with other probes, variable temperature measurement through a transition can also help to unveil the underlying microscopic mechanism. For instance, vibrational spectroscopy can be used to reveal spin-lattice coupling through magnetic ordering transitions, [4, 5] changes in hydrogen bond strengths at low temperature, [6] and the driving phonons of the spin-Peierls transition. [7–9] Temperature is therefore a vital tuning parameter in multifunctional materials.

One type of phase transition that has drawn much attention and is important to this dissertation is the quantum phase transition. Here, the transition is driven by an external tuning parameter $g$ (Fig. 1.2) as compared to a classical phase transition governed by thermal fluctuations [10, 11] These transitions often occur at very low temperatures such that thermal fluctuations are negligible. [12] Examples include the metal-insulator transitions in organic and oxide materials [13–16], superconductivity, [17–19] and magnetic field-induced quantum paramagnetism. [20, 21] These systems are particularly interesting due to the exotic properties that emerge near the quantum critical point, where delicately balanced energy scales leads to competition of phases with different properties.

Magnetic field also drives novel phase transitions. When a field is applied to a magnetic material, the spins can be driven into new microscopic arrangements. Antiferromagnets and ferrimagnets can display exotic phase transitions, such as the spin-flops in $\alpha$-$Fe_2O_3$ and $Ni_3TeO_6$ where the spins spontaneously reorient due to
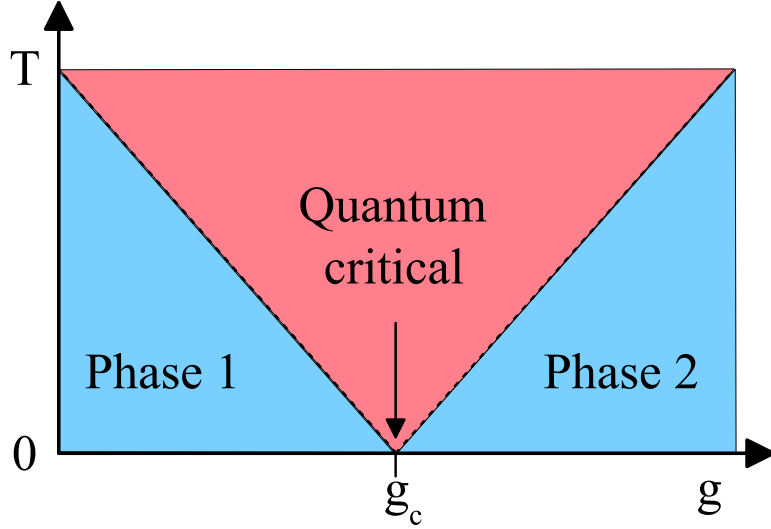
Figure 1.2: Schematic temperature-$g$ phase diagram, where $g$ represents an external tuning parameter such as magnetic field or pressure. The quantum phase transition occurs at $g = g_c$ and $T = 0$, with dashed lines indicating a crossover (after Ref. 22).

anisotropy. [23,24] Geometrically frustrated magnetic systems, such as the triangular lattice antiferromagnets $RbFe(MoO_4)_2$ and $CsFe(SO_4)_2$, can display many novel spin states before the spins fully saturate along the field direction. [25, 26] When field is applied at very low temperatures, a quantum phase transition to the fully polarized state may occur. [20, 21] By contrast, in paramagnetic or ferromagnetic systems this occurs continuously. Investigating these various field-driven transitions reveals the intrinsic interactions underlying magnetic ordering and allows for design of novel magnetic materials.

Pressure is a unique tuning parameter in that it directly changes bond lengths and angles, directly affecting orbital overlaps and therefore many properties. For example, the ferroelectric polarization of $TbMnO_3$ changes direction and increases an order of magnitude under compression, [27] and $[Ru_2(O_2CMe)_4]_3[Cr(CN)_6]$ displays a pressure-induced high-to-low spin crossover. [28] Compression can be achieved in various ways, such as applying hydrostatic pressure in a diamond anvil cell or through uniaxial strain techniques. The direction of compression can be important if a mate-

rial is anisotropic, as in the layered transition metal dicalchogenides where the weak interlayer van der Waals forces offer an easy direction of volume reduction. This direct change of chemical bonding can drive structural transitions in which the overall symmetry of the crystal structure changes. Moreover, changing atomic distances and angles affects the orbital overlaps which may result in magnetic crossovers [29] or even metallization. [30–32] Compression can also drive chemical reactions within a material. [33, 34] Pressure-induced transitions therefore give insight into chemical bonding and inter-atomic interactions.

## 1.2    Emergent phenomena at small sizes

One important tuning parameter that is relatively new is nanoscale confinement. Some phenomena, like magnetism, arise from the periodicity of an extended crystal structure. These long-range properties can be disrupted if a system is not large enough for the interactions to be fully expressed. Synthetic techniques have advanced to the point where controlled sizes and shapes of crystalline particles can be produced. Studying particles of various sizes allows these so-called "finite length scale effects" to be revealed. Important length and energy scales are typically robust (remaining bulk-like) as particle size is reduced until the nanoscale regime. Within this region the properties are heavily dependent on the size and shape of a nanoparticle. Such confinement effects are typically modeled with a $\frac{1}{r^2}$ size dependence where $r$ is the nanoparticle radius, meaning that changes are much stronger as size is decreased. Such effects include reduced energy scales like magnetic ordering temperatures and critical magnetic fields, [35–37] phonon frequencies, [38–40] and melting temperatures. [41, 42] Beyond simply reducing energy scales, quantum confinement can also change the ground state of a system. The most common example of this is superparamagnetism in magnetic nanoparticles, in which thermal fluctuations are strong

enough to force the magnetic moment flip direction randomly. This novel form of magnetism only appears below a critical length scale that is different for each material. [43, 44] Nanoscale confinement is therefore a powerful route by which to tune a material and explore new phases for exotic properties.

## 1.3  Combining tuning parameters to explore phase space

While each of the above tuning parameters can expose new phases, combining two or more together permits exploration of a wider area of phase space. This opens the door to probe many more phases which may exhibit unique properties. Molecule-based magnets, for instance, often have rich temperature-pressure-magnetic field phase diagrams that can be explored at experimentally realizable energy scales. [28, 45, 46] This allows many phase transitions to be explore within the same materials, giving a broader and deeper understanding of the intrinsic interactions and how to modify them to suit application needs.

In this dissertation, I discuss the properties of several materials under extreme conditions as probed via various spectroscopies. These include $WS_2$ nanotubes, nanoscale $\alpha$-$Fe_2O_3$, $CuF_2(H_2O)_2$(3-chloropyridine), and $Mn[N(CN)_2]_2$. The scientific questions focus on revealing the mechanisms behind various externally-driven phase transitions. Table 1.2 summarizes our findings, which we discuss briefly below.

Transition metal dichalcogenides attract interest due to their exotic properties and demonstrated applications. [47–52] Nanotubes and nanoparticles of these materials are well-known to display superior mechanical stability [53] and solid-state lubrication properties [54–56] that have led to their commercial availability, wide industrial use, and potential future applications. [57–60] Under high shearing rates,

Table 1.2: Summary of the scientific problems and important findings in this dissertation.

| Material | Scientific Problem | Our Findings |
|---|---|---|
| WS$_2$ nanotubes | • Pressure-induced breakdown mechanism of nanotubes <br> • Electronic properties under compression | • A$_{1g}$ breathing mode is main pathway of nanotube breakdown <br> • Nanotubes fracture from outside-in <br> • Nanotubes display weak conductivity at ambient conditions <br> • Hopping barrier estimation of 350 cm$^{-1}$ based on percolation model |
| $\alpha$-Fe$_2$O$_3$ nanoparticles | • Confinement effects on vibronic coupling <br> • Spin-charge coupling at small size <br> • Size dependence of collective excitations | • Vibronic coupling crossover due to dimensionality of mode displacement <br> • Enhanced magnetoelectric coupling above superparamagnetic limit <br> • Magnon sideband softens with reduced size <br> • Both magnon and exciton soften at small size, although exciton is more sensitive |
| Cu-3ClPyd | • Microscopic mechanism of antiferromagnet-to-ferromagnetic crossover under compression | • Magnetic crossover driven by reversible formation of Cl$\cdots$H$_2$O hydrogen bonding <br> • Structural transition discovered between 4-5.5 GPa mainly involving Cu bipyrimidal environment |
| Mn[N(CN)$_2$]$_2$ | • Exchange anisotropy development under compression <br> • Magnetic properties of high pressure $\delta$ phase | • Develop magneto-structural phase diagram containing many quantum phases <br> • Mn(II) should be reconsidered as a building block of quantum materials |

Cu-3ClPyd = CuF$_2$(H$_2$O)$_2$(3-chloropyridine)
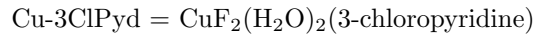
however, the tubes and particles begin to deform and exfoliate. [59, 61] Using high pressure spectroscopies of $WS_2$ nanotubes we find that the $A_{1g}$ vibration is twice as pressure sensitive as the other features, making the displacement a strong candidate for driving the nanotube breakdown. At the same time, the electronic properties of the transition metal dichalcogenides are of fundamental and practical importance. [52, 62–73] We also discover the development of a localized absorption under pressure that points to modest conductivity above the percolation limit.

We identified $\alpha$-$Fe_2O_3$, commonly known as hematite [74–77], as a model antiferromagnetic system with which to reach beyond temperature, magnetic field, and pressure tuning of color band activation [78–80] to investigate size and shape effects. We discover finite length scale effects on vibronic coupling in $\alpha$-$Fe_2O_3$ and a crossover in the coupling phonon frequency that is driven by a change in the dimensionality of the displacement pattern. Analysis reveals that the mode character becomes more three-dimensional with decreasing size. We confirm these findings and uncover a two-state mixing process at intermediate sizes via direct vibrational property measurements and comparison with prior lattice dynamics calculations [81]. We also find enhanced spin-charge coupling as indicated by the magnetic field-induced absorption difference of the $d - d$ excitation, and reveal size effects on collective excitations.

$CuF_2(H_2O)_2$(3-chloropyridine) attracted our attention due to its pentacoordinate copper environment, two-dimensional hydrogen bonding network, and pressure-induced magnetic transition. [82, 83] This system is fully molecular rather than being covalently bound. Moreover, it displays a buckled network of intermolecular hydrogen bonds between the $H_2O$ ligands and fluoride centers that act as superexchange linkages between the copper centers within the $ab$ plane. This network facilitates antiferromagnetic ordering below 2.1 K. [82] There is evidence that the system displays ferromagnetic behavior under pressure (0.8 GPa). [83] By combining diamond anvil

cell techniques, high pressure infrared and Raman spectroscopies, and complimentary calculations of energy, local structure trends, and lattice dynamics, we uncover the ability of hydrogen bond formation to trigger the antiferromagnetic to ferromagnetic crossover in $CuF_2(H_2O)_2$(3-chloropyridine). Our analysis reveals that compression enhances the in-plane $F^{...}$H-O exchange and creates new intermolecular hydrogen bonds between chlorine on the pyridine ring and the hydrogen centers on the water ligands. The latter pathway forms because compression reduces inter-atomic distances, aligns the Cl-containing ring, and widens the $H_2O$ ligands, leading to a three dimensional hydrogen bonding network between copper centers. This increased superexchange network dimensionality drives the 0.8 GPa magnetic crossover and is reversible, meaning that when pressure is released, the extra exchange pathway is eliminated. Further compression reveals another distortion between 4 and 5.5 GPa involving the bipyramidal copper environment although, at this time, it is not known whether there is a magnetic component.

The interplay between charge, structure, and magnetism gives rise to rich phase diagrams in complex materials with exotic properties emerging when phases compete. Molecule-based materials are particularly advantageous in this regard due to their low energy scales, chemical tunabilty, and flexible lattices. Here, we bring together high-pressure Raman spectroscopy, modeling, and first-principles calculations to reveal the pressure-temperature-magnetic field phase diagram of $Mn[N(CN)_2]_2$. We uncover how hidden soft modes drive two pressure-induced transitions with implications for magnetism, including a unique reorientation of exchange planes. These magnetoelastic transitions and their mechanisms highlight the importance of spin-lattice interactions in establishing phases with novel magnetic properties. Moreover, we discuss the possibility of quantum behavior in this and other Mn(II)-containing systems despite the usual semi-classical character of the high-spin ion.

The remainder of this dissertation is organized as follows: Chapter 2 presents a literature survey of coupling processes in condensed matter and the materials of interest. Chapter 3 summarizes the basics of spectroscopy, experimental techniques, and sample preparation characterization. Chapter 4 presents the high pressure spectroscopic study of the $WS_2$ nanotube breakdown mechanism and electronic properties. Chapter 5 details our investigation of confinement effects in $\alpha$-$Fe_2O_3$ nanoparticles with a focus on coupling processes and collective excitations. Chapter 6 is devoted to probing the microscopic mechanism of the pressure-induced antiferromagnetic to ferromagnetic crossover in $CuF_2(H_2O)_2$(3-chloropyridine). Chapter 7 contains our work on $Mn[N(CN)_2]_2$ in which we produce the three-dimensional phase diagram to understand the magnetic properties of the high pressure phases. Finally, Chapter 8 summarizes and presents scientific extensions of the findings.

# Chapter 2

# Literature survey

## 2.1 Confinement effects in nanomaterials

Nanomaterials are the subject of sustained research due to the novel properties that emerge at the nanoscale. Within this ever-growing class of materials, those containing iron stand out in particular due to the high natural abundance of iron and their variety of magnetic properties. [84–87] One of the main advantages of magnetic nanoparticles is that changing the particle size can greatly affect the basic material properties. These effects are referred to by a few terms including quantum (or nanoscale) confinement or finite size effects, manifest in a variety of ways, and are most often studied in chemically simple systems. Even the most basic of material properties can be affected by size. For example, the melting point of In and Zn nanowires decreases with reduced size. [41, 42] The optical properties can also be size-dependent, displaying shifting excitation energies at small length scales. [88–96] In fact, quantum confinement has widespread effects that must be more deeply understood in order to develop novel and useful multifunctional nanomaterials.

Importantly, magnetic properties are affected by finite length scale effects. [97–99] Magnetism is a long range phenomenon so reducing the length scale of system

has strong effects. As size is reduced, energy scales are typically decreased. This leads to decreased magnetic transition temperatures, such as the Néel temperature of NiO nanoparticles that drops off sharply below $\approx 15$ nm [36] or the lowering of the Morin temperature in nanoscale hematite [Fig. 2.1 (a)]. [100] Critical magnetic fields are also typically reduced, as exemplified by the spin-flop transition of oxide nanoparticles [Fig. 2.1 (a)], [100, 101] Confinement also results in increased coercive fields in $YMn_2O_{5\pm\delta}$ nanoparticles, [102] although coercivity decreases at small sizes in nano-$BiFeO_3$. [99] Below a material-dependent critical size, the system enters a novel form of magnetism in which the spins behave as one net moment that randomly changes direction called superparamagnetism. [35, 43, 44] All of these changes need to be taken into consideration when bringing a magnetic material into the nanoscale.
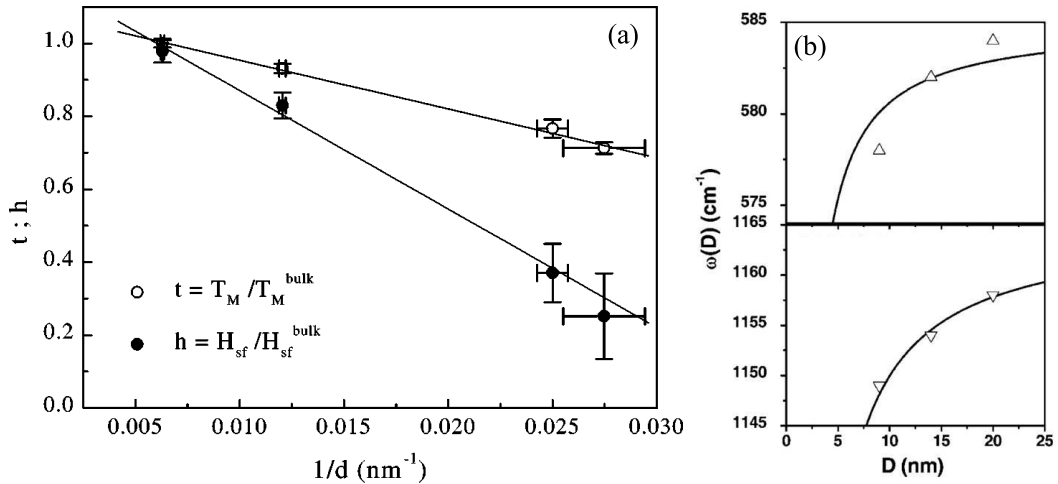


Figure 2.1: (a) Morin temperature $T_M$ and spin-flop field $H_{sf}$ of hematite nanoparticles. (b) Frequency of two Raman modes of ZnO nanoparticles. (From Refs. 100 and 103, respectively.)

The structure of a nanomaterial can differ from the bulk system too. As an example, the unit cell of nano-hematite expands anisotropically at small sizes, with the $a$ axis growing more quickly than the $c$ axis. [104] These structural changes are easily observed in the lattice dynamics which can be probed through vibrational spectroscopy. [38, 40, 105–109] Raman spectroscopy reveals that most vibrational

modes shift to lower frequency at small sizes, as in ZnO nanoparticles [Fig. 2.1 (b)]. [103] Infrared-active phonons also display finite size effects, such as the size-dependent frequency and damping of the $A_1(TO1)$ mode of $BiFeO_3$. [39] Confinement can also modifies the structural stability of a material. $Y_2O_3$ nanoparticles were shown to be more stable than their bulk counterparts, [110] while $TiO_2$ nanoparticles can be more or less compressible than bulk material depending on the particle shape. [111]

Beyond these basic material properties, finite length scale effects influence the interaction between charge, structure, and magnetism. [112, 113] Nanoscale oxides like MnO and $CoFe_2O_4$, for instance, sport modified chemical bonding, displacive transitions, and spin-lattice couplings compared to their bulk analogs. [114–116] Electron-phonon coupling in nanomaterials has also been somewhat explored. [117–119] Confinement also affects the nature of collective phase transitions, including the spin-Peierls transition in $CuGeO_3$ nanorods which is suppressed below 600 nm [37] and the ferroelectric-to-paraelectric crossover in $BiFeO_3$ nanoparticles of less than 8 nm diameter. [39] Due to the broad effects of nanoscale confinement, the microscopic mechanism of the quenching of these transitions are often ambiguous and require more in depth investigations of complex nanomaterials.

Magnetic nanoparticles already exhibit a wide variety of demonstrated applications. In biomedicine, they offer opportunities for controlled drug delivery, enhanced magnetic resonance imaging contrast, and protein purification. [87,120–124] The high surface-to-volume ratio of nanoparticles lead to enhanced catalysis and recovery of catalysts, [125–128] reducing synthesis costs. Core-shell structured nanoparticles allow materials with very different properties to be combined in a unique way. For example, combining hard and soft magnets can overcome the downfall of either parent material and provide a hybrid material that can be used in magnetic energy

13

storage. [129] Functionalized nanoparticles display superior chemical sensing abilities and their tunable length scale allows applications in previously difficult to probe environments, such as inside a cell. [130, 131] This new capability is a double-edged sword, however, since the nanoparticles can enter cells and disrupt non-targeted biological processes, [132, 133] making studies of toxicity paramount to wide-spread application of nanomaterials. [123, 134, 135]

Outside of biomedicine, magnetic nanoparticles are finding technological uses in the fields of sensing [136, 137] and spintronics. [138, 139] Graphene-nanoparticle hybrids, for example, display excellent sensitivity and selectivity in sensing molecules such as $H_2O_2$ or $NO_2$. [140, 141] Functionalized nanoparticles give rise to surface-enhanced Raman scattering, which enables single molecules to be sensed and measured. [142–144] Doped nanoscale dilute magnetic semiconductors exhibit magnetic properties that may be useful in spintronics, such as spin-valves or spin light emitting diodes. [145, 146]

### 2.1.1 Confinement effects in $\alpha$-Fe$_2$O$_3$, a model antiferromagnet

$\alpha$-Fe$_2$O$_3$, commonly referred to as hematite, is an iconic and ubiquitous antiferromagnet. It is also the chemically-simple parent compound from which many transition metal oxides stem, such as multiferroic BiFeO$_3$ and LiFe$_2$O$_4$. It is therefore critical to understand the fundamental properties and interactions of both bulk and nanoscale hematite in order to place the development of new functional oxides on a firm foundation.

The system crystallizes in a hexagonal $R\bar{3}c$ structure. [147] The system is antiferromagnetic below the 260 K Morin temperature with spins lying along the [111] axis of the trigonal unit cell. [148] Both temperature (260 K) [148] and magnetic field (6

14

or 16 T for the easy and hard axes, respectively) [149] drive a spin-flop transition to the basal place, with a small spin canting due to the Dzyaloshinsky-Moriya interaction. [150, 151] Applied pressure alters the electronic and vibrational properties of $\alpha$-$Fe_2O_3$, [80, 152–154] and drives a structural transition around 50 GPa. [155–158]

The optical spectrum of $\alpha$-$Fe_2O_3$ consists of two electronic transitions near 11,550 and 15300 cm$^{-1}$ that are assigned as $^6A_{1g} \rightarrow^4 T_{1g}$ and $^6A_{1g} \rightarrow^4 T_{2g}$ on-site excitations, respectively [Fig. 2.2 (a)]. [78] The formally forbidden $Fe^{3+}$ on-site excitation is formally forbidden, but is allowed via spin-orbit coupling, exchange interaction, and odd parity phonons that hybridize states and break inversion symmetry. [78, 160, 161] The phonon-activated character of the lower frequency $^6A_{1g} \rightarrow^4 T_{1g}$ band is indicated by the temperature-dependent oscillator strength $f$ [Fig. 2.2 (b)] that can be modeled by $f = f_0(1 + e^{-\theta/T})$, where $f_0$ is the low temperature limit of the oscillator strength, $\theta$ is the frequency of the activating phonon, and $T$ is temperature. At low temperatures, the leading edge of the lower frequency excitation displays excitons and a magnon sideband [162–164] which can be used to probe symmetry changes. [159] The field-driven spin-flop transition amplifies spectral contrast of the $Fe^{3+}$ on-site $d - d$ excitation [Fig. 2.2 (c)]. [159]

Nanoscale hematite has been the subject of continued study due to the important confinement effects. Reduced particle size hardens vibrational modes [38, 109, 167–169] as the unit cell expands anisotropically. [170] The magnon energy also increases in nanoparticles compared to the bulk, [168] although studies of size dependence within a family of similar nanoparticles are missing. The magnetic properties are also strongly modified; confinement reduces critical energy scales such as the Morin temperature [Fig. 2.3 (a,b)]. [100, 165, 171–179] In fact, the Morin transition is quenched below 8 nm. [100, 171] The spin-flop, in particular, is also subject to confinement effects. In acicular nanoparticles the spin-flop transition is absent, un-

15
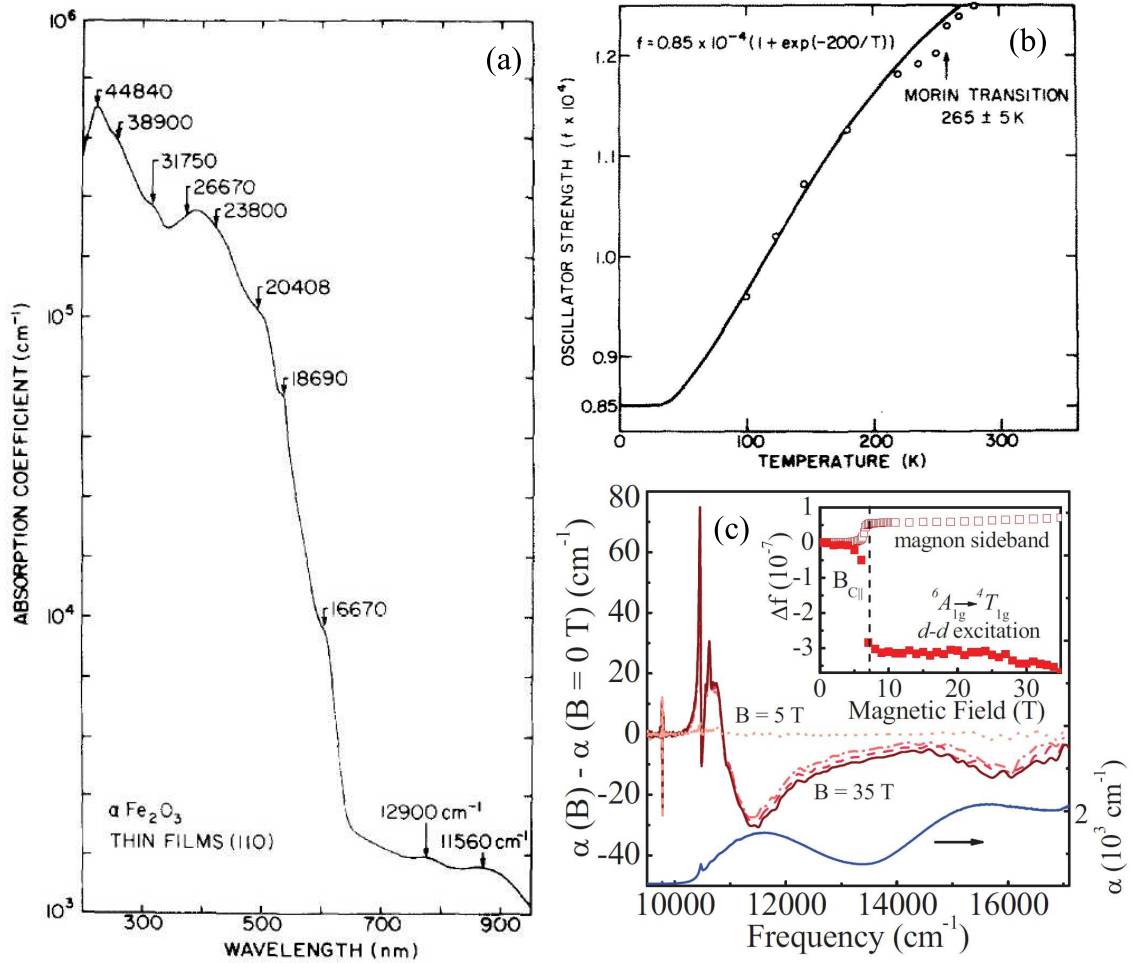
Figure 2.2: (a) Optical absorption spectrum of $\alpha$-Fe$_2$O$_3$ thin films (from Ref. 78). (b) Temperature-dependent oscillator strength of the $^6A_{1g} \rightarrow^4 T_{1g}$ color band fit to the phonon activation model (from Ref. 78). (c) (red) Magnetic field-induced absorption difference of single crystalline $\alpha$-Fe$_2$O$_3$ above the (blue) low temperature absorption spectrum. Inset: oscillator strength of the $d-d$ excitation and magnon sideband (from Ref. 159).
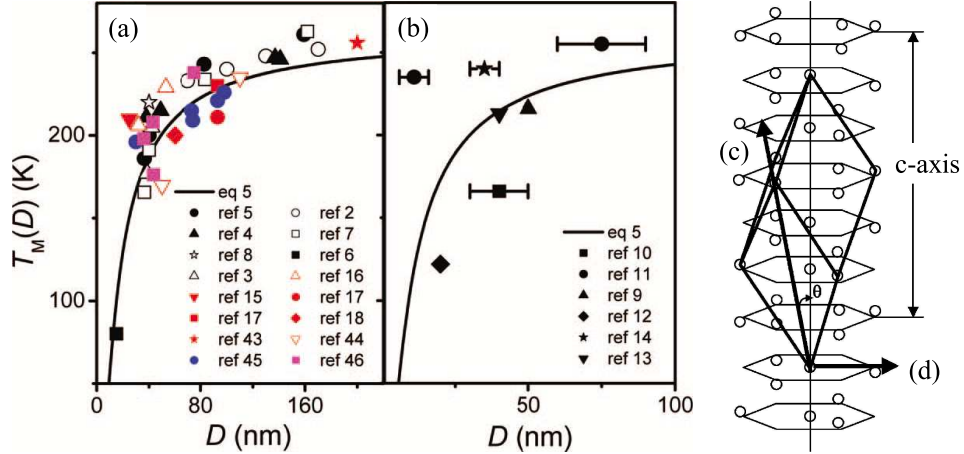
Figure 2.3: Comparison of between $T_M(D)$ for hematite (a) nanoparticles and (b) nanowires or nanorods and predictions (from Ref. 165). A proposed spin direction at $\theta = 28°$ between the (c) [110] rhombohedral and c-axis for $T < T_M$ and the (d) (111) basal plane for $T > T_M$ (from Ref. 166).

less the particles are sintered at high temperature. [180, 181] Moreover, below about 40 nm the spin-flop does not fully drive the spins to lie within the basal plain but instead to about 28° off-axis [Fig. 2.3 (c,d)]. [166] This length scale is in agreement with the onset of superparamagnetism, [176] which may explain the breakdown of the spin-flop transition.

## 2.1.2 Nanoscale transition metal dichacogenide: $WS_2$

Transition metal dichalcogenides have also attracted much attention due to the exotic electronic and tribological properties of their nano-analogs. Of particular interest is tungsten disulfide ($WS_2$). This system crystallizes in a layered $63/mmc$ structure. The unit cell contains two layers, each with W covalently bonded to six S atoms in a trigonal prismatic coordination. These layers comprise the $ab$ plane and are stacked along the $c$ direction. [182, 183] High pressure x-ray diffraction demonstrate that this structure remains stable up to 61 GPa. [184] The system can also be doped with elements such as Nb and Re. [185, 186]

Bulk $WS_2$ is a semiconductor with an indirect band gap of 1.35 eV [Fig. 2.4 (a)]. [187, 188] The vibrational properties of $WS_2$ are also well-known. The Raman response [Fig. 2.4 (b)] contains three main vibrational modes ($E_{2g}$, $B_{1u}$, and $A_{1g}$) [189] while the infrared spectrum [Fig. 2.4 (c)] contains two ($E_{1u}$ and $A_{2u}$). [190] Modes of E symmetry contain interlayer displacements while A symmetry motions are out-of-layer.
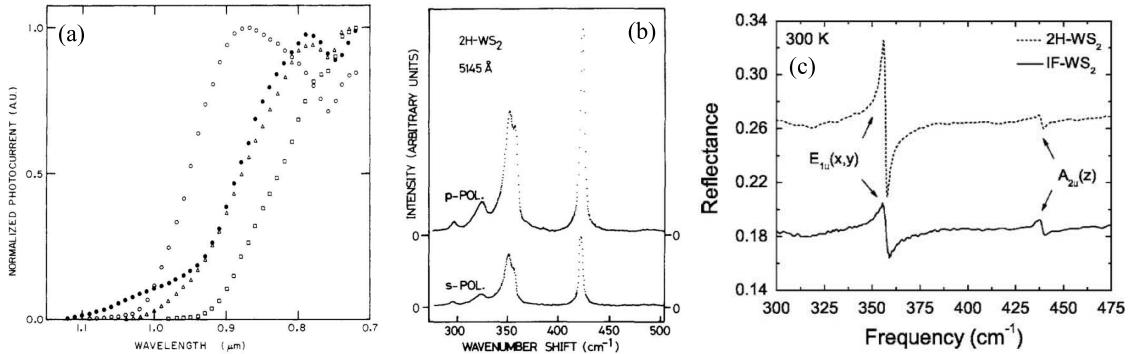


Figure 2.4: (a) Photocurrent spectra of different surfaces of $WS_2$ displaying the 1.3 eV band gap. (from Ref. 187). (a) Raman and (b) infrared spectra of $WS_2$. (from Refs. 189 and 190, respectively).

$WS_2$ has been extensively studied in nanoscale forms (nanotubes and inorganic fullerene-like nanoparticles) due to the superior mechanical stability [53] and solid state lubrication that emerges [Fig. 2.5 (a)]. [54–56] This has led to their commercial availability and wide use in power generation, heavy industry, and mining, and potential application in jet engines and medical devices. [57–60] Nanotube-reinforced polymer composites also benefit from the small tube size, modulus, and high aspect ratio, [191–193] as well as excellent dispersion and adhesion to the polymer matrix. [194] Under high shearing rates, however, the tubes and particles begin to deform and exfoliate. [59, 61] Previous theoretical and experimental studies give some insight into the lubrication and breakdown mechanisms. For instance, modeling of the nanotubes under uniaxial pressure predicts a distortion of the tubes with the innermost layer being the most strongly affected. [195] This causes a crack to
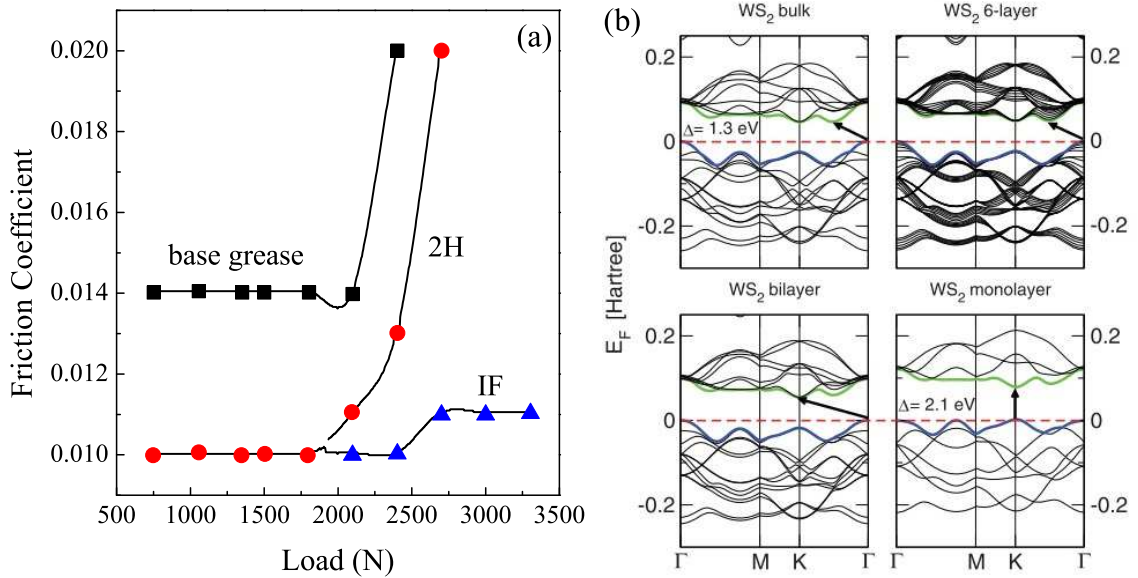
Figure 2.5: (a) Friction coefficient of base grease and grease with added 2H-MoS$_2$ platelettes and IF-WS$_2$ nanoparticles (adapted from Ref. 56). (b) Calculated band structures for various thicknesses of WS$_2$ samples (from Ref. 188).

propagate from a pinching point of the inner-most layer outward, resulting in two dimensional sheets. [195] Shock wave experiments predict a similar mechanism in nanoparticles, except with the fracture originating in the outermost layer. [196] At the same time, low temperature specific heat measurements show that long wavelength acoustic modes are blocked in these confined systems. [197] This makes the high pressure vibrational properties of transition metal dichalcogenide nanotubes of great fundamental and practical importance.

At the same time, the electronic properties of the transition metal dichalcogenides are of fundamental and practical importance. [52, 62–73] Theoretical modeling predicts a change in band gap and eventual crossover to a direct band gap upon approach to few- or single-layer form [Fig. 2.5 (b)]. [188] Predictions of band gap closure under pressure also remain to be tested. [198] For example, the pressure-induced metallization around 19 GPa due to collapse of the interlayer spacing is already demonstrated in bulk and multilayer MoS$_2$. [31, 199, 200] Bulk WS$_2$ is, by contrast, significantly

more stable and does not show distortions or metallization up to 52 GPa. [201]

## 2.2 Molecule-based magnets: Ideal platforms for investigating phase transitions

Molecule-based magnets have drawn strong interest because of their ability to be chemically tailored to exhibit a wide range of properties. [202–209] These systems are typically composed of transition metal centers connected by organic ligands, offering a wide array of building blocks. For example, the dimensionality of the magnetic superexchange network can be controlled through choice of transition metal center and ligands, exposing very different magnetic properties. [210–212] $Cu(pyz)(NO_3)_2$ (pyz = pyrazine), for example, is an excellent physical example of a one-dimensional spin-$\frac{1}{2}$ Heisenberg antiferromagnet comprised of basic organic ligands. [213] Two dimensional systems have also been discovered, such as $[Mn^{II}(TCNE)(NCMe)_2]X$ (X = $PF_6$, $AsF_6$, $SbF_6$) that display spin-glass behavior. [214] Combining organic and hydrogen bond-based ligands allows for control of dimensionality. $CuF_2(H_2O)_2(pyz)$ (pyz = pyrazine), for instance, is a two dimensional quantum magnet. $[Ni(HF_2)(pyz)_2]X$ (pyz = pyrazine; X = $PF_6$ , $SbF_6$), on the other hand, are structurally quasi-three-dimensional, but the magnetic superexchange is quasi-one-dimensional [215] demonstrating that structural and magnetic dimensionalities are not always commensurate. [216] This further proves the importance of incorporated ligands to the overall properties of a molecule-based magnet.

One main advantage of molecule-based magnets is that the energy scales are much lower as compared to conventional magnets (like oxides), allowing many exotic states and phase transitions to be explored within one system at experimentally realizable conditions. This is demonstrated best by the complex phase diagrams often exhibited

in molecule-based magnets, [217–219] such as the rich pressure-temperature-magnetic field phase diagram of $[Ru_2(O_2CMe)_4]_3[Cr(CN)_6]$. [28] While organic ligands and hydrogen bonds support magnetic superexchange, the exchange is typically not as strong as other classes of magnetic materials. This results in a lower ordering temperature, but also the ability to probe magnetic field-driven quantum phase transitions with conventional powered magnets. [20, 213, 215, 220] Moreover, the pliable organic ligands lead to critical pressures required to drive to new states. [221–224] In fact, many molecule-based magnets display structural distortions at pressures as low as 1 GPa, [225–227] whereas $\alpha$-$Fe_2O_3$ (a representative oxide) requires 54 GPa. [153] Taken together, these low energy scales make molecule-based magnets ideal systems for investigating spin-charge-lattice coupling processes.

### 2.2.1  Hydrogen bond-based $CuF_2(H_2O)_2$(3-chloropyridine)

One molecule-based magnet with various opportunities to study phase transitions is $CuF_2(H_2O)_2$(3-chloropyridine), the crystal structure of which consists of pentacoordinate $Cu^{2+}$ centers with slightly distorted trigonal bipyrimidal geometry [Fig. 2.6 (a)]. Two-dimensional layers are formed by strong intermolecular F···H-O hydrogen bonding which form the $ab$ plane and stack along the $c$ direction with 3-chloropyridine rings between them. [82] Low temperature drives a structural transition from the orthorhombic $Pnma$ space group to a monoclinic $P2_1/c$ structure between 100 and 200 K. [82] Long-range antiferromagnetic ordering appears below $T_N$=2.1 K [Fig. 2.6 (b)], and applied magnetic field drives a quantum critical transition to the fully polarized state at 25 T [Fig. 2.6 (c)]. [82] The fully molecular nature of this system allows the quantum critical transition to occur without lattice distortions, in comparison with materials combining hydrogen and covalent bonding. [228] Applied pressure drives an antiferromagnetic → ferromagnetic transition around 0.8 GPa, [83] the
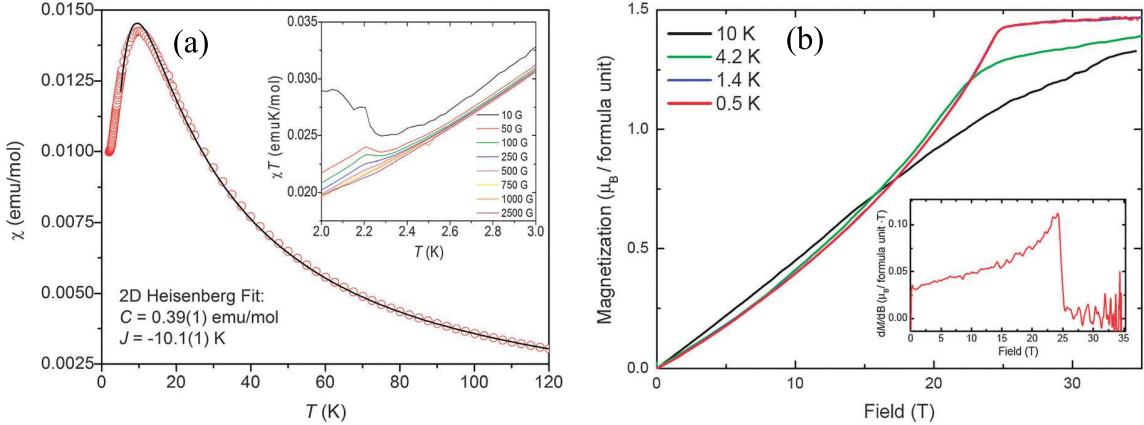
Figure 2.6: (a) Magnetization of $CuF_2(H_2O)_2$(3-chloropyridine) displaying long-range ordering below $T_N$. (b) High field magnetization exhibiting a quantum critical transition near 25 T. (from Ref. 82).

microscopic mechanism of which is unknown.

## 2.2.2 $Mn[N(CN)_2]_2$ offers opportunities to explore phase transitions

The $M[N(CN)_2]_2$ family of molecule-based magnets has been the subject of contemporary interest. [224, 229–237] $Mn[N(CN)_2]_2$, in particular, has been well-studied. [20, 45, 227, 238–241] The structure consists of Mn centers connected by dicyanamide ligands in an orthorhombic *Pnnm* structure [Fig. 2.7 (a)]. [232, 238] Below 16 K the system is a canted antiferromagnet. [233, 239–241] The temperature-pressure-field phase space of $Mn[N(CN)_2]_2$ has begun to be explored. Applied magnetic field drives a spin-flop transition around 0.5 T [241] and ultimately a quantum critical transition near 30 T. [20] The latter is accompanied by lattice distortions that lower the antiferromagnetic exchange and facilitate the fully polarized state. [20] Applied pressure causes an enhancement of the exchange anisotropy at 0.7 GPa [45] and a series of structural distortions, [227] although an unambiguous connection between the structural and magnetic changes remains undiscovered.
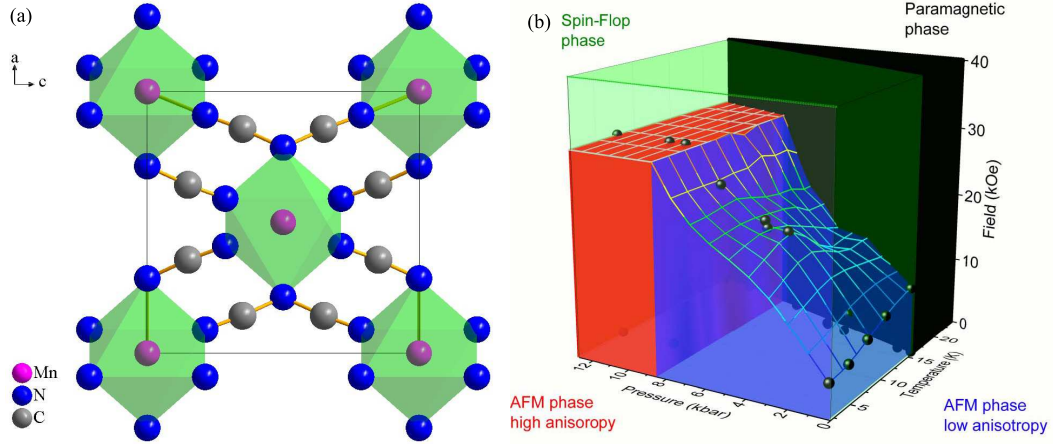
Figure 2.7: (a) Crystal structure of Mn[N(CN)$_2$]$_2$. [232] (b) Partial phase diagram exhibiting various magnetic phases (from Ref. 45).

## 2.3 Phase transitions driven by external stimuli

### 2.3.1 Phase transitions under compressions

Applied pressure to a material forces it to decrease atomic distances in order to reduce the overall volume. Pressure is therefore a unique tuning parameter since it acts directly on bond lengths and angles. Whether distances or angles change more depends on the crystal structure of the material because anisotropy may lead to a preferred direction of compression. For example, the transition metal dicalchogenides have layered structures [183] with strong interlayer bonding and weaker van der Waal's bonding between layers. This results in much greater compression along the stacking direction as compared to in-plane. [184, 201] Applied pressure can also drive structural transitions to totally new space groups when simple bond length and angle reductions do not reduce volume enough. [224, 242–244] Compression can also drive more subtle changes such as orbital reorientations [245, 246] or Jahn-Teller distortions. [225, 247]

One technique for exploring these high pressure effects is x-ray diffraction, since it directly probes the crystal structure. One downfall of this approach is that x-ray

diffraction is a bulk measurement technique. This allows the unit cell parameters and volume to be determined, [110, 184, 201, 248] but does not reveal local structure. Vibrational spectroscopy, on the other hand, is a microscopic probe used to study pressure-induced changes in local structure and symmetry. [153, 249–256] Combining these two techniques allows for a quantitative determination of structural anisotropy through calculation of the mode Grüneisen parameters of differently directed phonons. [254, 255, 257]

As applied pressure drives atoms closer together the electron orbitals overlap more and more, ultimately driving any material to a metallic state. In fact, metallization processes have already been observed in several systems. [30, 31, 258–262] The most striking example of this pressure-induced physical change occurs in hydrogen, the simplest elemental gas at ambient conditions. Even though hydrogen is an insulator with a band gap of $\approx$2 eV [263–265] it was predicted to turn metallic at pressures of 25 GPa in 1935. [266] However, as measurement techniques advance and new pressure limits are reached, metallic hydrogen remains elusive. Although it solidifies under pressure and exhibits a strikingly rich phase diagram (Fig. 2.8), [267, 268] metallic hydrogen has not been conclusively discovered up to pressures of 350 GPa. [267, 269–271]

One important note to make is that pressure can be applied in a variety of ways, leading to different effects. Compression can occur in only one direction, as in between two plates (uniaxial), or in all directions simultaneously (hydrostatic). For this reason, most high pressure experiments make use of a pressure medium to distribute forces evenly. However, not all pressure media behave the same or allow the same phase transitions. [272–274] $CuGeO_3$ undergoes a completely different series of structural transitions in a liquid medium as compared to a solid pressure medium, [275, 276] and the compressibility of zeolite 4A and titanium depend on
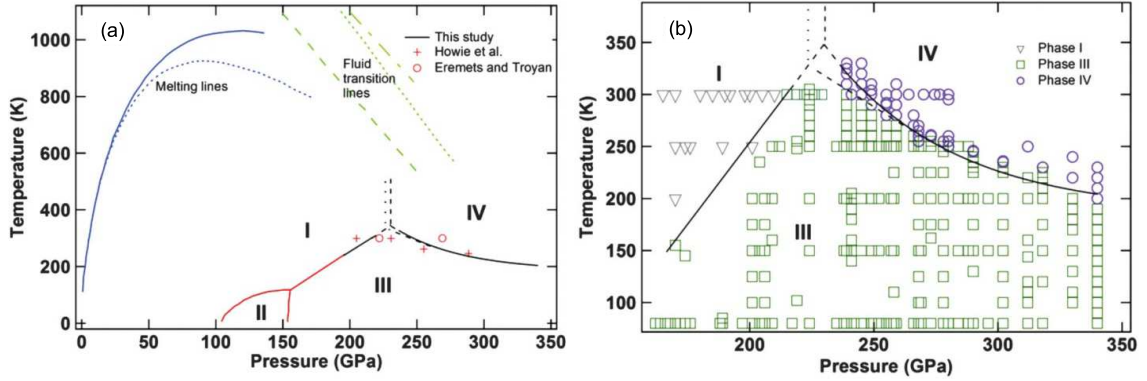
Figure 2.8: (a) Pressure-temperature phase diagram of hydrogen. (b) Close-up view of the triple point region as revealed by synchrotron-based infrared measurements (from Ref. 268).

the medium used. [277, 278] The choice of pressure medium therefore depends on the reactivity of the sample, pressure range of interest, desired hydrostaticity, and employed measurement technique.

## 2.3.2 Magnetic field-induced phase transitions

Magnetic field is another external tuning parameter that is becoming more common because of the capability to drive novel transitions. Magnetic field affects a surprising variety of properties including resistance, [279, 280] electric polarization, [24, 281] and even cause strain. [282, 283] Importantly, magnetic field affects magnetic moments, and below we discuss field-driven changes in magnetic ordering which are important to this dissertation. As magnetic field is applied, the spins are forced to align along the field direction. Depending on the magnetic ordering, this may occur gradually or through various transitions. Regardless of the type of magnetic ordering, when a large enough field is reached all spins will point along this direction and the magnetization will saturate.

Antiferromagnets and ferrimagnets sport exotic magnetic phase transitions. In these systems, the spins align in an anti-parallel fashion such that the net magnetic

25

moment is zero (antiferromagnet) or very low (ferrimagnet). One common field-induced transition exhibited by these systems is the spin-flop, where the magnetic moments change direction. [23, 24] Anisotropic exchange within the material lead to different field-induced energy changes along crystallographic directions. At a critical field, the energy along one direction overcomes its counterpart and the spins subsequently change direction. [284–286] This spin reorientation is often accompanied by changes to the surrounding lattice, [5] although structural distortions are not always required.

Antiferromagnets also sport magnetic quantum phase transitions, where the applied magnetic field drives the spins to the fully polarized state. This is often facilitated by lattice distortions that reduce antiferromagnetic exchange, [220, 235, 287] such as pyrazine ring buckling in $Cu(pyrazine)(NO_3)_2$, [21] and pyrazine and $HF_2^-$ modifications in $[Ni(HF_2)(pyrazine)_2]SbF_6$ [Fig. 2.9 (a,b)]. [46] These distortion track the magnetization squared [Fig. 2.9 (c)], [288] demonstrating the intimate coupling of spin and lattice in these systems. However, when magnetic superexchange occurs only through hydrogen bonding the lattice is not required to distort. [228]

Geometrically frustrated antiferromagnets often display much more complex magnetic transitions. Antiferromagnetically ordered spins do not easily map onto a triangular lattice. While there are configurations in which the net moment is zero, the spins experience "frustration". This can lead to steps in the magnetization as the moments are forced to align. $RbFe(MoO_4)_2$ and $CsFe(SO_4)_2$ [Fig. 2.10 (a,b)], for instance, display a plateau at one-third of the total magnetization where the spins lock into a stable configuration until a higher critical field is reached [Fig. 2.10 (c)]. [25] These systems therefore offer unique opportunities to investigate magnetic phase transitions.

26
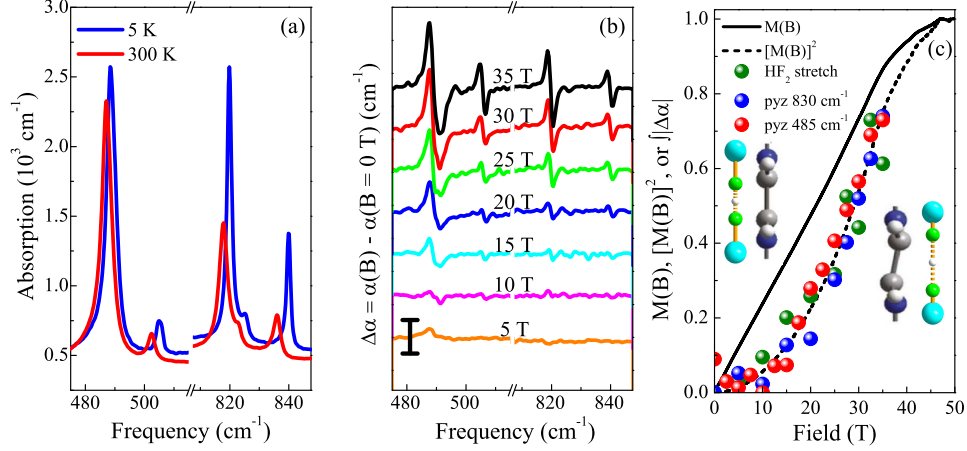
Figure 2.9: (a) Close-up view of the 300 and 5 K infrared absorption spectra of $[Ni(HF_2)(pyz)_2]SbF_6$ for the pyrazine out-of-plane mode. (b) Magnetic field-induced absorption differences for the pyrazine features. Scale bar represents 500 cm$^{-1}$. (c) Comparison of integrated absorption difference to magnetization [215] and magnetization squared. These quantities are normalized in order to draw comparisons. Insets are the $HF_2^-$ and pyrazine ring in the (left) low field and (right) distorted high field states to emphasize the field-induced changes (from Ref. 289).
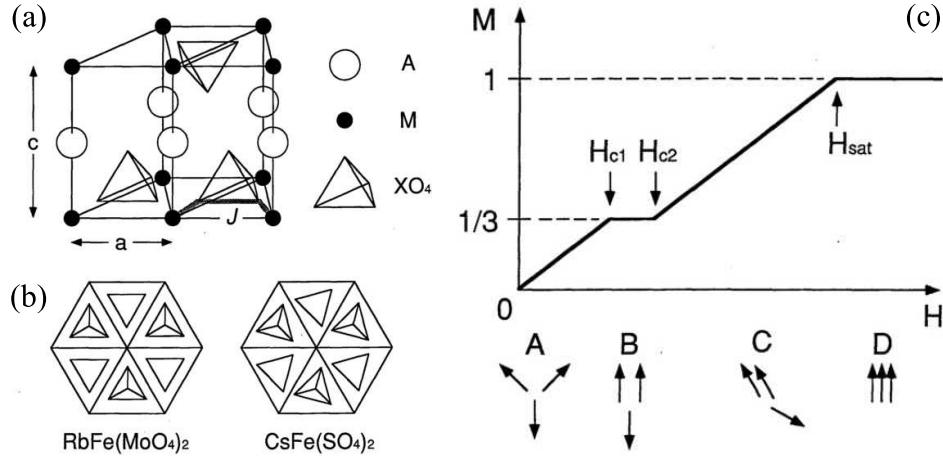


Figure 2.10: (a) Crystal structure of $RbFe(MoO_4)_2$ ($A$ = Rb, $M$ = Fe, $X$ = Mo). (b) Schematic [001] view of $RbFe(MoO_4)_2$ and $CsFe(SO_4)_2$. (c) Schematic magnetization curve for a Heisenberg two-dimensional triangular lattice antiferromagnet with weak Ising anisotropy (from Ref. 25).

27

# Chapter 3

# Experimental and theoretical techniques

## 3.1 Spectroscopy

Spectroscopy is the study of light's interaction with matter. It is a microscopic probe of the vibrational and electronic properties of a material. While spectroscopy is often used as a basic characterization method, advanced spectroscopic techniques can unveil important material chemistry. Vibrational spectroscopies (infrared and its complement, Raman) can be combined with analyses of vibrational mode trends and displacement patterns to reveal local symmetry changes, [236, 244] phase transition mechanisms, [290] and coupling constants. [4, 5] Optical spectroscopies, on the other hand, explore electronic properties such as band gaps, [291–293] electronic excitations, [78, 159, 294] and lifetimes. [295, 296] Spectroscopy is, therefore, an ideal probe with which to study phase transitions in multifunctional materials.

### 3.1.1 Infrared measurements

Infrared measurements were performed in-house on a suite of spectrometers (Fig. 3.1) covering a broad range of frequencies (20-55,000 cm$^{-1}$) with overlapping energy windows such that spectra can be merged. Far infrared measurements (20-700 cm$^{-1}$) were carried out using a Bruker 113v Fourier transform spectrometer. This system operates under vacuum to reduce atmospheric noise and employs a liquid helium-cooled bolometer for increased sensitivity. A Bruker Equinox 55 with IR Scope II attachment covers the middle infrared through visible region (600-17,000 cm$^{-1}$). This Fourier transform instrument utilizes various combinations of sources, beamsplitters, and detectors to select the region of interest. Visible through ultraviolet wavelengths (3500-55,000 cm$^{-1}$) are probed by a Perkin Elmer Lambda-900 grating spectrometer. Source, grating, filter, and detector changes are automatically chosen as appropriate for the energy range measured. Together, this suite of instrumentation allows for spectroscopic investigation of materials over a very broad frequency range.



Figure 3.1: Infrared spectrometers employed for work presented here. (a) Bruker 113v and (b) Bruker Equinox 55 Fourier transform spectrometers, and (c) Perkin Elmer Lambda-900 grating spectrometer.

### 3.1.2 Raman measurements

Raman measurements were carried out with a custom-built micro-Raman spectrometer. A 532 nm diode-pumped solid state laser was used as an excitation source,

typically with power below 1 mW to prevent sample degradation. Measurements were carried out in the backscattering geometry using 1800 groove per millimeter grating and a liquid nitrogen-cooled charge coupled device detector. Spectra were integrated up to 90 s and averaged up to 5 times to improve the signal-to-noise ratio, as needed.

## 3.2 Spectroscopy in extreme conditions

### 3.2.1 Variable temperature techniques

Samples are loaded into dynamically vacuumed cryostats for variable temperature measurements, with both transmittance and reflectance configurations available. Each cryostat is paired with a spectrometer and has windows that transmit light in the appropriate energy range. A transfer line connects a liquid helium dewar to the cryostat. Temperature control is achieved via adjustment of helium flow rate a heater housed inside the cryostat. Flow rate is controlled with flow meters, a needle valve at the tip of the transfer line, and pressure inside the liquid helium dewar, while the heater output can be controlled digitally. This combination allows for measurements at stable temperatures over a very wide range (4.2-700 K).

### 3.2.2 High magnetic field

Spectroscopic measurements in an applied magnetic field are performed at the National High Magnetic Field Laboratory in Tallahassee, FL and Los Alamos, NM. Stable, continuous magnetic field of up to 35 T can be applied using the resistive magnet setup. Control of field is achieved through varying the current running through the magnet coils and is controlled electronically as desired. Samples are mounted within a probe that is placed inside a liquid helium dewar and passes through the bore of

the magnet. For infrared measurements (20-4000 cm$^{-1}$), light is guided from the spectrometer down the length of the probe via standard optics and is collected with a bolometer detector. Fiber optic cables are used to both bring light through the probe and collect light transmitted through the sample for visible and ultraviolet measurements. Magnetic field-induced changes are typically small, such that absorption difference spectra $\Delta\alpha = \alpha(B) - \alpha(B = 0 \ T)$ are calculated to emphasize them.

### 3.2.3 Diamond anvil cell techniques

Diamond anvil cells are used for high pressure vibrational spectroscopic measurements. As summarized in Fig. 3.2, the setup consists of a metal gasket between two 5 $\mu$m diamond faces. In order to reduce background signal, Type II diamonds are used for infrared measurements, and Type I diamonds with ultra-low fluorescence are employed for Raman. The gasket has a hole drilled through the center (typically about 200 nm diameter) that houses the sample and allows light to pass through. The sizes of both the diamond culets and gasket hole determine the maximum pressure that can be applied. Four screws are turned to drive the diamonds closer together which compresses the sample. Having multiple screws reduces the chance of pressure concentrating in one area and cracking the diamonds. Note that pressure is changed *in situ* but step-wise, such that spectra are taken at a fixed pressure. Release of pressure can be achieved by loosening the screws. Spectra can then be taken upon decompression to look for reversibility of phase transitions by comparing with spectra taken before compression.

Polycrystalline samples are loaded into the cells either neat or with a pressure medium (vacuum grease for far infrared, KBr for middle infrared, or liquid argon) for measurements. The inclusion of a transparent pressure medium helps to ensure that
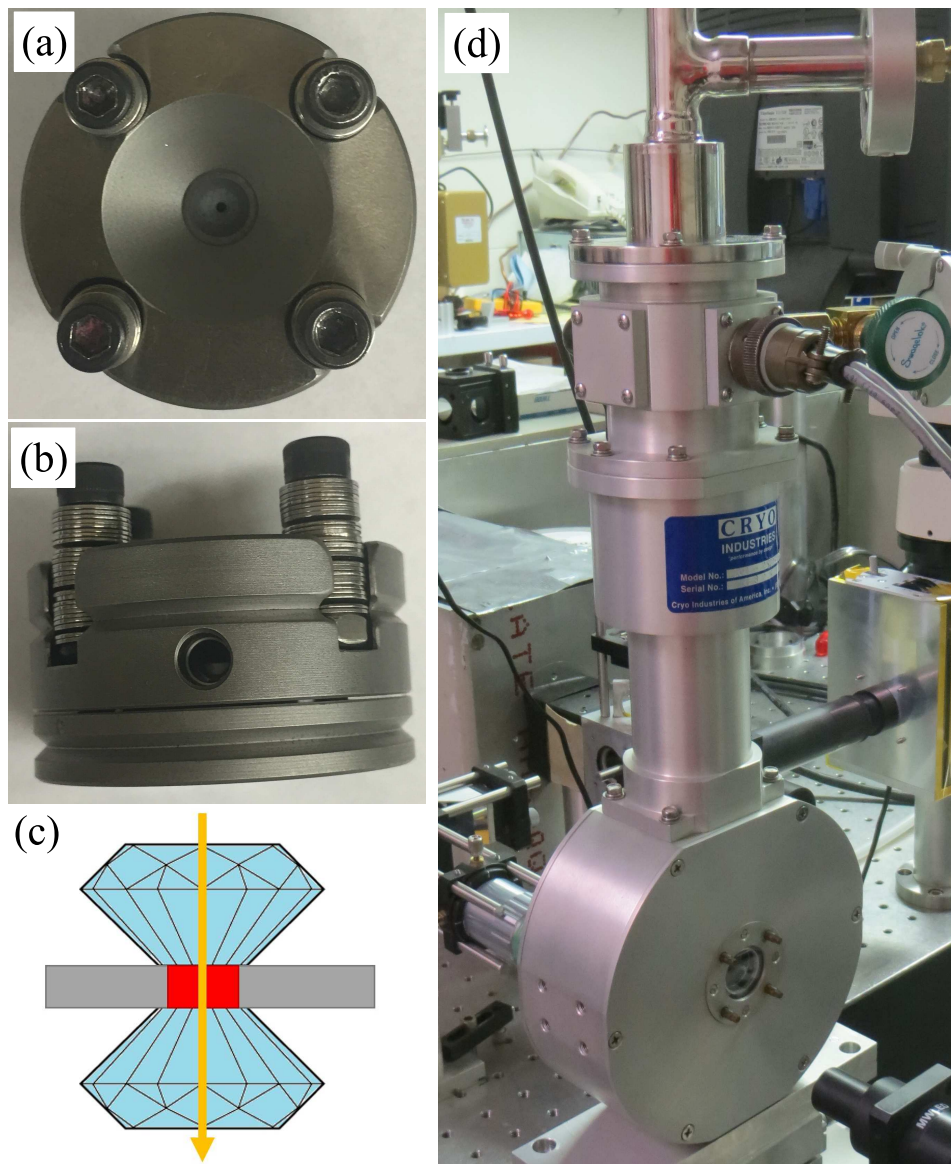
Figure 3.2: (a,b) Pictures and (c) schematic representation of a diamond anvil cell. (d) Cryostat used for low temperature, high pressure measurements.

the applied pressure is quasi-hydrostatic. This helps to make results reproducible and avoid non-linearities. Fluorescence of an annealed ruby ball inside the diamond anvil cell is used to measure the pressure. [297] This is achieved by measuring the $R_1$ fluorescence line at each pressure, since it has a well-known linear dependence between wavelength and applied pressure. Due to the small sample size and 500 $\mu$m diamond culets, the National Synchrotron Light Source (II) at Brookhaven National Laboratory is used for its high brightness infrared light. [298] Far infrared measurements (100-700 cm$^{-1}$, 1 cm$^{-1}$ resolution) combine synchrotron radiation with a helium-cooled bolometer detector and mylar-coated germanium beamsplitter. Middle infrared measurements (600-4000 cm$^{-1}$, 1 cm$^{-1}$ resolution) are taken on a Bruker Hyperion spectrometer with microscope attachment using a Globar source and MCT detector. The in-house Bruker Equinox 55 with IRScope II discussed earlier can also be used to measure high pressure spectra. Raman measurements are performed with a 532 nm diode-pumped solid state laser, with power typically below 1 mW to prevent sample degradation, and a liquid nitrogen cooled charge coupled device detector. Raman spectra (50-4000 cm$^{-1}$) are taken using an 1800 line per mm grating, integrated up to 120 seconds, and averaged as needed to improve the signal-to-noise ratio.

A custom cryostat [Fig. 3.2 (d)] houses the diamond anvil cell for low temperature, high pressure measurements. The cryostat can be used in either the Raman or far-infrared configurations. The cryostat is dynamically vacuumed and cooled with liquid helium. Due to the thermal contact of the mechanism for turning the screws inside the cryostat the lowest available temperature is ≈80 K. At low temperature the dynamics of the experimental system are slowed. This means that after turning the screws to apply pressure it is best to wait a minute or so before measuring, as the pressure can drift. Another drawback of working at low temperature is that

releasing pressure can be difficult. The system may need to be warmed back to room temperature in order to achieve ambient pressure. While this is often not a major issue, the possible thermal cycling needs to be considered for samples with thermal transitions with broad hysteresis. When properly used, this setup allows low temperature, pressure-driven phase transitions to be explored or regions of phase space to be mapped out.

## 3.3 Material synthesis and complementary calculations

### 3.3.1 WS$_2$ nanotubes

#### *Nanotube growth*

WS$_2$ nanotubes were synthesized by a bottom-up solid-gas reaction by Alla Zak at the Holon Institute of Technology. [299] Tungsten oxide nanoparticles of $\approx$100 nm in diameter were used as a precursor to react with hydrogen (H$_2$) and hydrogen sulfide (H$_2$S) gases at an elevated temperature of 750-840 °C. The reaction consists of two steps, both carried out in the same reaction zone and following each other in a self-controlled manner. During the first step, the suboxide whiskers of 10-20 micron in length and 20-120 nm in diameter were grown by the reaction of the precursor oxide with hydrogen. In the second step, the tungsten oxide whiskers were converted into tungsten sulfide nanotubes by an outward-inward process. The reaction with H$_2$/H$_2$S started from the whiskers surface, creating the outermost sulfide layer, and continued the sulfidization of the inner oxide by the slow diffusion mode. The reaction resulted in full oxide-to-sulfide conversion and hollow WS$_2$ nanotube formation. The formation of the hollow core inside the nanotubes is due to the difference in specific

gravity of the oxide and sulfide phases (7.15 vs. 7.5 g/cm$^3$, respectively).

### 3.3.2 $\alpha$-Fe$_2$O$_3$ nanoparticles

*Material synthesis and characterization*

Stan Wong's group at Stony Brook University employed a combination of adapted hydrothermal and molten salt methods to synthesize the suite of $\alpha$-Fe$_2$O$_3$ nanoparticles used in this work. [300–302] For the hydrothermal synthesis of nanorhombohedra, aqueous solutions of cetyltrimethylammonium bromide (CTAB) were stirred until the solution turned clear. The anhydrous FeCl$_3$ precursor was then added to the solution and stirred until all precursors were dissolved and then delivered to a Teflon-lined stainless steel autoclave. By tuning the precursor ratio unique sizes of nanorhombohedra were produced. [303] The autoclave was filled to 80% of the volume capacity with the precursor solution and then maintained at elevated temperature for set amounts of time. The products were collected after the autoclaves were cooled to room temperature naturally and subsequently washed with distilled water and ethanol (Acros, 99.5%) by centrifugation. Truncated one-dimensional nanostructures, which we call "nanorice," were generated by the hydrothermal reaction of ferric chloride and ammonium dihydrogen phosphate. Multifaceted polyhedra were prepared by mixing commercial iron oxide nanoparticles (Aldrich) with NaCl (Mallinckrodt) and nonylphenol ethoxylate (NP-9) (Aldrich), in a 1:40:6 molar ratio. The precursor materials were ground together in an agate mortar for thirty minutes and subsequently sonicated before being placed into a porcelain coated ceramic crucible. The sample was then annealed in a tube furnace at 820° C for 3.5 hours and allowed to cool down to room temperature at a natural rate. The as-prepared particles were isolated from the salt matrix by washing the product with distilled water and ultimately collected with centrifugation.

The composition and crystallinity of our as-prepared products were investigated by x-ray powder diffraction. Diffraction patterns were obtained on a Scintag diffractometer, operating in the Bragg-Bretano configuration using Cu K$\alpha$ radiation ($\lambda$ = 1.54 Å) from 20 to 70° at a scanning rate of 0.50° per minute. To investigate the size and morphology of our as-prepared nanoparticles, the product was dispersed in ethanol by sonication and drop cast onto a clean silicon wafer. The substrates were subsequently imaged with a Hitachi S-4800 field-emission scanning electron microscope operating at an accelerating voltage of 5 KV.

## Magnetic property measurements

The $dc$ magnetization of the $\alpha$-Fe$_2$O$_3$ nanoparticles sealed inside gelatin capsules with paraffin wax was measured after both zero-field cooling and field cooling in a Quantum Design Magnetic Properties Measurement System from 1.8 to 300 K under an applied field of 500 Oe by Jack Simonson at Farmingdale State College.

### 3.3.3   CuF$_2$(H$_2$O)$_2$(3-chloropyridine)

## Material synthesis

CuF$_2$(H$_2$O)$_2$(3-chloropyridine) was grown by John Schlueter's group by slowly diffusing a vapor of 3-chloropyridine into an aqueous solution of CuF$_2$(H$_2$O)$_x$ as described previously [82]. Sample quality was confirmed by x-ray diffraction and magnetic susceptibility.

## First principles calculations

Puru Jena's group at Virginia Commonwealth University carried out multi-scale calculations in which both the molecular unit was modeled using molecular orbital

theory and the magnetic properties under pressure were calculated via super cell techniques and band structure methods. Using density functional theory with the generalized gradient approximation, we calculated lattice dynamics of a single unit of $CuF_2(H_2O)_2$(3-chloropyridine) as well as an isolated 3-chloropyridine ring and water molecule to assign the vibrational modes. The relative enthalpy of the antiferromagnetic and ferromagnetic states was calculated at various pressures using spin-polarized density functional theory. [289]

### 3.3.4 $Mn[N(CN)_2]_2$

*Material preparation*

Polycrystalline $Mn[N(CN)_2]_2$ was synthesized by Jamie Manson's group as described previously. [229] $MnCl_2$ was reacted with $Na[N(CN)_2]$ in a 1:2 stoichiometry in aqueous solution, producing a colorless microcrystalline powder.

*Theoretical calculations*

First-principles calculations were performed based on density-functional theory within the generalized gradient approximation GGA+$U$ scheme [304] with the Perdew-Becke-Erzenhof parametrization [305] as implemented in the Vienna *ab initio* simulation package. [306, 307] We employed the Dudarev [308] implementation with on-site Coulomb interaction $U = 5$ eV to treat the localized $d$ electron states of Mn. Within GGA+$U$ this choice gives excellent agreement between the calculated (4.66 $\mu_B$) and experimental magnetic moments (4.65 $\mu_B$). [240] The projector augmented wave potentials [309, 310] explicitly include 13 valence electrons for manganese ($3p^6 3d^5 4s^2$), 5 for nitrogen ($2s^2 2p^3$), and 4 for carbon ($2s^2 2p^2$). Structural optimizations were performed for a 22-atom unit-cell with a $6 \times 6 \times 6$ Monkhorst-Pack $k$-point mesh.

Raman mode frequencies were computed using the frozen phonon method to capture soft-modes driven by pressure. To find the minimum-energy configuration of the soft modes with pressure, we added one (under $\sim$2 GPa) or two unstable soft modes (under $\sim$3-5 GPa) in the ground state structure and moved the atoms according to the conjugate-gradient algorithm until the Hellman-Feynman forces were less than 1.0 meV/Å. Interestingly, when we added the two soft modes to the $Pnnm$ ground state under the higher pressures (3-5 GPa), only the $R_a$ soft mode leading to the monoclinic $\delta$ phase remains after the relaxation. A Heisenberg-type spin Hamiltonian ($\mathcal{H} = -\sum_{\langle i,j \rangle} J_{i,j} \mathbf{S_i} \cdot \mathbf{S_j}$) was employed to estimate the exchange interactions. As a point of comparison, the calculated $J$ value at ambient conditions (-0.12 meV) is in good agreement with the experimental value (-0.07 meV). [240, 241]

# Chapter 4

# High pressure vibrational properties of WS$_2$ nanotubes

We bring together synchrotron-based infrared and Raman spectroscopies, diamond anvil cell techniques, and an analysis of frequency shifts and lattice dynamics to unveil the vibrational properties of multiwall WS$_2$ nanotubes under compression. While most of the vibrational modes display similar hardening trends, the Raman-active $A_{1g}$ breathing mode is almost twice as responsive, suggesting that the nanotube breakdown pathway under strain proceeds through this displacement. At the same time, the previously unexplored high pressure infrared response provides unexpected insight into the electronic properties of the multiwall WS$_2$ tubes. The development of the localized absorption is fit to a percolation model, indicating that the nanotubes display a modest macroscopic conductivity due to hopping from tube to tube.

## 4.1 Vibrational mode assignments and pressure trends

Figure 4.1(a,b) displays the infrared and Raman response of the $WS_2$ nanotubes. At ambient conditions, the infrared spectrum exhibits vibrational modes at 356.7, 438.3, and 498.6 $cm^{-1}$ which are assigned as $E_{1u}$ symmetry, $A_{2u}$ symmetry, and a combination mode, respectively. [311, 312] The ambient pressure Raman spectrum shows features at 360.0, 415.9, and 420.7 $cm^{-1}$ which are assigned as $E_{2g}$, $B_{1u}$, and $A_{1g}$ symmetry modes, respectively. [311, 313, 314] The latter are in excellent agreement with previous Raman measurements. [314] The displacement patterns for these modes are summarized in Fig. 4.2, where the single crystal displacements are used in approximation of the multi-walled nanotubes. While these are all intralayer modes, [63, 311–314] i.e. not the rigid layer modes observed at lower frequencies, [189, 257, 315–317] the A and B symmetry modes can still reveal interlayer interactions as their displacements
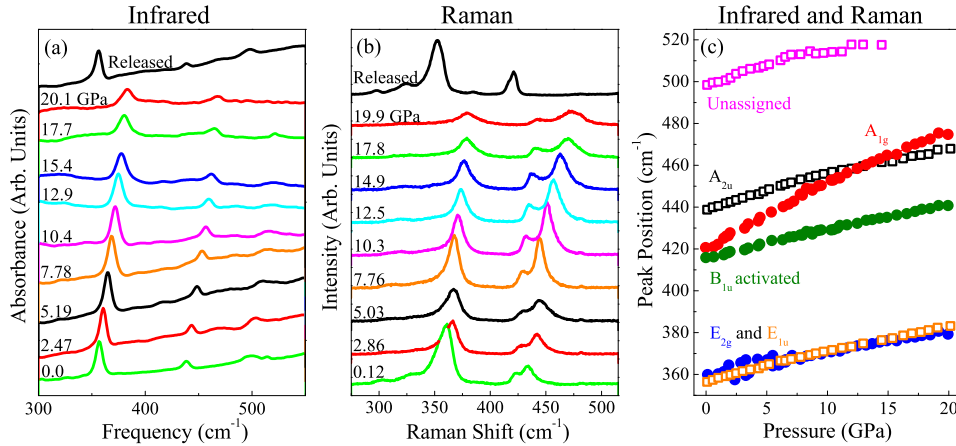


Figure 4.1: (a) Infrared and (b) Raman spectra of $WS_2$ nanotubes at the indicated pressures focusing on the observed vibrational modes. The number and position of modes are consistent with expectations, and the released spectra are taken after the compression cycle. (c) Frequency vs pressure for the infrared- (open squares) and Raman-active (closed circles) modes, displaying the stronger pressure sensitivity of the $A_{1g}$ mode. The unassigned feature is likely a combination mode rather than a fundamental.
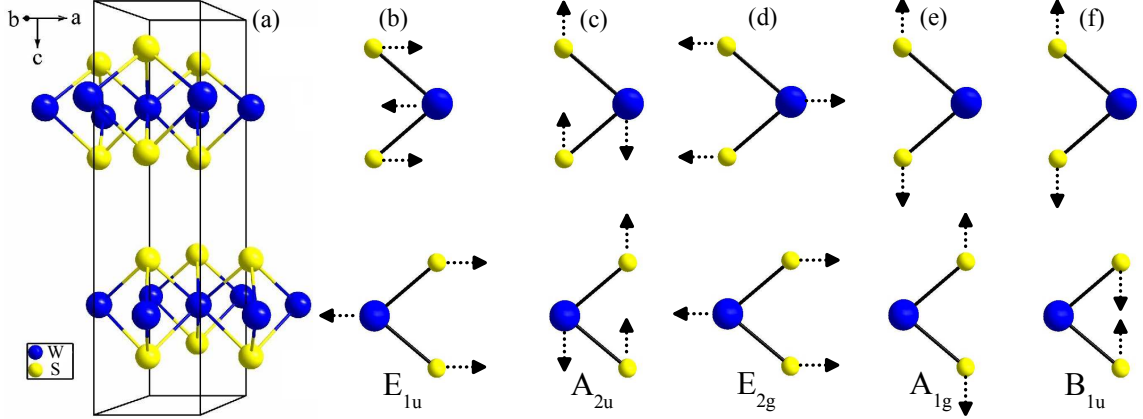
Figure 4.2: (a) The unit cell of WS$_2$ consists of two layers; in each layer W is covalently bonded to six S atoms in trigonal prismatic coordination, [182] which form the walls of the tubes. These layers comprise the $ab$-plane, and are stacked along the $c$ axis. Displacement patterns for the (b,c) infrared- and (d-f) Raman-active phonons. [311,312] While these mode patterns and symmetries formally apply only to the single crystal, they are regularly extended to describe nanoscale analogs.

have out-of-plane components. These assignments and symmetries are brought together in Table 4.1.

In order to better understand the microscopic aspects of tube breakdown, we investigated the vibrational properties of the WS$_2$ nanotubes under compression. Tracking the mode frequencies versus pressure shows that all peaks harden systematically up to 20 GPa, in line with the lack of a structural phase transition in the single crystal. [184] Bringing the peak position versus pressure data together in Fig. 4.1 (c) highlights a far more exciting trend. While the majority of features display similar

Table 4.1: Assignments, pressure-induced hardening, mode Grüneisen parameters, and fractional frequency increase for the vibrational modes of WS$_2$ nanotubes.

| $\omega_{Ambient}$ (cm$^{-1}$) | Activity | Symmetry | d$\omega$/dP (cm$^{-1}$/GPa) | Grüneisen parameter [a] | Grüneisen parameter [b] | $(1/\omega)(d\omega/dP)$ $10^{-2}$ kbar$^{-1}$ |
|---|---|---|---|---|---|---|
| 356.7 | infrared | E$_{1u}$ | 1.31 ± 0.02 | 0.28 | 0.70 | 0.037 |
| 438.3 | infrared | A$_{2u}$ | 1.44 ± 0.03 | 0.25 | 1.67 | 0.033 |
| 498.6 | infrared | - | 1.44 ± 0.08 | - | - | 0.027 |
| 360.0 | Raman | E$_{2g}$ | 1.05 ± 0.05 | 0.21 | 0.51 | 0.027 |
| 415.9 | Raman | B$_{1u}$ | 1.25 ± 0.03 | 0.23 | 1.51 | 0.030 |
| 420.7 | Raman | A$_{1g}$ | 2.79 ± 0.04 | 0.49 | 3.25 | 0.064 |

[a] Traditional Grüneisen parameters calculated using the unit cell volume. [b] "Directional" Grüneisen parameters calculated using the pressure dependence of the unit cell parameter $a$ or $c$ based on the displacement. [201]

41

hardening (with dω/dP between 1 and 1.4 cm$^{-1}$/GPa), [318] the 420.7 cm$^{-1}$ Raman mode is different, with dω/dP on the order of 2.8 cm$^{-1}$/GPa (Fig. 4.1 (c) and Table 4.1). It is worth noting that while the pressure-induced frequency shift of the $A_{1g}$ mode (and in fact all of the Raman-active modes in the WS$_2$ tubes) is in perfect agreement with the work of Staiger *et al.* [314] up to 10 GPa, the extension of our study up to 20 GPa and the ability to compare with infrared unambiguously reveals the uniqueness of the $A_{1g}$ displacement. As we shall argue below, the large dω/dP of the Raman-active $A_{1g}$ mode suggests that it may be an integral part of the tube breakdown pathway. That long wavelength acoustic modes are blocked in confined systems like WS$_2$ nanoparticles is consistent with this interpretation. [319]

To quantify these effects, we calculated the mode Grüneisen parameters as $\gamma_i = -\frac{\partial \ln \omega_i}{\partial \ln V} = (\omega_i \chi_T)^{-1}(\frac{\partial \omega_i}{\partial P})$, where $\omega_i$ is the frequency of the $i$th mode, and $\chi_T = -V^{-1}(\frac{\partial V}{\partial P})$ is the isothermal compressibility, $V$ is the volume, and $P$ is pressure. [201, 320] As a reminder, the $\gamma_i$ characterize mode stiffness. Due to the strong polarization of the vibrational modes, we also calculate a "directional Grüneisen parameter" using the unit cell parameter pertinent to the displacement in place of the cell volume. [201] This is done by replacing the volume derivative in the $\chi_T$ expression with that along the specific axis of interest, for instance $\chi_T = -c^{-1}(\frac{\partial c}{\partial P})$ for modes with displacements along the $c$ axis. We also calculated the fractional frequency increase $(1/\omega)(d\omega/dP)$ for each mode, which are in good agreement with the intralayer modes of similar layered sulfides. [257] Moreover, as an approximation, the force constant increase at 20 GPa for each mode can be estimated as $(\frac{\omega_{0\ GPa}}{\omega_{20\ GPa}})^2$. The $A_{1g}$ mode force constant increased by ≈1.27, whereas the next highest increase is ≈1.15 for the $E_{1u}$ mode. In all cases, we again see that the $A_{1g}$ mode is unique, with values that are significantly higher than those for the other modes irrespective of the calculation method (Table 4.1). We conclude that the $A_{1g}$ mode is much stiffer than

the others. Similar findings are anticipated for the transition metal dichalcogenide nanoparticles. [63]

Bringing our spectroscopic findings together with an analysis of the displacement patterns reveals why the 420.7 cm$^{-1}$ Raman mode in the WS$_2$ nanotubes is so sensitive to applied pressure. It is well-known that interlayer van der Waals forces are weaker than the intralayer covalent bonding in transition metal dichalcogenides. [47, 257] Local lattice distortions in this direction thus provide a "path of least resistance" for volume reduction. Based on this simple idea, the A and B symmetry modes are expected show the greatest pressure dependence since they contain out-of-layer displacements. Let us consider the A$_{1g}$ mode in this context. The displacement pattern involves in-phase out-of-plane expansion of the layers, so it is logical that it is the most affected by compression since the layers have less and less room to expand. This accounts for the magnitude of the volume and linear Grüneisen parameters in Table 4.1. The A$_{2u}$ and B$_{1u}$ modes are different - even though they also probe the elastic properties in the $c$ direction. Their pressure dependencies are, in fact, similar to the E symmetry modes, a finding that can again be explained by the displacement patterns. The A$_{2u}$ mode consists of WS$_2$ units counter-rotating within the $ac$-plane, whereas in the B$_{1u}$ mode, the WS$_2$ layers expand out-of-plane and out-of-phase [Fig. 4.2 (c,f)]. As a result, interlayer distance does not strongly affect these motions. This analysis clearly shows why the A$_{1g}$ vibrational mode is most sensitive to reduced interlayer distances. It also reveals why this displacement is a likely driver of the WS$_2$ nanotube breakdown mechanism. We anticipate that this type of breathing mode will also be important in other nanotubes formed from layered materials, such as MoS$_2$ or the newly discovered misfit layered compounds, [321] under compression.

## 4.2 Microscopic breakdown mechanism and comparison to theory

Theoretical modeling of the tubes under uniaxial pressure (perpendicular to the tube axis) gives insight into the breakdown mechanism. [195] The tube layers are predicted to distort under pressure, with the innermost layer being the most affected. The layers eventually fracture at a pinching point, and the crack propagates from the inside to the outer most layer forming two dimensional sheets. [195] Shockwave experiments reveal a similar mechanism in $WS_2$ nanoparticles, except the fracture propagates from the outermost layer inwards. [53, 196, 322] These findings dovetail with our experimental results, which provide direct microscopic evidence for this mechanism. The large pressure-induced frequency shift of the $A_{1g}$ mode suggests a strong interlayer component to the breakdown pathway. In fact, transmission electron microscope images of tubes after compression (Fig. 4.3) display a remarkable set of fractures perpendicular to the tube direction, i.e. along the direction of the $A_{1g}$ displacement. The fractures appear to propagate from the outside inward, as evidenced by the exfoliation of the outer layer in some instances [Fig. 4.3 (c)]. It is important to realize that this type of fracture event is fairly local, probably occurring over a range of pressures and leaving much of the nanotube unperturbed. If the entire length of the tube were to be damaged at once there would instead be a sharp discontinuity in the frequency versus pressure trends.

Although isotropic (three-dimensional) pressure is applied in our work, it is comparable to strain in that it modifies bond lengths and angles. Density functional theory calculations predict that the Raman signatures of the in- and out-of-plane modes depend linearly on axial strain. [323] Our data show that the Raman mode frequencies do indeed change linearly with pressure. The $E_{2g}$ mode is, however, pre-
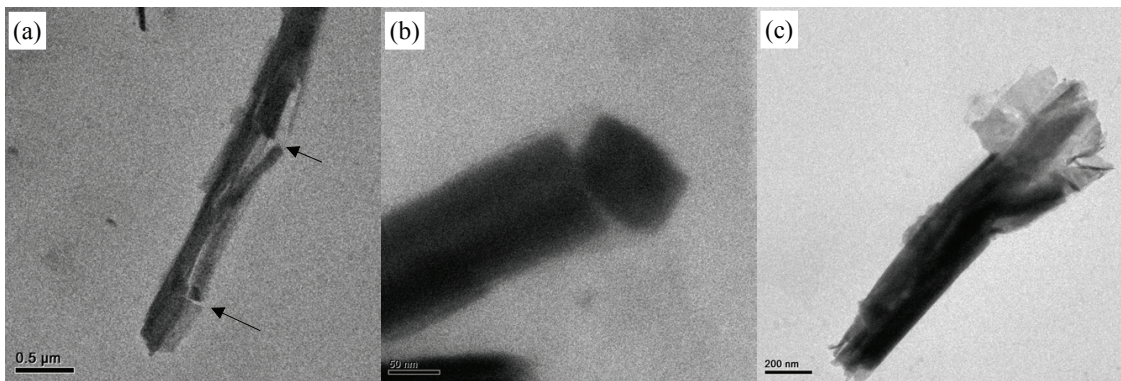
Figure 4.3: TEM images of the nanotubes after compression to 20 GPa in the diamond anvil cell and subsequent release, demonstrating the fractures perpendicular to the tube direction (a,b) and exfoliation of the outer layer (c).

dicted to be more sensitive to tensile strain than the $A_{1g}$ mode, [323] different than the experimental high pressure response in Fig. 4.1. This discrepancy probably originates from the tensile strain being applied only along the length of the nanotube in the calculations, i.e. along the $a$ axis, therefore not affecting the interlayer spacing as strongly as the isotropic pressure applied in our work. These differences clearly merit future investigation. [324–326]

## 4.3 Electronic properties under pressure

The electronic properties of transition metal dichalcogenides are also attracting sustained attention. For instance, $MoS_2$ metallizes under pressure in both bulk powder and single crystal form. [31, 260] Moreover, simulations of $WS_2$ nanotubes under tensile strain predict band gap closure above 16% nanotube elongation. [323, 329] Pressure is clearly a very effective tuning parameter. We are therefore very interested in any signature or tendency toward novel electronic behavior in the tubes.

In addition to the vibrational modes discussed in prior sections, the infrared response of the $WS_2$ tubes displays a broad and rising electronic background under pressure that can be seen both in the absolute absorption and the absorption dif-

ference spectra [Fig. 4.4 (a,b)]. [330] This localized absorption may be indicative of percolation. We therefore consider what can be learned from effective medium theories. [331, 332] While percolation theory usually refers to the concentration of a conducting material in a non-conducting matrix (like metal nanoparticles in glass), [334] the analogy can be made to a fixed concentration in a decreasing volume. As pressure is applied, the nanotubes are forced closer together until they eventually touch [inset, Fig. 4.4 (c)]. When enough tubes are in contact, a conductive pathway can be created, so we can think of these experiments as "sweeping concentration."

To quantify this trend, we tracked the absorption difference at 295 cm$^{-1}$ versus pressure [Fig. 4.4 (c)]. In line with percolation modeling of layered networks of semiconducting carbon nanotubes, [335, 336] we fit the absorption difference at 295 cm$^{-1}$ to the sigmoidal Boltzmann equation, $I = \frac{A_1 - A_2}{[1 + exp(P - P_0)/\Delta P]} + A_2$, where $I$ is the percolation probability, $A_1$ is the percolation at ambient pressure, $A_2$ is the high pressure percolation limit, $P$ is pressure, and $P_0$ and $\Delta P$ are the pressure at the midpoint
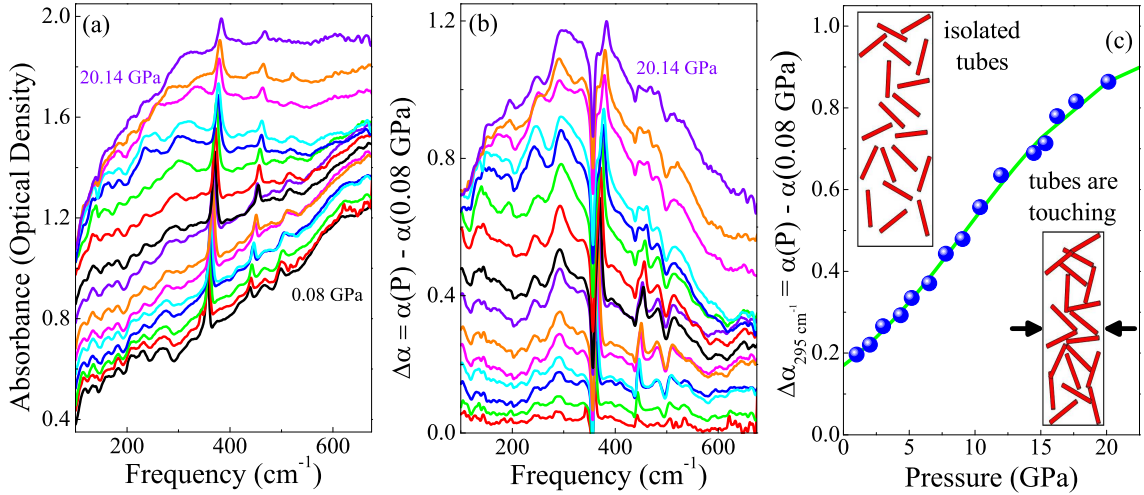


Figure 4.4: (a) Infrared spectra at increasing pressures. (b) Absorption difference, $\Delta\alpha = \alpha(P) - \alpha(0.08 \text{ GPa})$, showing the increasing background due to improved conductivity under pressure caused by percolation effects. (c) Absorption difference at 295 cm$^{-1}$ versus pressure. The green line is a fit to the percolation model described in the text. Insets: schematic views of the diamond anvil cell at low and high pressure showing the conductive pathway that forms as the tubes begin to touch.

of percolation and pressure range from zero to full percolation, respectively. We find the percolation threshold to be $P_0$=9.3 GPa and predict that percolation will saturate at 40 GPa. [337] Our modeling also indicates that there is some percolation even at ambient conditions, demonstrating that while the individual $WS_2$ tubes may be relatively conducting, the ensemble properties are dominated by hopping from tube to tube. This finding is consistent with both theoretical and experimental conductivities and band gaps. [65, 338–341] Using the position of the broad electronic background as a measure of the hopping barrier [Fig. 4.4 (b)], we find an activation energy of approximately 350 cm$^{-1}$ (43 meV). Although we measured up to 20 GPa, which is close to the 19 GPa metallic transition in multilayered $MoS_2$, [31, 260] there is no evidence for a Drude response in the multiwall $WS_2$ nanotubes. No metallic behavior was observed in bulk $WS_2$ up to 52 GPa either, [201] suggesting critical differences between the Mo and W systems that give additional stability to $WS_2$ and cause the analogous transition to move to much higher pressures. [201]

# Chapter 5

# Size-dependent optical properties of $\alpha$-Fe$_2$O$_3$ nanoparticles

We investigate the size-dependent optical properties of a suite of $\alpha$-Fe$_2$O$_3$ nanoparticles focusing on the Fe$^{3+}$ on-site excitation to probe confinement effects on coupling processes. At small size the phonon responsible for activating the $d - d$ excitation crosses over to a lower frequency mode due to increasing three-dimensional character of the displacement. Confinement also affects the spin-charge coupling through the spin-flop transition; high field color contrast is enhanced with reduced size, until the superparamagnetic length scale is reached. Moreover, the size dependence of collective excitations such as the magnon sideband are revealed. These findings demonstrate the flexibility of mixing processes in confined systems and suggest a strategy for both enhancing and controlling coupling processes in other materials.

## 5.1  Size-dependent vibronic coupling

Figure 5.1 (a-c) displays the absorption spectra for single crystalline hematite and select nanoparticles at 4 and 300 K. The dominant structure in this spectral region
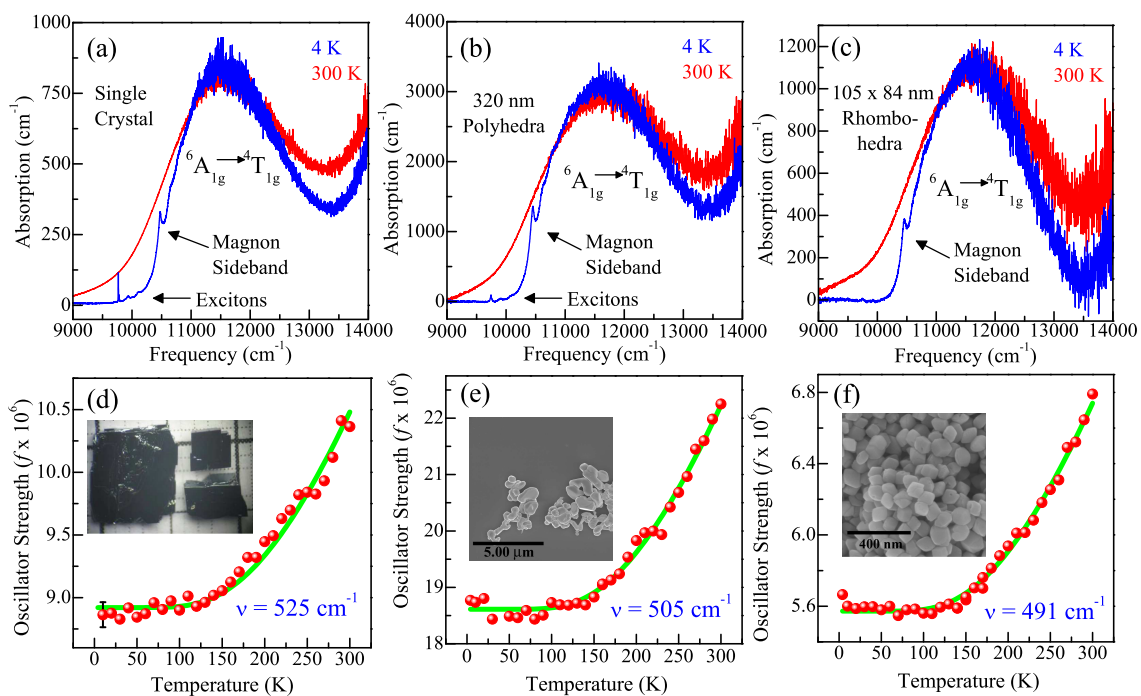
Figure 5.1: (a-c) Absorption at 4.2 and 300 K for the (111) plane of the single crystal, nanopolyhedra, and largest nanorhombohedra, respectively. Excitons and a magnon sideband can be seen in the low temperature spectrum of the single crystal, whereas the nanoparticles reveal strong magnon sideband excitations but only weak exciton features. (d-f) Oscillator strength of the color band transition as a function of temperature for the single crystal, nanopolyhedra, and largest nanorhombohedra, respectively. A representative error bar is given in (d). The green lines represent fits to the vibronic coupling model described in the text. Insets: Images of each material.

is assigned as the $^6A_{1g} \rightarrow {}^4T_{1g}$ $Fe^{3+}$ on-site electronic excitation. [160] This $d-d$ excitation and the one around 16,000 $cm^{-1}$ (not shown) are formally spin and parity forbidden, but are observed due to exchange interactions, spin-orbit coupling, and odd parity phonons that break inversion symmetry. [160, 161, 342] The low temperature single crystal spectrum reveals excitons and a magnon sideband on the leading edge of the $d-d$ transition. [159] While the magnon sideband is still observed in the nanoparticle spectra, the excitons are more obscured due to the random orientation of the nanoparticles combined with the directional character and low oscillator strengths of the excitons. We calculated the oscillator strength of the electronic excitation at temperatures 10 K increments between 4 and 300 K [Fig. 5.1 (d-f)]. [343] The 260 K discontinuity in the oscillator strength of the single crystal is a signature of the spin-flop transition. [148] Magnetization measurements show that the spin-flop is present in the nanoparticles but is obscured by the error bars on oscillator strength. [303]

The temperature dependent oscillator strength for a vibronically activated excitation is described as

$$f = f_0 \coth(h\nu/2kT), \tag{5.1}$$

where $f$ is oscillator strength, $f_0$ is the limiting low temperature oscillator strength, $\nu$ is the frequency of the vibrational mode that activates the on-site excitation, $h$ is Planck's constant, $k$ is Boltzmann's constant, and $T$ is temperature. [342] We employed this model to fit the oscillator strength trends and extract the coupling phonon frequencies. The best fits are shown in Fig. 5.1 (d-f), and the fit parameters are summarized in Table 5.1. The magnitude of the oscillator strength of the $d-d$ excitation in each sample agrees well with typical oscillator strengths of parity forbidden transitions observed in other transition metal oxides like $CuGeO_3$ [291] and iron containing materials such as $CsFeCl_3$. [345] Our extracted value of $\nu$=525 $cm^{-1}$ for single crys-

Table 5.1: Summary of the material characteristics, fitting parameters obtained from the vibronic coupling model, full field absorption difference $\Delta\alpha = (\frac{\alpha(35\ T)-\alpha(0\ T)}{\alpha(0\ T)}) \times 100$, and color contrast $|\Delta\alpha|$ of the hematite nanomaterials used in this work. Error bars in size represent a distribution of sizes.

| material | particle length (nm) | particle width (nm) | $f_0$ $(10^{-6})$ | $\nu$ (cm$^{-1}$) | $\Delta\alpha$(%) | $|\Delta\alpha|$(%) |
|---|---|---|---|---|---|---|
| single crystal | 42 $\mu$m | - | 10.8 | 525 ± 6 | | |
| bulk powder | 1000 nm | - | 4.73 | 529 ± 4 | -1.2 | 1.2 |
| cubes | 450 ± 60 | 450 ± 60 | 25.1 | 507 ± 8 | -1.6 | 1.6 |
| polyhedra | 320 ± 90 | 320 ± 90 | 18.6 | 505 ± 4 | -1.2 | 1.2 |
| rice | 148 ± 32 | 67 ± 10 | 1.61 | 498 ± 4 | 0 | 0 |
| rhombohedra | 105 ± 16 | 84 ± 12 | 5.57 | 491 ± 3 | -1.5 | 1.5 |
| rhombohedra | 75 ± 8 | 50 ± 7 | 5.38 | 460 ± 4 | -2.1 | 2.1 |
| rhombohedra | 59 ± 9 | 59 ± 8 | 1.97 | 490 ± 9 | -3.1 | 3.1 |
| rhombohedra | 50 ± 8 | 35 ± 7 | 2.54 | 469 ± 8 | -1.9 | 1.9 |

talline hematite is significantly larger than the previously reported 139 cm$^{-1}$ acoustic phonon, [78] but lies within the range of phonons energies in hematite. In fact, it is an excellent match for the E$_u$ symmetry mode centered at 520 cm$^{-1}$. [346] This difference likely arises from the fact that the previous authors measured only along one crystal axis, did not investigate below 100 K, and used an approximate model that assumes that both the ground and excited state are characterized by harmonic oscillators that share force constants and equilibrium positions. [347, 348] Our more comprehensive analysis was also carried out on a micron-sized bulk powder (in order to compare the single crystal to the randomly oriented nanoparticles), nanocubes, nanopolyhedra, nanorice, and four sizes of nanorhombohedra. Figure 5.1 shows some representative examples. The nanoparticle dimensions and extracted parameters are summarized in Table 5.1.

Figure 5.2 displays the coupling phonon frequency, $\nu$, that we extract from this vibronic coupling analysis, versus average particle size. There is excellent agreement between the two largest sizes (the single crystal and micron-sized bulk powder). Both yield a coupling phonon frequency of about $\nu$=525 cm$^{-1}$. For the 450 nm nanocubes, we extract a coupling frequency of 507 cm$^{-1}$. For the smallest size of nanorhombohedra, we find $\nu$=469 cm$^{-1}$. Overall, reduction of particle size decreases
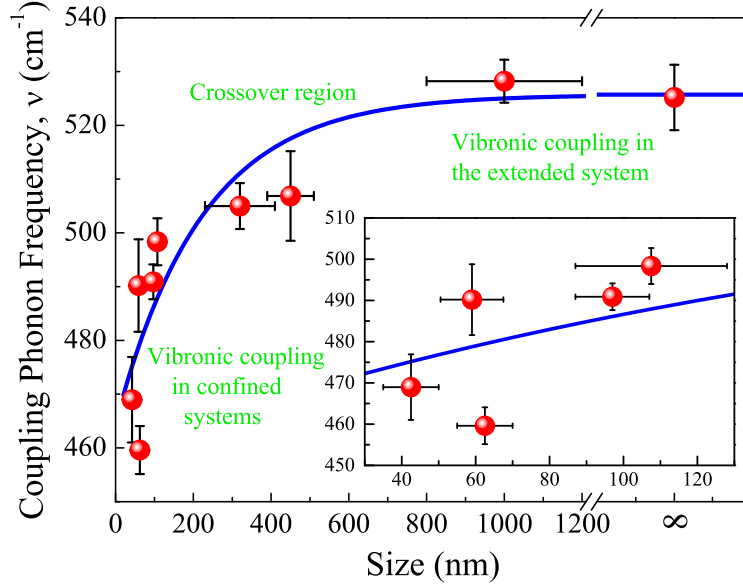
Figure 5.2: Coupling phonon frequency, $\nu$, versus average particle size as determined by the oscillator strength analysis described in the text. The blue line guides the eye. Interestingly, this trend depends only on the particle size, with shape playing no role. Inset: Expanded view of the trend for the smallest nanoparticles.

the coupling phonon frequency that activates the color band excitation. This decrease is much larger than what might be expected from size-dependent changes in phonon frequencies for hematite alone. [38]

In order to activate the spin and parity forbidden on-site excitation, the coupling phonon mode must break the inversion symmetry around the $Fe^{3+}$ center. The activating phonon must then be of *ungerade* symmetry, i.e. infrared active. To test whether the phonon frequencies extracted from our vibronic coupling analysis correlate with actual vibrational modes, we measured the infrared response of each set of nanoparticles [Fig. 5.3 (a)]. From our vibronic coupling analysis, we extract $\nu = 525$ cm$^{-1}$ for the bulk material, and in the infrared there is an $E_u$ symmetry phonon mode observed at 530 cm$^{-1}$. [109] This phonon mode consists mainly of atomic displacements within the $ab$ plane. [81] For the 450 nm cubes, $\nu$ is found to be 507 cm$^{-1}$, which is now between the peaks observed at 560 and 480 cm$^{-1}$, indicating
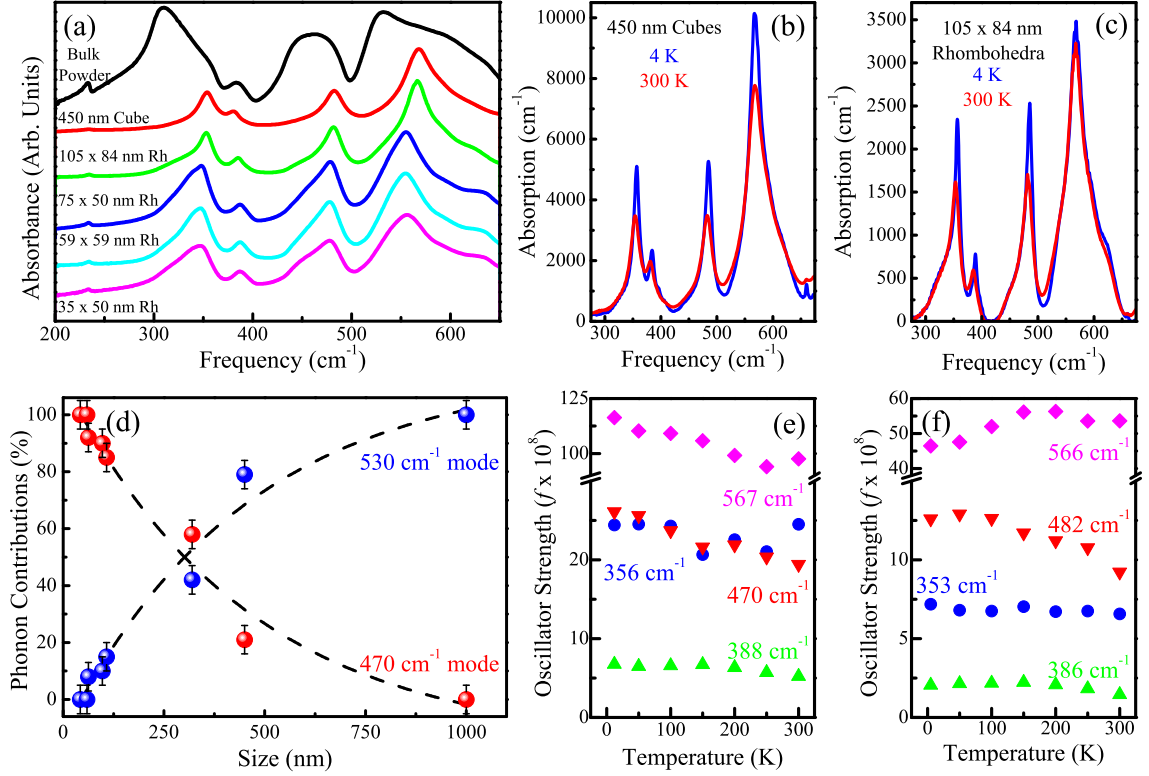
Figure 5.3: (a) Representative 300 K infrared absorption spectra for the bulk powder (black), nanocubes (red), and nanorhombohedra from largest (green) to smallest (magenta). Infrared response at 4 and 300 K for the (b) 450 nm nanocubes, and (c) 84 nm nanorhombohedra. All phonon modes harder upon cooling. (d) Contribution of the 470 and 530 $cm^{-1}$ phonon modes to the activation of the on-site excitation. At large sizes, the 530 $cm^{-1}$ mode consisting of only $ab$ plane motion dominates. There is a strong superposition at intermediate sizes as well as a crossover. At small sizes, the 470 $cm^{-1}$ mode consisting of $ab$ plane and $c$ axis motion dominates. Analysis of the data in (b) and (c) allow us to follow phonon oscillator strengths as a function of temperature. Panels (e) and (f) show our findings for the nanocubes and nanorhombohedra, respectively. Only the phonon modes extracted from our vibronic coupling analysis gain significant oscillator strength at low temperature, a finding that directly confirms the aforementioned weighting crossover in the intermediate size regime.

that both modes are contributing to the activation of the color band. Turning to the smallest nanoparticles (the 35×50 nm rhombohedra), $\nu$ is determined to be 469 cm$^{-1}$. Indeed, the infrared spectrum does reveal a phonon mode at 470 cm$^{-1}$. The displacement pattern for this mode consists of combined $ab$ plane and $c$ axis motion. [81] Taken together, these findings suggest that there is a crossover from the 530 cm$^{-1}$ phonon mode activating the transition at large sizes to the 470 cm$^{-1}$ mode at small sizes. In the intermediate size region, our analysis yields a weighted average of the two mode frequencies (530 and 470 cm$^{-1}$). [350] This size driven crossover is reminiscent of a simple two state kinetics model, with particle size in place of time, and the concentrations (or two states in our case) are the relative contribution of the 530 and 470 cm$^{-1}$ phonon modes to $\nu$.

To understand why this crossover occurs, we must consider how nanoscale confinement affects the structure of hematite. As particle size decreases, the hematite unit cell expands anisotropically, with the $c$ axis expanding faster than the $a$ axis. [170] While this trend has been formally demonstrated for particle sizes below 63 nm, [170] the argument can presumably be extended to the sizes discussed in our work. As the unit cell expands, $c$-directed displacements in the 470 cm$^{-1}$ mode become more important. This enhanced symmetry breaking provides a mechanism for why the electronic transition crosses over to be activated by a lower frequency phonon mode at small size. Moreover, the trend appears to be independent of particle shape, as the nanorice (with a vastly different aspect ratio than the nanocubes and nanorhombohedra) and the multifacted polyhedra follow the same trend with excellent agreement. The reduction of $\nu$ also suggests that small nanoparticles should be more sensitive to temperature than bulk hematite as indicated by the greater relative increase in oscillator strength.

At low temperature, coupling between the activating phonon mode and the elec-

tronic transition is reduced, and the activating phonon mode may recover some oscillator strength instead of conserving oscillator strength. [351] We carried out variable temperature infrared measurements to test this idea. Figure 5.3 (b,c) displays the 4 and 300 K infrared absorption spectra for the nanocubes and largest size of rhombohedra, respectively. Again, due to the overlapping spectral features a simple integration could not be performed, and a standard peak fit method was used to determine the oscillator strength of each mode. In the nanocubes, both the 560 and 470 cm$^{-1}$ phonon modes show a modest increase in oscillator strength at low temperature while the oscillator strength of the other phonon modes remain constant. This indicates that both modes are coupled to the electronic transition, as predicted by our vibronic coupling analysis. In the largest size of rhombohedral nanoparticles, the 480 cm$^{-1}$ E$_u$ phonon mode regains oscillator strength at low temperature while the 560 cm$^{-1}$ mode remains constant. This nicely confirms that only the 480 cm$^{-1}$ phonon mode is coupled to the electronic transition as anticipated [Fig. 5.3 (e,f)].

We note that size-dependent vibronic coupling is not unique to $\alpha$-Fe$_2$O$_3$. Ongoing work on nanorods of the inorganic spin-Peierls material CuGeO$_3$ is revealing a similar crossover in the activating phonon.

## Magneto-optical properties of hematite nanoparticles

Figure 5.4 (a-c) displays the absorption of polycrystalline $\alpha$-Fe$_2$O$_3$ as well as the response of two different sizes of $\alpha$-Fe$_2$O$_3$ nanoparticles. We assign the broad absorption band centered at 11,600 cm$^{-1}$ as the $^6$A$_{1g} \rightarrow ^4$T$_{1g}$ Fe$^{3+}$ on-site excitation [78] and the smaller feature on the leading edge of this structure (at 10,470 cm$^{-1}$) as a magnon sideband. [162] The former is activated by vibronic coupling and interaction with odd parity phonons whereas the latter is a characteristic dipole-allowed transition that appears in a number of antiferromagnets. [78, 160, 161, 352] The collective
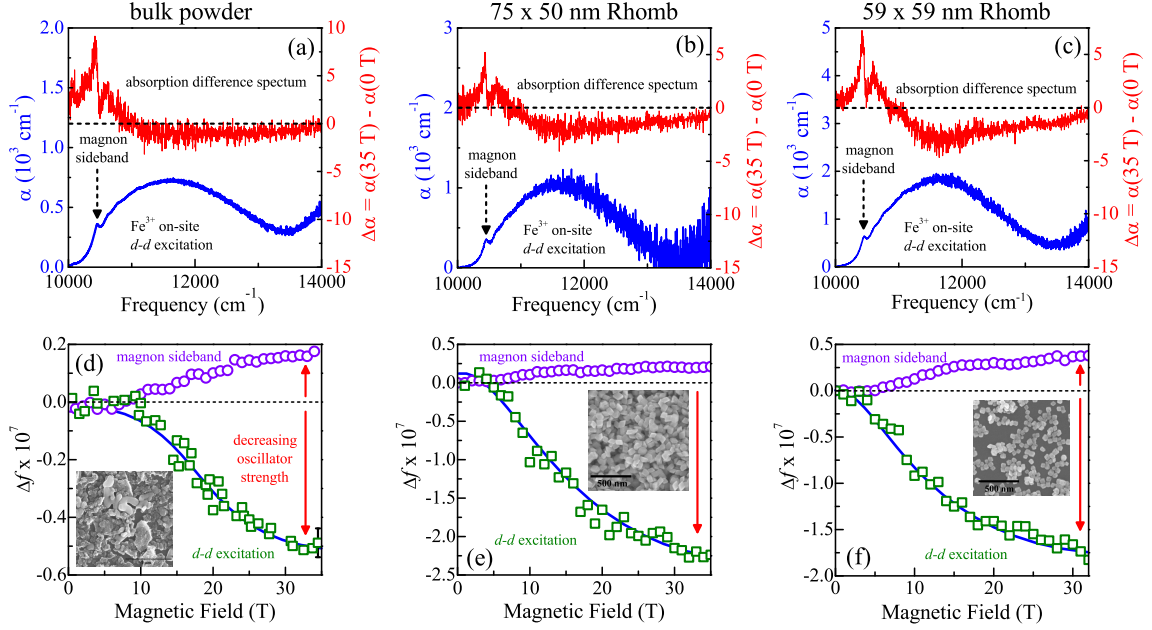
Figure 5.4: (a-c) 4.2 K absorption spectrum of polycrystalline hematite and selected nano-rhombohedra beneath the full field absorption difference spectrum, $\Delta\alpha = \alpha(35\ T) - \alpha(0\ T)$, for comparison. The full data set is available in the Supplementary Information. (d-f) Change in oscillator strength ($\Delta f$) of the $d$-to-$d$ on-site excitation (green squares) and magnon sideband (violet circles) vs. magnetic field for these materials. Blue lines guide the eye.

nature of the magnon sideband makes it a superb probe of spin-charge coupling and magnetic quantum phase transitions. [159, 353] The magneto-optical response of these materials [also in Figure 5.4 (a-c)] is shown as a full field absorption difference: $\Delta\alpha = \alpha(35\ T) - \alpha(0\ T)$. This rendering highlights field-induced spectral changes by eliminating commonalities.

Inspection reveals that the absorption difference spectra have the same general shape regardless of particle size, with field-induced changes to both the $d$-to-$d$ excitation and the magnon side band. A partial sum rule analysis [344] over the appropriate energy windows quantifies these trends [Figure 5.4 (d-f)]. Prior magneto-optical work on single crystals reveals clear optical contrast through the spin-flop transition with enhancement (and softening) of the magnon sideband and diminution of the on-site excitation due to spin-charge interactions. [159] A remnant of these effects appears

in polycrystalline $\alpha$-Fe$_2$O$_3$ and the various nanoparticles of interest here. [354] For example, the oscillator strength of the $d$-to-$d$ excitation in the bulk powder begins to decrease around 6 T and reaches its steepest slope near 16 T, consistent with the easy and hard axis critical fields of the single crystal. [23] The nano-rhombohedra display similar effects although here, the oscillator strength of the color band begins to decrease at lower fields, indicating that smaller fields drive the color change. This is because the critical fields are smaller, in line with direct measurements of $H_c$. [100] At the same time, a portion of this oscillator strength is transferred to the magnon sideband, which grows with increasing field [Figure 5.4 (d-f)].

Table 5.2 summarizes the magnetochromic response of the full suite of $\alpha$-Fe$_2$O$_3$ nanomaterials of interest. [303] Here, we use the field-induced change in the absorption spectrum ($\Delta\alpha_{max}$) at the center position of the on-site excitation (11,600 cm$^{-1}$) and highest available field (35 T) to quantitatively compare how the color band changes with size. Inspection of the last column in Table 5.2 reveals that, in general, spectral contrast (understood as $|\Delta\alpha_{max}|$) increases with decreasing size - independent of shape.

Table 5.2: Summary of the shape, size, and full field absorption difference $\Delta\alpha_{max} = (\frac{\alpha(35\ T)-\alpha(0\ T)}{\alpha(0\ T)}) \times 100$ calculated at the highest absorption ($\approx$11,600 cm$^{-1}$) of the hematite nanomaterials used in this work.

| material | particle length (nm) | particle width (nm) | $\Delta\alpha_{\mathbf{max}}$(%) |
|---|---|---|---|
| bulk powder | $\approx$1000 | $\approx$1000 | -1.2 |
| cubes | $450 \pm 60$ | $450 \pm 60$ | -1.6 |
| polyhedra | $320 \pm 90$ | $320 \pm 90$ | -1.2 |
| rice | $148 \pm 32$ | $67 \pm 10$ | 0 |
| rhombohedra (2x) | $105 \pm 16$ | $84 \pm 12$ | -1.5 |
| rhombohedra (L) | $75 \pm 8$ | $50 \pm 7$ | -2.1 |
| rhombohedra (M) | $59 \pm 9$ | $59 \pm 8$ | -3.1 |
| rhombohedra (S) | $50 \pm 8$ | $35 \pm 7$ | -1.9 |

Figure 5.5 displays the same data in graphical form. It is easy to identify three

distinct regimes: a bulk-like regime, a small size range, and an area below the super-paramagnetic limit. At large sizes, the field-induced color change is nearly constant and on the order of 1.3%. [355] This is true for the single- and poly-crystal as well as for several of the larger nanoparticles including cubes and polyhedra, suggesting that spin-charge coupling (which activates the field-induced color change) is of similar order of magnitude. Things are different when the characteristic particle size drops below about 75 nm (≈60 unit cells). Here, the spectral contrast increases to nearly 3% before dropping back down as the system approaches the super-paramagnetic region. [176] A similar trend emerges for the contrast of the magnon sideband. The enhanced contrast at small size suggests that spin-charge coupling is changing in critical ways - either by systematic enhancement (and subsequent diminishment at
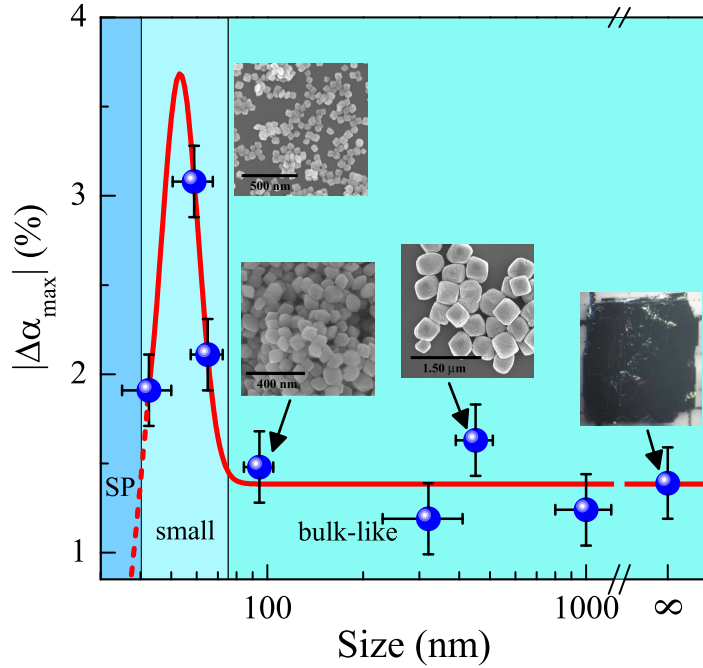


Figure 5.5:   Full field color contrast, $|\Delta\alpha_{max}| = |(\frac{\alpha(35\ T) - \alpha(0\ T)}{\alpha(0\ T)})| \times 100\%$, evaluated at 11,600 cm$^{-1}$ (which corresponds to the maximum of the $d$-to-$d$ absorption) at 4.2 K. A photo of the single crystal and scanning electron microscope images of select nanoparticles are included. The three different size regimes (bulk-like, small size, and super-paramagnetic [SP]) are indicated. The red line guides the eye, with the dashed region approximating what may happen at smaller sizes.

the smallest size) or by involving additional degrees of freedom (besides the spin and charge channels). We test these mechanistic scenarios below and find, to our surprise, that spin-charge coupling not only describes the overall trend but provides a plausible explanation for (i) the curious behavior of the smallest nano-rhombohedra in this study and (ii) the rigidity of the $d$-to-$d$ excitation in the nano-rice.

## Mechanism of field-induced color contrast in $\alpha$-Fe$_2$O$_3$ nanoparticles

It is well established that magnetic field-induced color contrast in hematite single crystals derives from spin-charge coupling that is strongly amplified across the spin-flop transition. [159] It is therefore reasonable to anticipate that a similar mechanism will be relevant to the $\alpha$-Fe$_2$O$_3$ nanoparticles. Our work provides three independent checks of this scenario. The first test involves the behavior of the smallest nanorhombohedra and evaluates the role of the collective transition. Below about 40 nm (close to the size of the smallest rhombohedra), the spin-flop transition does not force spins to lie perfectly along the $c$-axis (as in larger particles) but instead allows a 28° off-axis orientation. [166] This scenario is consistent with the significant moment below the spin-flop transition observed in magnetization measurements of our 35×50 nm$^2$ particles, and it suggests that a degraded spin-flop transition might impact magnetochromism. The second check concerns the nanorice sample and even more firmly establishes the importance of the collective transition. Magnetic property measurements of the nanorice reveal no spin-flop transition, and correspondingly, magneto-optical experiments up to 35 T (and even test runs to 45 T) show no field-induced absorption difference. In other words, the absence of a spin flop transition quenches the color contrast. Together, these two results demonstrate that a robust collective transition - in which the spins fully reorient - is required to modify the $d$-

to-$d$ excitation. The final check of the spin-charge coupling mechanism in hematite nanoparticles involves ruling out a lattice contribution. Since the $d$-to-$d$ excitation is activated by coupling with an odd parity phonon, [303] any spin-lattice coupling is expected to involve an infrared-active mode. Direct magneto-infrared measurements of the smallest rhombohedra up to 35 T, however, reveal no local lattice distortions, implying that the spin-flop transition occurs without any commensurate changes to the lattice. Taken together, these results show that spin and charge are intimately coupled in $\alpha$-Fe$_2$O$_3$ and can interact directly - without involving the lattice.

## Magnetochromic sensing applications

In the discussion above, we describe a general strategy for creating enhanced magnetochromic contrast in magnetic nanoparticles like $\alpha$-Fe$_2$O$_3$. It is important to point out that there are a number of applications that can make use of this technology - especially when the color contrast is visible to the human eye. Earth-abundant materials like hematite are inexpensive, safe, and stable. Moreover, small nanoparticles can be mixed into inks and embedded into fibers to provide very subtle and hard-to-duplicate forms of identification of the type that may be useful for anti-counterfeiting purposes. In $\alpha$-Fe$_2$O$_3$, our measurements suggest that particle sizes near 75 nm are likely to produce maximum red $\rightarrow$ red$'$ magnetochromic color contrast. The magnetic energy scales (as measured by the Morin temperature, for instance) are also relatively high and may be able to support room temperature operation. The latter assumes that the residual spin-spin correlations above the magnetic ordering temperature are sufficient to provide a remnant of the collective transition - a supposition that has yet to be tested. Other iron oxides like Fe$_3$O$_4$ or CoFe$_2$O$_4$ will have somewhat different sweet spots, but our research suggests that the size regime just above the transition to the super-paramagnetic state is the place to search for enhanced

color contrast that can be observed with a hand-held spectrometer or (even better) by the naked eye. This discovery clearly opens the door to completely new types of sensing from magnetic nanoparticles.

## Collective excitations and fine structure in $\alpha$-Fe$_2$O$_3$ nanoparticles

Antiferromagnets traditionally offer foundational opportunities for investigating collective excitations like excitons and magnons as well as features like magnon sidebands that arise from charge-spin coupling [160, 352, 356]. The latter arises from the dipole-allowed combination of an exciton and a magnon ($\omega_{MS} = \omega_E + \omega_M$) and is commonly observed on the leading edge of a $d$-to-$d$ band. [79, 159, 162, 352, 356] Exciton splitting and magnon sideband trends are incisive probes of symmetry, and their behavior can even be used to develop temperature-magnetic field phase diagrams. [79,159,357] While much is known about excitons, magnons, and magnon sidebands in antiferromagnets under external stimuli, there have been few opportunities to reveal finite length scale effects on the behavior of collective excitations. Our suite of hematite nanoparticles provides a superb platform for such tests. [159, 162, 358]

Figure 5.6 summarizes how the collective excitations in nano-hematite change with size. An obvious linear correlation exists between particle size and magnon sideband position in the absence of magnetic field [Figure 5.6 (a, d)]. As particle size decreases, the frequency of the magnon sideband is reduced. This trend is due to the combined size dependence of the exciton and magnon that compose it and, in the discussion below, we separate the two effects. The magnon sideband position also softens through the field-driven spin-flop transition [Figure 5.6 (b)]. The degree to which the field-induced softening of the magnon sideband $\Delta\omega_{MS}$ depends upon size is interesting [Figure 5.6 (e)]. $\Delta\omega_{MS}$ increases linearly in the small size regime but
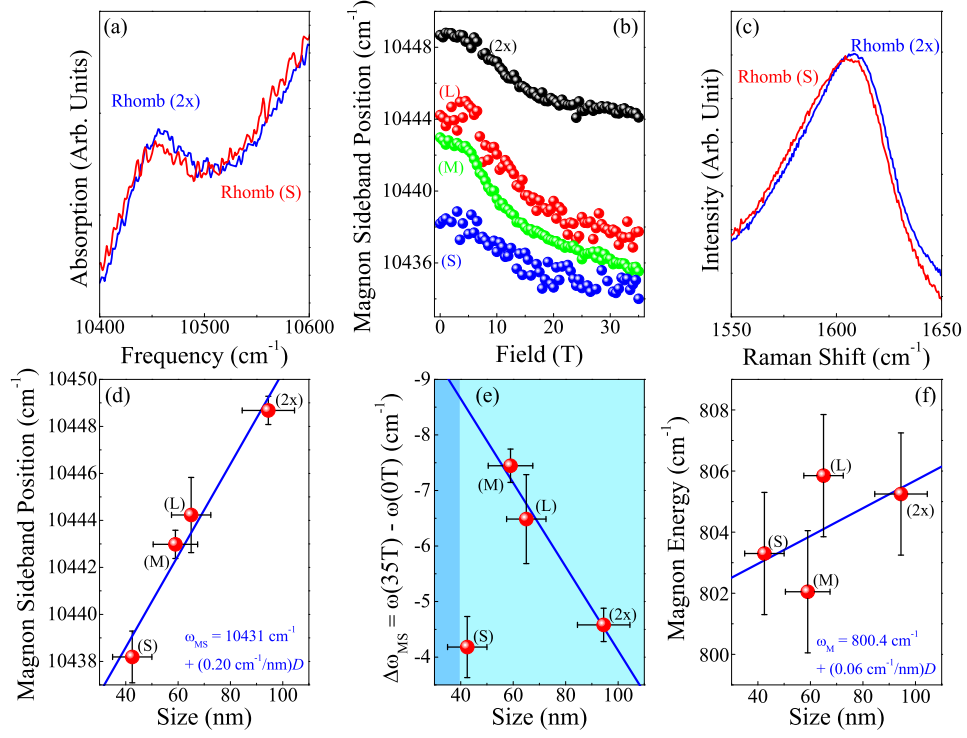
Figure 5.6: (a) Magnon sideband for the (blue) largest and (red) smallest rhombohedra. (b) Magnon sideband position vs. field for the rhombohedral samples at 4.2 K. (c) Raman-active two magnon mode for the (blue) largest and (red) smallest rhombohedra at 300 K from which the magnon energy was determined. (d) Magnon sideband position vs. particle size at 4.2 K and zero field. The equation reveals the limiting "zero size" value of the magnon sideband position and its systematic shift with particle size $D$ in nanometers. (e) Change in magnon sideband position at 35 T vs. size. Note that the smallest size particles are close to the super-paramagnetic region. (f) Magnon energy vs. size. The limiting "zero size" position of the magnon and estimated linear size-dependent shift are extracted from the indicated fit. The sample specifications are given in Table 5.2.

weakens again as the super-paramagnetic regime is approached. This is because only a remnant of the spin-flop transition survives below the super-paramagnetic limit, a situation that we already established as inconsistent with maximum spin-charge coupling. [166, 359]

Magnons are a type of spin wave commonly found in magnetic materials [360,361] and are typically explored with neutron and Raman scattering techniques. The two-magnon mode, in particular, is Raman-active. [362, 363] It is straightforward to estimate the magnon frequency $\omega_M$ from measurements of the two magnon mode as $\omega_{2M} = 2\omega_M$. In $\alpha$-Fe$_2$O$_3$ single crystals, this yields $\omega_M = 782$ cm$^{-1}$. [152, 159, 164] Figure 5.6 (c, f) displays the Raman-active two-magnon peak and the size dependence of $\omega_M$. At least within the rhombohedral sub-class, $\omega_M$ is nearly rigid. [364] Since $\omega_{MS} = \omega_E + \omega_M$, simple subtraction reveals that the exciton frequency must also decrease as particle size is reduced. We find $\omega_E = 9631 + (0.14 \text{ cm}^{-1}/\text{nm})D$, where $D$ is particle size in nanometers. Comparison of the relative slopes reveals that the exciton is much more sensitive to size than the magnon. [365]

# Chapter 6

# Pressure-induced magnetic crossover driven by hydrogen bonding in $\mathrm{CuF_2(H_2O)_2}$(3-chloropyridine)

$\mathrm{CuF_2(H_2O)_2}$(3-chloropyridine) displays a buckled network of intermolecular hydrogen bonds between the $\mathrm{H_2O}$ ligands and fluoride centers that act as superexchange linkages between the copper centers, facilitating antiferromagnetic ordering below 2.1 K [82]. Compression drives a crossover to a ferromagnetic state, [83] although the exact mechanism is not known. Our analysis of the high pressure vibrational properties reveals that compression creates new intermolecular hydrogen bonds between chlorine on the pyridine ring and the hydrogen centers on the water ligands, leading to a three dimensional hydrogen bonding network. The increased superexchange dimensionality drives the 0.8 GPa magnetic crossover. Further compression reveals another distortion between 4 and 5.5 GPa involving the bipyramidal copper

environment, although it is not known whether there is a magnetic component.

## 6.1 Spectroscopic signatures of pressure-induced structural distortions

Close-up views of the infrared and Raman spectra of $CuF_2(H_2O)_2$(3-chloropyridine) between ambient pressure and 1.5 GPa are displayed in Fig. 6.1 (a,c). Both sets of spectra show signatures of the 0.8 GPa transition. With increasing pressure, the 125 cm$^{-1}$ infrared active lattice mode diminishes and then disappears. The displacement pattern for this mode is highly collective and involves the F-Cu-F symmetric stretch, the O-Cu-O asymmetric bend, and libration of the 3-chloropyridine ring around the C-Cl bond. Turning to the Raman response, a shoulder around 1575 cm$^{-1}$, which we assign as a combination of C=C and C-N in-phase, in-plane stretches and C-Cl rocking motion, also diminishes and then disappears. Figure 6.1 (b,d) shows frequency versus pressure plots for these structures. Their disappearance through the 0.8 GPa transition indicates that the lattice is sensitive to the magnetic crossover, a sign of magnetoelastic coupling. [220, 287, 366, 367] Note that we employ room temperature, high pressure data to understand the low temperature response because the spectra are nearly insensitive to temperature. [368]

We carried out lattice dynamics calculations in order to assign the vibrational modes of $CuF_2(H_2O)_2$(3-chloropyridine) and relaxations to model structural changes between the low-pressure antiferromagnetic and high-pressure ferromagnetic states [Fig. 6.2 (a-c)]. [83] Our calculations predict that the ferromagnetic state becomes energetically favorable above 0.75 GPa, in excellent agreement with the 0.8 GPa crossover found experimentally. As anticipated, most interatomic distances decrease under compression. The drastic decrease in the O-H···Cl distance with pressure is
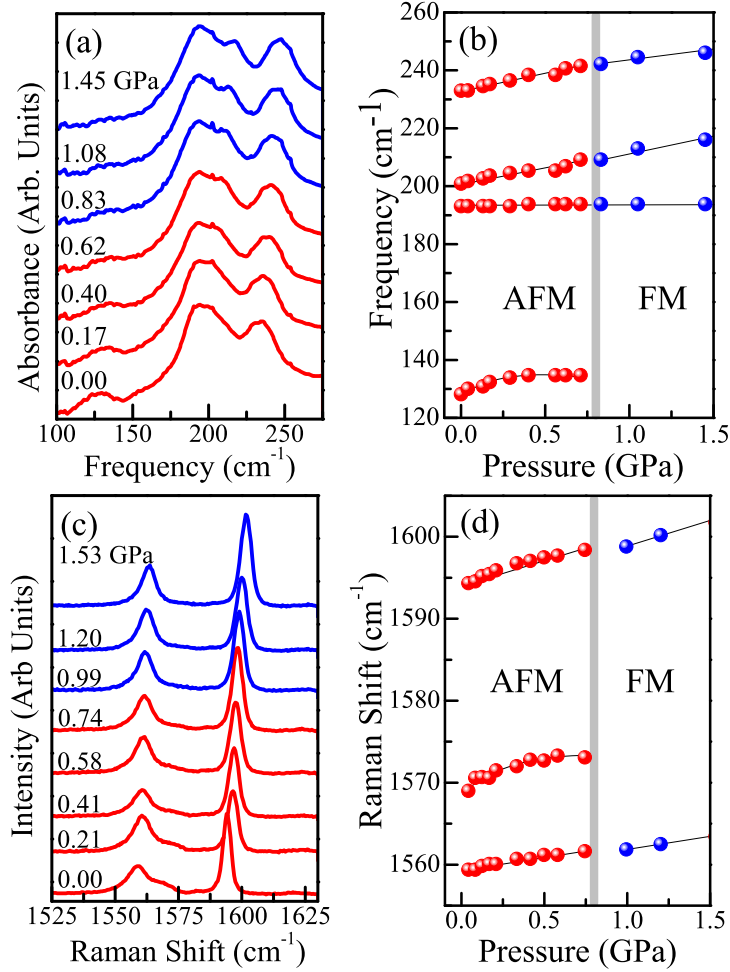
Figure 6.1: (a) Infrared spectra of $CuF_2(H_2O)_2$(3-chloropyridine) at 300 K and various pressures demonstrating the disappearance of the 125 $cm^{-1}$ lattice mode through the 0.8 GPa transition. (b) Frequency versus pressure for the infrared active modes in panel (a). (c) Room temperature Raman spectra at the indicated pressures showing the disappearance of a shoulder around 1565 $cm^{-1}$. (d) Frequency versus pressure for the Raman active modes in panel (c). The vertical grey line marks the critical pressure for the 0.8 GPa magnetic crossover.

66
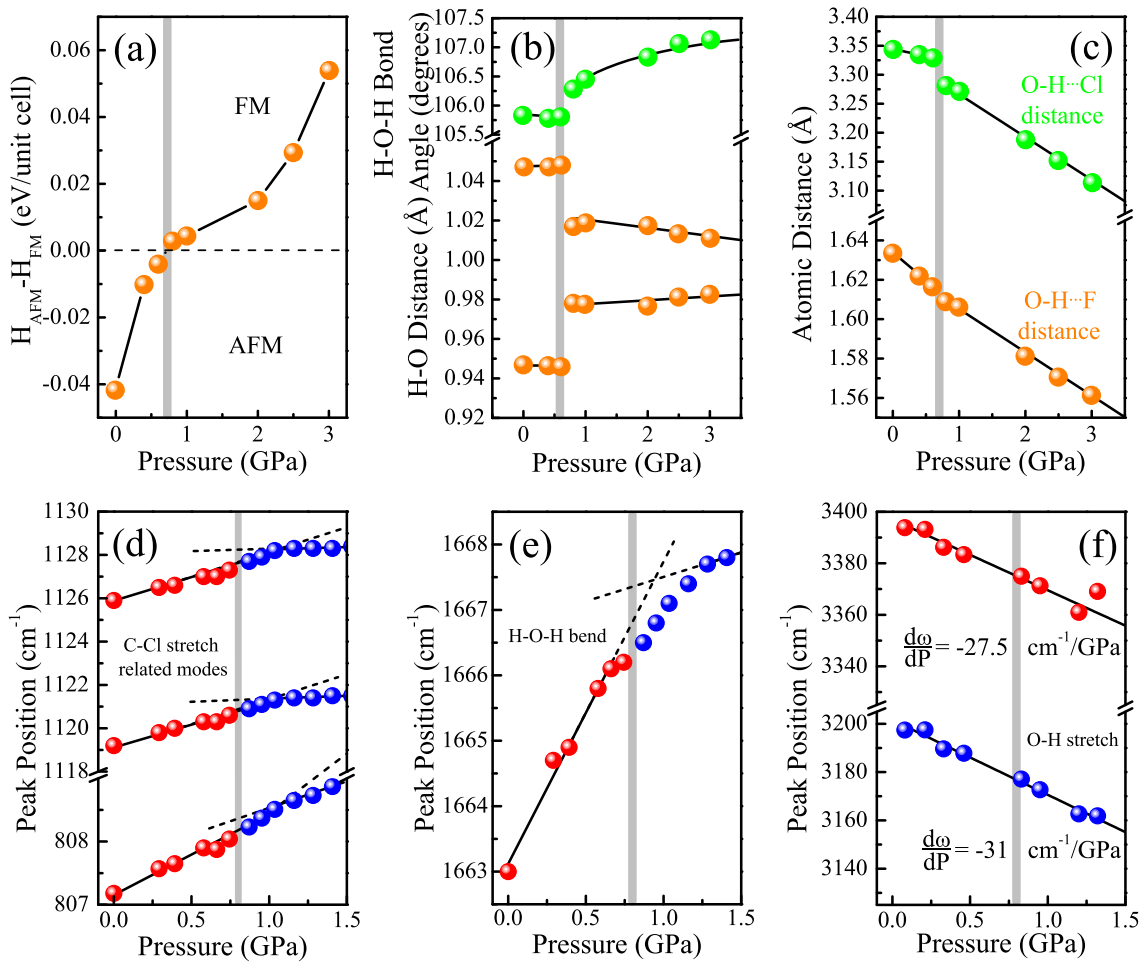
Figure 6.2: (a) Relative enthalpy of the $CuF_2(H_2O)_2$(3-chloropyridine) unit cell, predicting that the ferromagnetic state becomes energetically favored. (b) Calculated H-O bond distances and H-O-H bond angle and (c) H···F and H···Cl distances all indicate sharp changes at the critical pressure. The grey lines indicate the transition pressure which is in excellent agreement with the experimental pressure (0.75 vs. 0.8 GPa). (d) Experimental frequency versus pressure at 300 K for three modes involving the C-Cl bond, (e) H-O-H bend, and (f) O-H stretches. All modes involving the C-Cl bond show slight increases in $d\omega/dP$ around the transition. The H-O-H bend hardens significantly with pressure. The difference in $d\omega/dP$ (-27.5 ± 2 vs. -31 ± 1 $cm^{-1}$/GPa) for the two O-H stretches results in increased splitting between the features. Lines are drawn to guide the eye and help visualize different mode behaviors through the transition.

67

particularly striking. A small discontinuity also appears at the critical pressure. Moreover, one O-H bond length is predicted to increase while the other decreases (such that they become more similar), and the H-O-H bond angle widens dramatically. Taken together, our simulations suggest that changes in the O-H···Cl distance and shape of the $H_2O$ ligands are the most important local lattice distortions through the 0.8 GPa transition.

Figure 6.2 (d-f) displays frequency versus pressure trends for three different vibrational modes: the C-Cl stretches, the H-O-H bend, and the O-H stretches. As our calculations predict, these features are sensitive to the transition. For instance, on approach to the 0.8 GPa transition, the C-Cl stretching modes blue shift with increasing pressure. Above the critical pressure, these same vibrational modes display a much smaller $d\omega/dP$, indicating the stabilization of a less compressible phase. At the same time, the H-O-H bend hardens significantly over the entire pressure range, consistent with the prediction of increasing angle. [369] There is also a notable change in slope through the transition regime. Finally, both O-H stretching features soften under pressure, although at different rates. Softening is characteristic of improved hydrogen bonding interactions, [197,370] and the divergent rates imply that the two O-H stretching modes in the water ligand are becoming more inequivalent. The latter trend is in apparent contradiction to the aforementioned prediction of one O-H bond lengthening and the other shortening. As discussed below, this observation has its origin in the breakdown of simple frequency-bond length correlations. [287,371,372]

Taken together, we find that hydrogen bonds are established between the $H_2O$ ligands and the Cl center through the 0.8 GPa magnetic transition [Fig. 6.3 (b)]. The shortened O-H···Cl distance falls within the range of a "long" hydrogen bond with chlorine, [373] which explains the hardening of the C-Cl stretching modes as the motion is dampened by the new interaction and increased stability beyond 1 GPa.
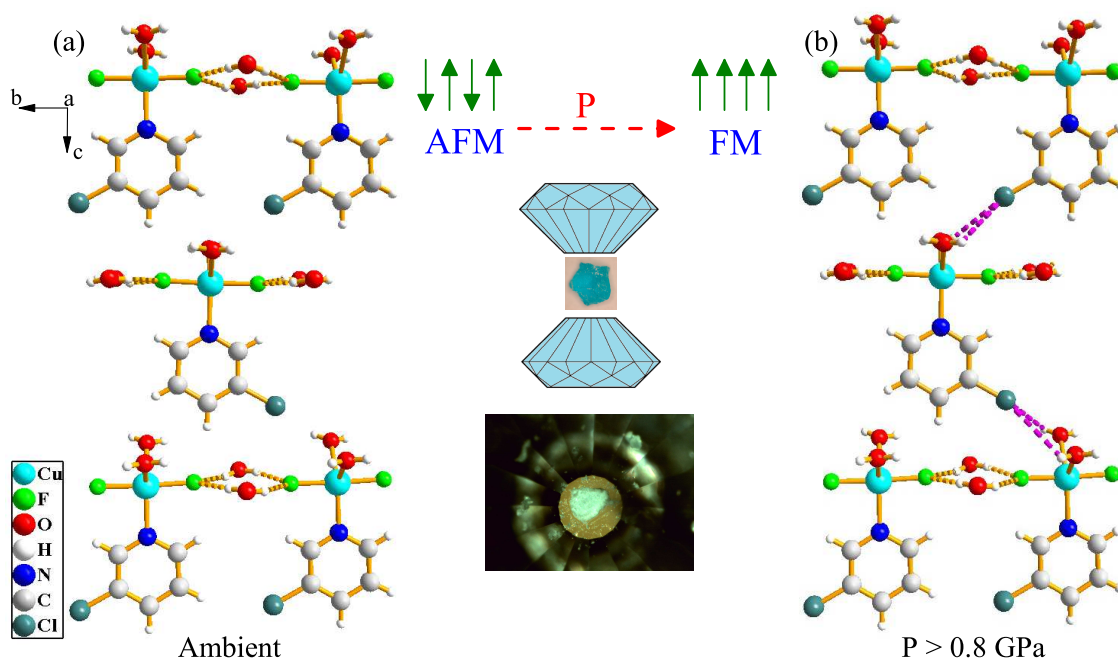
Figure 6.3: (a) Crystal structure of $CuF_2(H_2O)_2$(3-chloropyridine) at 10 K showing the buckled two-dimensional hydrogen bonded layers. [82] Parts of neighboring $CuF_2(H_2O)_2$(3-chloropyridine) molecules have been omitted to emphasize the hydrogen bonding. (b) Schematic rendering of the structure above 0.8 GPa illustrating the three dimensional network that is formed under compression. The connection in the third direction consists of intermolecular O-H···Cl hydrogen bonds, as indicated by the purple dashed lines. Also included are drawings of the pressure-induced magnetic crossover and diamond anvil cell as well as a photo of $CuF_2(H_2O)_2$(3-chloropyridine) on the diamond culet.

This interaction also accounts for the disappearance of the 125 cm$^{-1}$ infrared mode seen in Fig. 6.1 (a,b) since the O-H$\cdots$Cl hydrogen bonds prevent the 3-chloropyridine ring from librating. Since the chlorine center is closer to one hydrogen than the other, the hydrogen bond forces the H-O-H angle to open, dampening the bending motion. This process hardens the H-O-H bending mode. What is formed in the end is essentially an asymmetric pair of O-H bonds (from the point of view of a single $H_2O$ ligand), in excellent agreement with our calculations (Fig. 6.2). The establishment of new hydrogen bonding also accounts for the prediction of one O-H bond lengthening and the other shortening [Fig. 6.2 (b)]. As the hydrogen closer to the chlorine is pulled away from the oxygen center, the bond length of the second O-H linkage ought to be reduced as the electrostatic repulsion is lessened. The intermolecular O-H$\cdots$Cl hydrogen bond also shifts the electron density of the oxygen towards chlorine, effectively reducing bond order between the oxygen and the hydrogen center that is not interacting with the chlorine. This is evidenced in our spectra by increased splitting between the two O-H stretching modes as pressure is applied (-27.5 $\pm$ 2 vs. -31 $\pm$ 1 cm$^{-1}$/GPa).

## 6.2 Hydrogen bond network dimensionality controls magnetic crossover

We propose that intermolecular hydrogen bonding between the water ligand and chlorine acts as an additional superexchange pathway between copper centers along the $c$ axis, adding a third dimension to the hydrogen bonding network in $CuF_2(H_2O)_2$(3-chloropyridine) above 0.8 GPa [Fig. 6.3 (b)]. Once established, this supplemental linkage, combined with improved in-plane superexchange (due to shorter distances between F centers and H-O$\cdots$), facilitates the pressure-induced antiferromagnetic to

ferromagnetic crossover. [374] Since the 0.8 GPa magnetic crossover is driven by these local lattice distortions, the transition should be considered magnetoelastic rather than purely magnetic. [375–377] Moreover, the crossover is an excellent illustration of how pressure-induced changes in bond lengths and angles modify the transfer integral $t$ which in turn modifies the exchange interaction $J$. [220,235] In this case, the mechanism even changes the sign of $J$.

While the 0.8 GPa magnetic crossover in $CuF_2(H_2O)_2$(3-chloropyridine) was previously identified, [83] there has been no investigation of structure at higher pressures. We extended our work up to 8 GPa and discovered an additional rather sluggish structural transition between 4 and 5.5 GPa (Fig. 6.4). The low frequency Raman spectra are the most revealing in this regard. The appearance of five new modes, along with mode splitting at 120 cm$^{-1}$ and the disappearance of the 85 cm$^{-1}$ mode, signal the transition. The infrared-active modes show similar behavior in this pressure range (not shown). [289] While we cannot precisely assign the new modes that appear, our dynamics calculations show that, in general, modes below 500 cm$^{-1}$ are related to motion around the copper center, and those above 500 cm$^{-1}$ are related to the 3-chloropyridine ring. Therefore, we conclude that this higher pressure distortion involves mostly the bipyrimidal copper environment, not the 3-chloropyridine ring. The increase in the number of vibrational modes through the transition indicates an overall reduction in symmetry around the copper center. [378] X-ray diffraction will be needed to identify the space group of the high pressure phases.
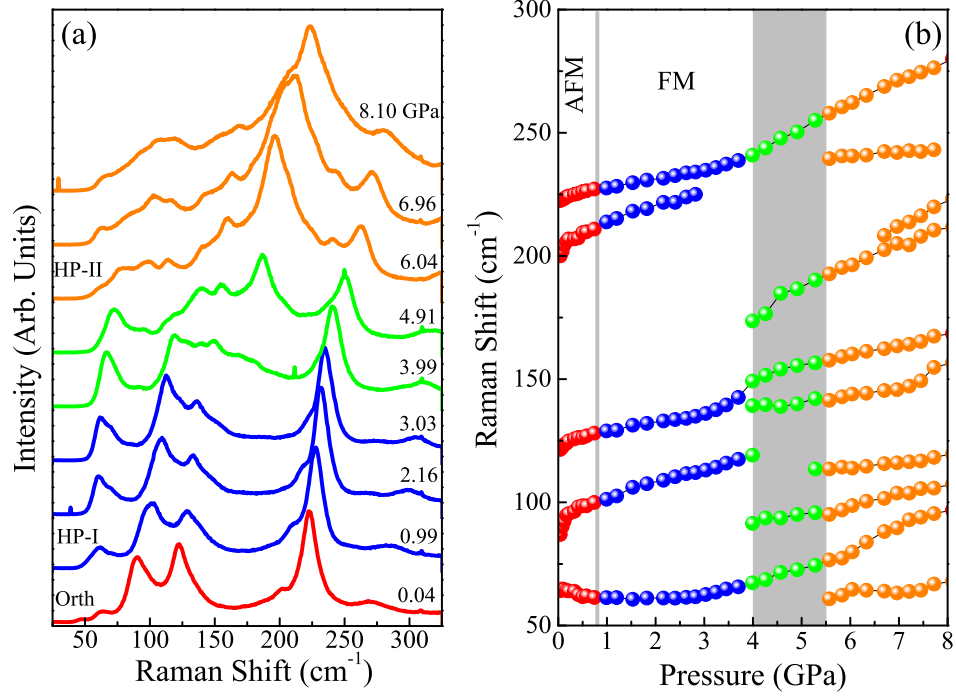
Figure 6.4: (a) Raman spectra as a function of pressure. The change in line color denotes a new phase (or coexistence of phases). (b) Raman shift versus pressure over the full pressure range investigated. The critical pressures are marked with grey vertical bands. The orthorhombic to high pressure phase I transition is at 0.8 GPa, and the broad transition with the coexistence of high pressure phases I and II is between 4 and 5.5 GPa. Here, Orth is *Pmna* orthorhombic (although at low temperature, the material is $P2_1/c$ monoclinic in this regime), [82] HP-I is the first high pressure phase, HP-II is the second high pressure phase, AFM is antiferromagnetic, and FM is ferromagnetic. The magnetic phases are present at low temperature.

## 6.3 Consequences of the magnetic crossover for piezomagnetic applications

Having established the primary role of pressure-induced local lattice distortions in creating new hydrogen bonding pathways which in turn drive the antiferromagnetic to ferromagnetic crossover in $CuF_2(H_2O)_2$(3-chloropyridine), we turn our attention toward prospects for control. One of the most important criteria in this regard is reversibility. As revealed by Fig. 6.5, the process is indeed reversible. Hydrogen bond networks form, diminish, and repeatedly reform under pressure. This implies that magnetism, which is determined by the dimensionality of the hydrogen bonding network that provides for superexchange between copper centers, is equally switchable. Whether this process can be demonstrated in thin film form and under lattice strain is an open question, but similar mechanisms involving coordinated motion of hydrogen bond networks that function as exchange pathways between magnetic cen-
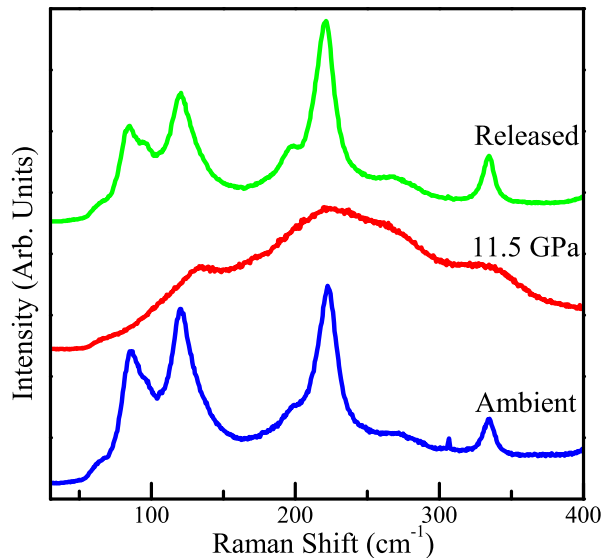


Figure 6.5: Raman spectra at ambient conditions (blue), 11.5 GPa (red), and after the release of pressure (green). The ambient and released pressure spectra are nearly identical, demonstrating the lack of hysteresis.

ters are likely to play out in other quantum magnets. A secondary criteria is room temperature operation. The O-H···Cl connections in $CuF_2(H_2O)_2$(3-chloropyridine) are robust at 300 K. However, these connections only function as superexchange linkages at low temperature. We therefore anticipate that pressure- or strain-controllable exchange interactions [379] can be realized only below the ordering temperature, although short range interactions might increase the operating temperature by a few degrees. Materials like $V(TCNE)_x \cdot y(CH_2Cl_2)$ and $(Et_4N)_{0.5}Mn_{1.25}[V(CN)_5]\cdot 2H_2O$ may offer pressure- and/or strain-driven switchability at high temperatures. [380,381] Spin-crossover materials may be good candidates as well. Finally, this kind of cooperative functionality is not limited to piezomagnetism. Low power piezoelectric devices may also be possible if magnetoelectric coupling can be made strong enough. [382]

# Chapter 7

# Competing magnetoelastic phases in a semiclassical system

Quantum phase transitions are quite different than classical transitions in that they are driven by external stimuli such as magnetic field, pressure, or composition rather than by thermal fluctuations. One characteristic feature of this type of transition is the quantum critical point near which exotic properties often emerge. $M[\text{N(CN)}_2]_2$ with $M = \text{Mn}$ is particularly rich in this regard. This system sports a variety of quantum phases at experimentally-realizable magnetic fields and pressures. Moreover, delicately balanced energies create an exotic pressure-temperature-magnetic field phase diagram where small external perturbations change important energy and length scales to favor one phase over another. Although high-spin $S = 5/2$ Mn(II) is commonly considered a classical ion, several states driven by pressure and magnetic field are supported by cooperative structural distortions and exhibit quantum properties. These findings highlight the importance of spin-lattice coupling in quantum phase transitions and invalidate the usual classical treatment of Mn(II).

## 7.1 Revealing the mechanisms of the of structural phase transitions

Figure 7.1 displays close-up views of the Raman response of $Mn[N(CN)_2]_2$ as a function of pressure at 100 K. The majority of features display traditional compression-induced hardening, [227] so we focus on the behavior of the octahedral rotations, the lowest frequency lattice modes, the C≡N-C ligand bend, and the C≡N stretch as most significant. Peak position vs. pressure plots along with a frequency shift and splitting pattern analysis reveal a series of pressure-induced structural phase transitions at 0.2, 1.3, and 3.0 GPa. In order to simplify our discussion of the structural distortions, we designate the phases as $\alpha$, $\alpha'$, $\gamma$, and $\delta$ from lowest to highest pressure. The sharp $\alpha \rightarrow \alpha'$ transition at $P_{C1} = 0.2$ GPa takes place within the orthorhombic $Pnnm$ space group. It involves only local distortions in the $MnN_6$ environment as indicated by a hardening of the 50 $cm^{-1}$ mode associated with octahedral rotation around $c$ and a change in slope of the 80 $cm^{-1}$ equatorial out-of-phase N-Mn-N bending mode. The more gradual $\alpha' \rightarrow \gamma$ crossover at $P_{C2} = 1.3$ GPa is signalled by the disappearance of the 50 $cm^{-1}$ octahedral rotation around $c$ and splitting of the 2190 $cm^{-1}$ C≡N stretch. Finally, the $\gamma \rightarrow \delta$ crossover near $P_{C3} = 3.0$ GPa is identified by splitting of the mode at 120 $cm^{-1}$, a significant width enhancement of the C≡N-C bending mode near 680 $cm^{-1}$ that we attribute to weak splitting, and rigidity in the 2260 $cm^{-1}$ overtone. As discussed below, $P_{c2}$ and $P_{C3}$ have important effects on the crystal symmetry and magnetic properties. [227]

We extended these high pressure Raman scattering measurements and the analysis shown in Fig. 7.1 to include several temperatures between 100 and 300 K. In each case, we are able to identify a series of three critical pressures. As before, the $\alpha \rightarrow \alpha'$ transition is sharp whereas the $\alpha' \rightarrow \gamma$ and $\gamma \rightarrow \delta$ crossovers take place continuously
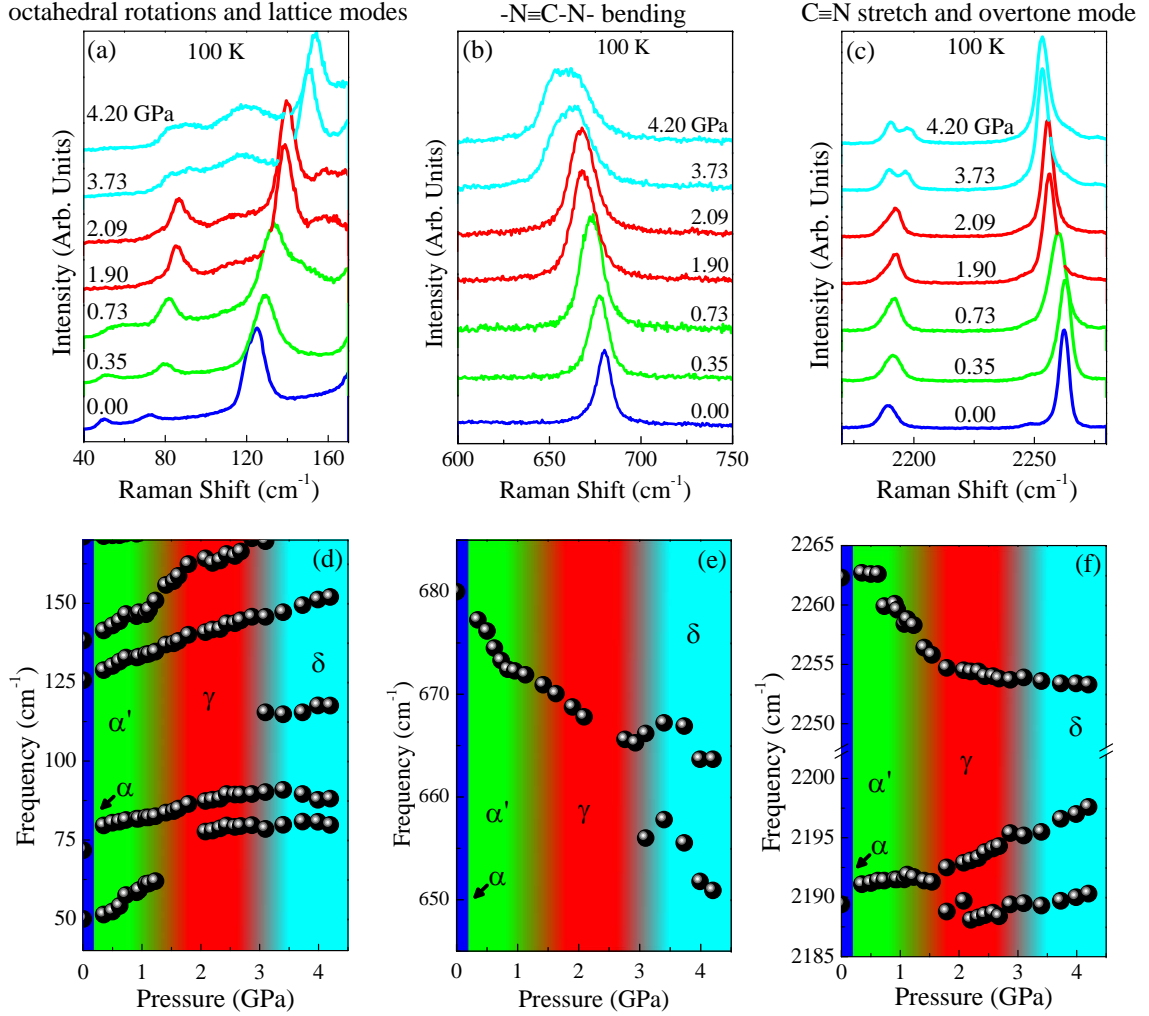
Figure 7.1: (a-c) Close-up views of the 100 K Raman spectra of Mn[N(CN$_2$)]$_2$ as a function of pressure. (d-f) Frequency vs. pressure for the modes displayed in (a-c) from which we determine the critical pressures. Line and background colors correlate with well-defined phases. Here, blue, green, red, and cyan represent the ambient pressure orthorhombic ($Pnnm$) $\alpha$ phase and the high pressure $\alpha'$, $\gamma$, and $\delta$ phases, respectively. The blending near $P_{C2}$ and $P_{C3}$ indicates the range over which the structural distortions take place.

77

over a much broader range. Figure 7.2 displays the pressure-temperature phase diagram of $Mn[N(CN)_2]_2$. We immediately notice that the phase boundaries corresponding to these structural distortions have positive $\partial P/\partial T$'s, although that associated with $P_{C3}$ is the most responsive. That $\partial P/\partial T > 0$ and $(\partial P/\partial T)_V = -(\partial S/\partial V)_T$ indicates that entropy is increasing as the system becomes more disordered through each successive structural transition. Moreover, the phase boundaries drive toward a very interesting set of magnetic states at low temperature.

In order to unveil the mechanism behind this series of structural phase transitions, we performed first-principles calculations of $Mn[N(CN)_2]_2$ under isotropic compression and compared our predictions with the experimental results [Fig. 7.3 (a,b)]. Our calculations reveal three octahedral rotational modes [Fig. 7.3 (c-e)], two of which
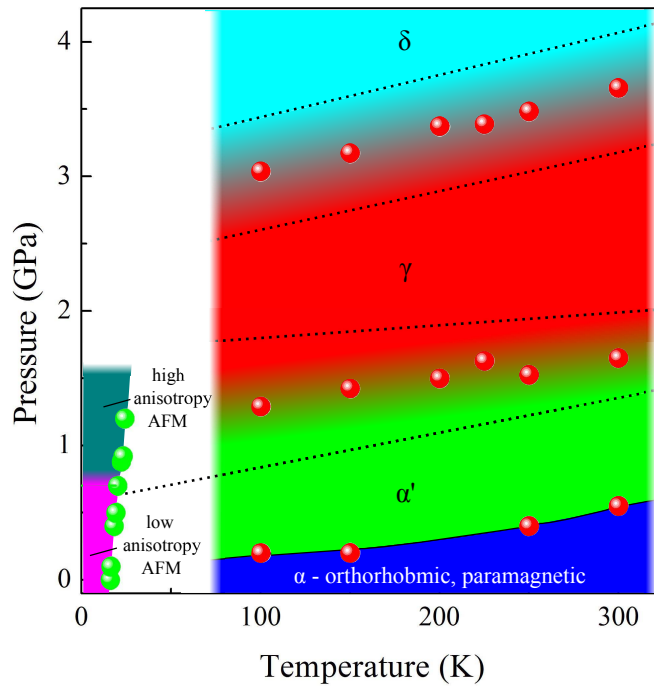


Figure 7.2: Pressure-temperature phase diagram of $Mn[N(CN)_2]_2$ obtained by combining the critical pressures determined by Raman scattering (red points) with magnetic properties data (green points) from Ref. 45. The blue, green, red, and teal regions correspond to the $\alpha$, $\alpha'$, $\gamma$, and $\delta$ phases, respectively. The breadth of the phase boundaries near $P_{C2}$ and $P_{C3}$ is indicated by blending between the dotted lines.
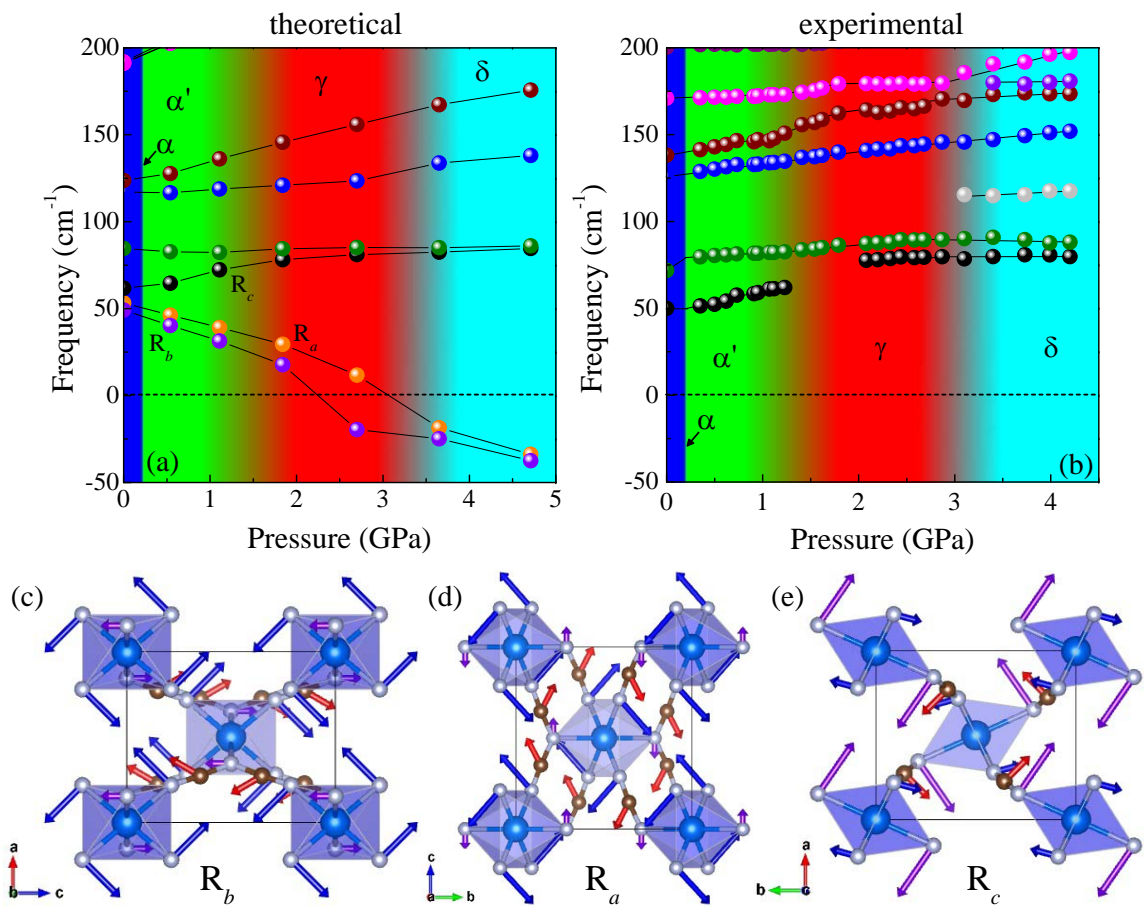
Figure 7.3: a) Calculated and (b) experimental frequency vs. pressure trends for the low frequency Raman-active modes of $Mn[N(CN)_2]_2$. Colored regions correspond to various phases as labeled, with blended areas indicating gradual crossovers. (c-e) Displacement patterns for the octahedral rotation modes around $b$, $a$, and $c$.

strikingly become unstable under pressure. These soft modes drive permanent lattice distortions and are responsible for the structural phase transitions at $P_{C2}$ and $P_{C3}$ in $Mn[N(CN)_2]_2$. By contrast, the transition at $P_{C1}$ is a local distortion and therefore is not associated with a soft mode. The soft modes predicted to appear at 49 and 53 cm$^{-1}$ are unfortunately not observed in our experiments because (i) the features overlap and (ii) the calculated matrix elements are very small (0.018 and 4.43 compared to $\approx$44 for the 120 cm$^{-1}$ lattice mode). This highlights the role of predictive theory in unraveling precisely how and why a phase transition takes place.

Overall, the predicted critical pressures are in excellent agreement with the sequence of structure phase transitions displayed in the $P$-$T$ phase diagram [Fig. 7.2]. The octahedral rotation around $b$ [R$_b$ in Fig. 7.3 (c)] is predicted to become imaginary at 2.2 GPa, near the observed $\alpha' \to \gamma$ crossover at $P_{C2} = 1.3$ GPa. The $MnN_6$ rotation about the $a$ axis [R$_a$ in Fig. 7.3 (d)] is predicted to go soft at 3.1 GPa, very close to the $\gamma \to \delta$ crossover at $P_{C3} = 3.0$ GPa. Finally, we point out that the ambient structure is already displaced through the octahedral rotation around $c$ [R$_c$ in Fig. 7.3 (e)], and therefore the $MnN_6$ rotational mode observed at 50 cm$^{-1}$ does not go soft [Fig. 7.3 (a,b)]. Trends in the lattice and localized modes are reproduced as well, [227] although small discrepancies arise from carrying out our calculations under constant symmetry. A similar sequence of soft mode-driven transitions trigger the pressure-induced magnetic crossovers in $Co[N(CN)_2]_2$ [237] and may be important in other hybrid systems like the metal-organic framework multiferroics. [383]

## 7.2 Structural phase transitions trigger new magnetic states

This series of pressure-driven structural distortions has important implications for low temperature magnetism. The connection is readily apparent from the $P$-$T$ phase diagram, where we see that $Mn[N(CN)_2]_2$ sports at least two long-range ordered magnetic states that differ in their anisotropy. [45] Extrapolating the pressure-induced structural transitions [indicated by dotted lines in Fig. 7.2] to base temperature reveals that the low pressure edge of the $\alpha' \rightarrow \gamma$ transition directly encounters the magnetic phase boundary, suggesting that it triggers the anisotropy crossover. This sort of direct connection from simple inspection of the phase diagram is not often apparent. Our calculations also link the $\alpha' \rightarrow \gamma$ structural phase transition and the magnetic anisotropy crossover. Figure 7.4 displays two of the important angles in the Mn-N≡C-N-Mn superexchange pathway and the corresponding exchange interaction between metal centers ($J$) as a function of pressure. These values are computed in two different magnetic planes. Strikingly, we predict the development of two unique Mn-N≡C-N-Mn bridges under pressure (in agreement with our spectral findings), an unprecedented change in the Mn-N-C bond angle (by more than $\pm 20°$), and a consequent splitting of $J$ in the $\gamma$ phase. These two different exchange interactions arise due to the octahedral rotations. Although we predict that the system remains orthorhombic, the two unique $J$ values are consistent with a change in exchange anisotropy. We therefore conclude that structural distortions across the $\alpha' \rightarrow \gamma$ crossover drive the anisotropy enhancement [45] in the $\gamma$ phase.

The temperature dependence of the $\gamma \rightarrow \delta$ crossover provides compelling evidence for an unexplored low temperature magnetic phase near 3 GPa. Our calculations predict that the 53 cm$^{-1}$ soft mode [$R_a$] drives the system to a monoclinic space group,
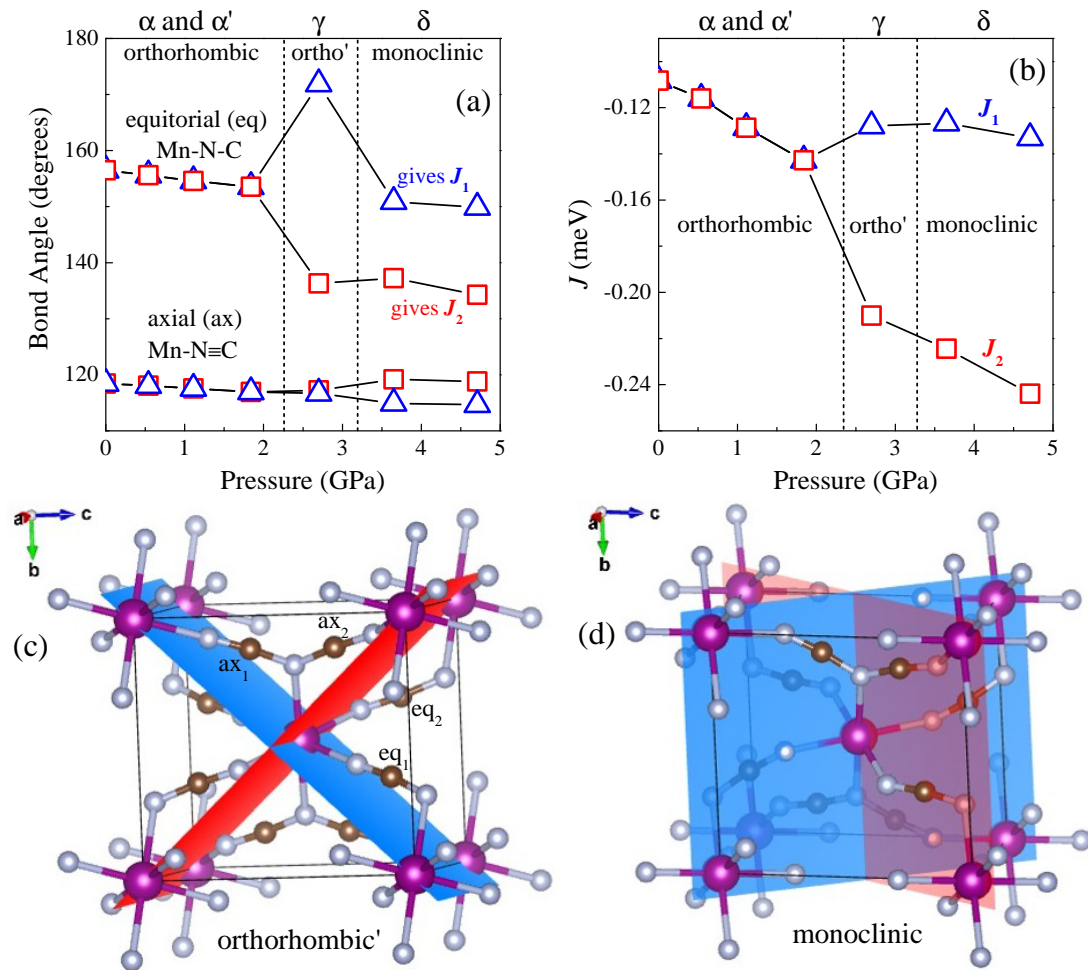
Figure 7.4: Calculated (a) Mn-N≡C and Mn-N-C angles and (b) $J$ vs. pressure. $J_1$ ($J_2$) is the exchange interaction of spins located in the blue (red) plane of (c) the orthorhombic' $\gamma$ and (d) monoclinic $\delta$ phases. The exchange interactions in both the $\gamma$ and $\delta$ phases support G-type antiferromagnetism on a bipartite lattice. The blue and red magnetic planes (associated with $J_1$ and $J_2$) rotate by 90° in a cooperative manner across the structural transition.

82

consistent with the appearance of new spectral features. As seen in Fig. 7.4 (a), the 120° Mn-N≡C angle splits into two, giving a total of four unique superexchange angles in the $\delta$ phase. This is also in line with splitting of the N≡C-N ligand bending mode around 680 cm$^{-1}$ [Fig. 7.1 (b,e)]. The $\delta$ phase is therefore predicted to display two unique $J$ values [Fig. 7.4 (b)] that become more distinct under compression. Another intriguing aspect of the $\gamma \rightarrow \delta$ transition in Mn[N(CN)$_2$]$_2$ is that it takes place with a 90° reorientation of the unique exchange planes [Fig. 7.4 (c,d)]. According to our calculations, this unusual exchange plane reorientation is a consequence of the 90° separation of the rotation axes of the R$_b$ and R$_c$ soft modes that define the structural phases. High pressure magnetization or inelastic neutron scattering may be able to detect this exotic reorientation and the effect on the microscopic spin arrangement.

## 7.3 Revealing the rich $P$-$T$-$B$ phase diagram of Mn[N(CN)$_2$]$_2$

Pressure and temperature are not the only external stimuli that support new states of matter in Mn[N(CN)$_2$]$_2$. Applied magnetic field drives a spin-flop transition [241] and ultimately a transition to the fully polarized state that is stabilized by lattice distortions. [20] Here, field suppresses the quantum fluctuations associated with the canted antiferromagnetic state to saturate the magnetization above 30 T. Bringing these results together with our current effort yields an extraordinarily rich $P$-$T$-$B$ phase diagram [Fig. 7.5] with a surprising number of competing magnetostructural phases. This complexity arises from the delicate balance of interactions in Mn[N(CN)$_2$]$_2$ and makes it possible for small external perturbations to modify the important energy scales and mixing processes, driving the system into new phases with unique proper-

ties. What makes this particular *P-T-B* phase diagram especially fascinating is the prospect that many of these phases may host quantum properties and that some of the boundaries may in fact be quantum phase transitions.
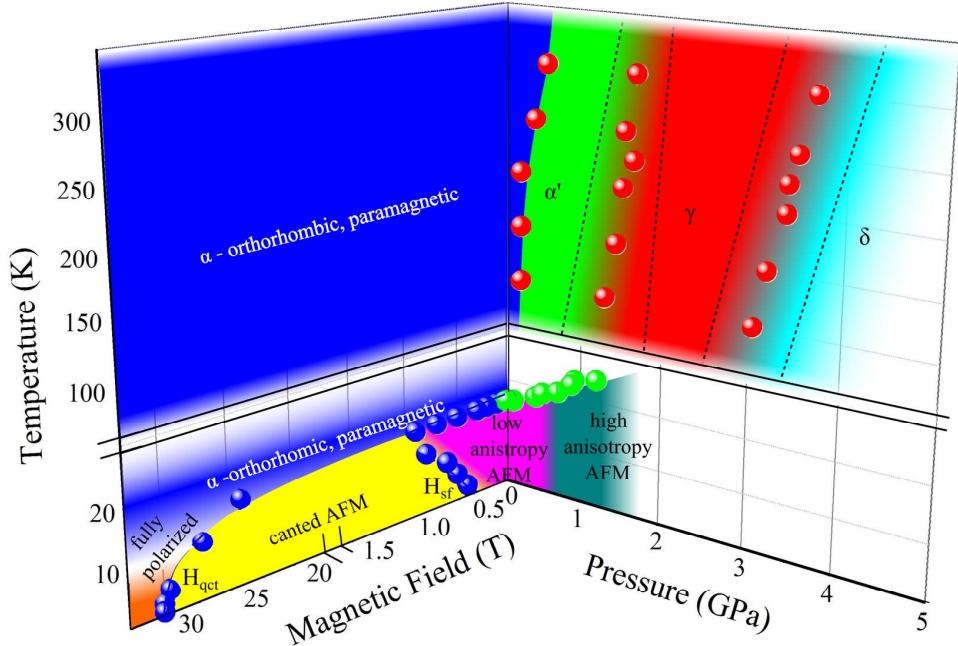


Figure 7.5: Pressure-temperature-magnetic field phase diagram of $Mn[N(CN)_2]_2$ created by combining our findings with prior magnetic and vibrational properties work. [45, 227, 235, 241] The color scheme in pressure space matches that in prior figures, and blended areas denote extended transition regimes. The structural and magnetic phases are labeled.

The possibility that $Mn[N(CN)_2]_2$ may be a quantum material is an interesting surprise. High spin Mn(II) is typically described as a semi-classical or solely classical ion because spin is large ($S=5/2$), single ion anisotropy is low, and quantum fluctuations (which go as $1/S$) tend to be small - especially compared to Mn(III) and Mn(IV). [384] That said, dicyanimide is a high anisotropy ligand and is intimately involved in establishing the different Neél states under pressure. These antiferromagnetic states are unequivocally quantum in nature since they are not eigenstates of the Hamiltonian. Moreover, our calculations predict that Dzyaloshinskii-Moriya interactions grow with decreasing bond angle [Fig. 7.4 (a)]. The magnetostructural

phase diagram and mechanisms revealed here suggest the possibility that a number of the states and phase transitions in $Mn[N(CN)_2]_2$ may in fact have quantum aspects. We argue here that the $T = 0$ pressure-induced transitions are quantum in nature and are associated with the softening of phonon modes.

We also emphasize that the magnetostructural coupling mechanisms discussed here are intrinsic to molecular materials and, in addition to being important features of $Mn[N(CN)_2]_2$, fulfill the promise of hybrid transition metal-organic materials - many of which also contain Mn(II). Multiferroic $[(CH_3)_2NH_2]Mn(HCOO)_3$ is a superb example. [383, 385–387] One instance of a Mn(II) system where quantum spin fluctuations are observed is $Mn_{1-x}Co_xWO_4$, which undergoes a series of ferroelectric phase transitions into states where the magnetic spin cycloid is eccentric with a ratio of short-to-long spins of $\approx 0.8$. [388] Because higher harmonics associated with easy-axis anisotropy are absent, this eccentricity must be caused by quantum spin fluctuations. Similar quantum phenomena may emerge in other purely Mn(II) systems. [389–394] $Mn(TCNE)[C_4(CN)_8]_{1/2}$, for instance, displays a pressure-induced antiferromagnetic to ferrimagnetic transition that merits additional investigation in this regard. [394] The competing phases of these and other materials suggest that despite the classical (or semi-classical) nature of the magnetic ion, Mn(II)-containing systems may provide an interesting new platform for exploring quantum materials.

# Chapter 8

# Summary and Outlook

In this dissertation, I present spectroscopic investigations of materials under extreme conditions. Our target systems focus on functional nanomaterials and molecule-based magnets that offer opportunities to explore properties through various phase transitions driven by size, temperature, magnetic field, and pressure. These findings are important for understanding and developing novel multifunctional materials.

The first problem focuses on size effects on the properties of nanomaterials. Using high pressure vibrational spectroscopy we investigate the breakdown of $WS_2$ nanotubes under compression. Our spectra reveal that the $A_{1g}$ phonon is twice as sensitive to compression as any other mode, making it a strong candidate for the breakdown pathway. Scanning electron microscope images of nanotubes after compression to 20 GPa confirm that the tubes fracture along the direction of this displacement, and reveal that the fracture begins in the outer layers and propagates inwards. Moreover, the infrared spectra under compression surprisingly indicate percolation effects due to conductivity between the nanotubes. Knowing the microscopic mechanism of the nanotube breakdown suggests routes by which to block it. In this case, filling the hollow nanotubes with a stabilizing filler could suppress the $A_{1g}$ mode and allow the nanotubes to survive to higher pressures.

We also measured the optical properties of a suite of $\alpha$-Fe$_2$O$_3$ nanoparticles, allowing us to explore size effects on coupling processes in a well-known antiferromagnet. Oscillator strength analyses reveal that confinement drives a crossover from a phonon at 530 cm$^{-1}$ to one a 470 cm$^{-1}$ activating the formally forbidden $d - d$ excitation. We can understand that is as an anisotropic expansion of the unit cell with reduced size leading to a more three-dimensional character of the 470 cm$^{-1}$ mode at smaller sizes. We also find modifications of spin-charge coupling with reduced size; magnetic field-induced spectral contrast is enhanced upon confinement until the superparamagnetic regime is reached due to enhanced spin-charge coupling. Moreover, we discovered that both excitons and magnons red shift with reduced size in nano-$\alpha$-Fe$_2$O$_3$, although the exciton is more sensitive to particle size. This work suggests that small size may enhance color contrast in materials with other color change mechanisms and may lead to applications such as anti-counterfeiting agents.

The second problem revolves around pressure-induced structural transitions in molecule-based magnets. In order to investigate the antiferromagnetic to ferromagnetic crossover in CuF$_2$(H$_2$O)$_2$(3-chloropyridine), we measured the high pressure infrared and Raman responses. Our spectra reveal that a new hydrogen bond is formed between the 3-chloropyridine ring and the H$_2$O ligand. This reversible process increases the dimensionality of the superexchange network between copper centers and drives the magnetic crossover. Moreover, a structural transition is discovered between 4 and 5.5 GPa that mainly involves the Cu pentacoordinate environment and may also have consequences on the magnetic properties. The reversible magnetic crossover takes place at a relatively low critical pressure, hinting at possible piezomagnetic applications. While the Neél temperature of CuF$_2$(H$_2$O)$_2$(3-chloropyridine) is admittedly low, incorporating halogens onto rings of molecule-based with higher ordering temperatures may result in similar magnetic crossovers at more application-

friendly energy scales.

Combining high pressure Raman scattering with theoretical calculations revealed hidden soft modes that drive pressure-induced structural transitions in $Mn[N(CN)_2]_2$ that connect to exotic magnetic property crossovers. The strikingly complex $P$-$T$-$B$ phase diagram of $Mn[N(CN)_2]_2$ highlights the importance of molecule-based magnets in exploring phase transitions at experimentally realizable energy scales. Moreover, it contains many magnetoelastic phases that display may quantum properties. These findings therefore challenge the generally accepted classical treatment of Mn(II) and invite its reconsideration as an integral part of quantum materials.

Taken together, these comprehensive findings give insight into the interplay between spin, charge, and lattice degrees of freedom in multifunctional materials. They also provide natural scientific extensions and motivation for development of improved measurement techniques. Suppressing the breathing mode in $WS_2$ nanotubes may prevent the breakdown under shear stresses. This can be achieved by filling the nanotubes with a filler such as $C_{60}$, or by implementing a nanoscroll geometry instead of a multi-walled tube. The enhanced color contrast in $\alpha$-$Fe_2O_3$ suggests that similar size effects may appear in materials with strong field-induced color change that have not been explored at the nanoscale, such as $Ni_3V_2O_8$ or $NiFe_2O_4$. Moreover, the high pressure vibrational properties of $CuF_2(H_2O)_2$(3-chloropyridine) and $Mn[N(CN)_2]_2$ both indicate possible magnetic transitions at pressures higher than the typical 1.5 GPa limit of conventional pressure cells for magnetic properties measurements that should spur development of new high pressure techniques. Increasing this experimental limit would enable the exploration of novel phase transitions in molecule-based magnets, and open the door to probing transitions in materials with higher energy scales such as oxides.

# Bibliography

[1] I. Živković, K. Prša, O. Zaharko, and H. Berger. J. Phys. Condens. Matter, **22**, 056002 (2010).

[2] J. Nagamatsu, N. Nakagawa, T. Muranaka, Y. Zenitani, and J. Akimitsu. Nature, **410**, 63 (2001).

[3] M. K. Wu, J. R. Ashburn, C. J. Torng, P. H. Hor, R. L. Meng, L. Gao, Z. J. Huang, Y. Q. Wang, and C. W. Chu. Phys. Rev. Lett., **58**, 908 (1987).

[4] L. D. Casto, A. J. Clune, M. O. Yokosuk, J. L. Musfeldt, T. J. Williams, H. L. Zhuang, M. W. Lin, K. Xiao, R. G. Hennig, B. C. Sales, J. Q. Yan, and D. Mandrus. APL Mater., **3**, 041515 (2015).

[5] M. O. Yokosuk, S. Artyukhin, A. Al-Wahish, X. Wang, J. Yang, Z. Li, S.-W. Cheong, D. Vanderbilt, and J. L. Musfeldt. Phys. Rev. B, **92**, 144305 (2015).

[6] B. R. Jones, P. A. Varughese, I. Olejniczak, J. M. Pigos, J. L. Musfeldt, C. P. Landee, M. M. Turnbull, and G. L. Carr. Chem. Mater., **13**, 2127 (2001).

[7] G. Li, J. S. Lee, V. C. Long, J. L. Musfeldt, Y. J. Wang, M. Almeida, A. Revcolevschi, and G. Dhalenne. Chem. Mater., **10**, 1115 (1998).

[8] P. Lemmens, B. Eisener, M. Brinkmann, L. V. Gasparov, G. Güntherodt, P. v. Dongen, W. Richter, M. Weiden, C. Geibel, and F. Steglich. Physica B, **223-224**, 535 (1996).

[9] J. L. Musfeldt, Y. J. Wang, S. Jandl, M. Poirier, A. Revcolevschi, and G. Dhalenne. Phys. Rev. B, **54**, 469 (1996).

[10] P. Gegenwart, Q. Si, and F. Steglich. Nat. Phys., **4**, 186 (2008).

[11] S. Sachdev and B. Keimer. Phys. Today, **64**, 29 (2011).

[12] S. Sachdev. *Quantum phase transitions*. Cambridge University Press, Cambridge, 2nd ed. (2011).

[13] T. Furukawa, K. Miyagawa, H. Taniguchi, R. Kato, and K. Kanoda. Nat. Phys., **11**, 221 (2015).

[14] N. Büttgen, H.-A. Krug von Nidda, W. Kraetschmer, A. Günther, S. Widmann, S. Riegg, A. Krimmel, and A. Loidl. J. Low Temp. Phys., **161**, 148 (2010).

[15] H. Terletska, J. Vučičević, D. Tanasković, and V. Dobrosavljević. Phys. Rev. Lett., **107**, 026401 (2011).

[16] Z. Tian, Y. Kohama, T. Tomita, H. Ishizuka, T. H. Hsieh, J. J. Ishikawa, K. Kindo, L. Balents, and S. Nakatsuji. Nat. Phys., **12**, 134 (2016).

[17] J. Biscaras, N. Bergeal, S. Hurand, C. Feuillet-Palma, A. Rastogi, R. C. Budhani, M. Grilli, S. Caprara, and J. Lesueur. Nat. Mater., **12**, 542 (2013).

[18] P. Gegenwart, J. Custers, C. Geibel, K. Neumaier, T. Tayama, K. Tenya, O. Trovarelli, and F. Steglich. Phys. Rev. Lett., **89**, 056402 (2002).

[19] Y. I. Joe, X. M. Chen, P. Ghaemi, K. D. Finkelstein, G. a. de la Peña, Y. Gan, J. C. T. Lee, S. Yuan, J. Geck, G. J. MacDougall, T. C. Chiang, S. L. Cooper, E. Fradkin, P. Abbamonte, G. A. de la Peña, Y. Gan, J. C. T. Lee, S. Yuan, J. Geck, G. J. MacDougall, T. C. Chiang, S. L. Cooper, E. Fradkin, and P. Abbamonte. Nat. Phys., **10**, 421 (2014).

[20] T. V. Brinzari, P. Chen, Q. C. Sun, J. Liu, L. C. Tung, Y. Wang, J. A. Schlueter, J. Singleton, J. L. Manson, M.-H. Whangbo, A. P. Litvinchuk, and J. L. Musfeldt. Phys. Rev. Lett., **110**, 237202 (2013).

[21] O. Günaydın-Şen, C. Lee, L. C. Tung, P. Chen, M. M. Turnbull, C. P. Landee, Y. J. Wang, M. H. Whangbo, and J. L. Musfeldt. Phys. Rev. B, **81**, 104307 (2010).

[22] S. Sachdev. Science, **288**, 19 (2000).

[23] T. Kaneko and S. Abe. J. Phys. Soc. Japan, **20**, 2001 (1965).

[24] Y. S. Oh, S. Artyukhin, J. J. Yang, V. Zapf, J. W. Kim, D. Vanderbilt, and S.-W. Cheong. Nat. Commun., **5**, 3201 (2014).

[25] T. Inami, Y. Ajiro, and T. Goto. J. Phys. Soc. Japan, **65**, 2374 (1996).

[26] L. E. Svistov, A. I. Smirnov, L. A. Prozorova, O. A. Petronko, L. N. Demianets, and A. Y. Shapiro. Phys. Rev. B, **67**, 094434 (2003).

[27] T. Aoyama, K. Yamauchi, A. Iyama, S. Picozzi, K. Shimizu, and T. Kimura. Nat. Commun., **5**, 4927 (2014).

[28] K. R. O'Neal, Z. Liu, J. S. Miller, R. S. Fishman, and J. L. Musfeldt. Phys. Rev. B, **90**, 104301 (2014).

[29] J. B. Goodenough. *Magnetism and the chemical bond*. Interscience Publishers, New York-London (1963).

[30] X.-J. Chen, V. V. Struzhkin, Y. Song, A. F. Goncharov, M. Ahart, Z. Liu, H.-K. Mao, and R. J. Hemley. Proc. Natl. Acad. Sci., **105**, 20 (2008).

[31] Z. H. Chi, X. M. Zhao, H. Zhang, A. F. Goncharov, S. S. Lobanov, T. Kagayama, M. Sakata, and X. J. Chen. Phys. Rev. Lett., **113**, 036802 (2014).

[32] H. Cui, J. S. Brooks, A. Kobayashi, and H. Kobayashi. J. Am. Chem. Soc., **131**, 6358 (2009).

[33] A. Shinozaki, K. Mimura, T. Nishida, T. Inoue, S. Nakano, and H. Kagi. Chem. Phys. Lett., **662**, 263 (2016).

[34] R. J. Hemley. Annu. Rev. Phys. Chem., **51**, 763 (2000).

[35] M. Evangelisti, T. G. Sorop, O. N. Bakharev, D. Visser, A. D. Hillier, J. J. Alonso, M. Haase, L. A. Boatner, and L. Jos De Jongh. Phys. Rev. B, **84**, 094408 (2011).

[36] S. Thota, J. H. Shim, and M. S. Seehra. J. Appl. Phys., **114**, 2013 (2013).

[37] Z.-Q. Li, L. Zhang, Y. Song, X.-T. Chen, J. L. Musfeldt, and Z.-L. Xue. CrystEngComm, **16**, 850 (2014).

[38] I. V. Chernyshova, M. F. Hochella Jr., and A. S. Madden. Phys. Chem. Chem. Phys., **9**, 1736 (2007).

[39] P. Chen, X. Xu, C. Koenigsmann, A. C. Santulli, S. S. Wong, and J. L. Musfeldt. Nano Lett., **10**, 4526 (2010).

[40] C. C. Yang and S. Li. J. Phys. Chem. B, **112**, 14193 (2008).

[41] X. W. Wang, G. T. Fei, K. Zheng, Z. Jin, and L. De Zhang. Appl. Phys. Lett., **88**, 23 (2006).

[42] S. H. Xu, G. T. Fei, Y. Zhang, X. F. Li, Z. Jin, and L. D. Zhang. Phys. Lett. A, **375**, 1746 (2011).

[43] C. P. Bean and J. D. Livingston. J. Appl. Phys., **30**, S120 (1959).

[44] U. Jeong, X. Teng, Y. Wang, H. Yang, and Y. Xia. Adv. Mater., **19**, 33 (2007).

[45] P. A. Quintero, D. Rajan, M. K. Peprah, T. V. Brinzari, R. S. Fishman, D. R. Talham, and M. W. Meisel. Phys. Rev. B, **91**, 014439 (2015).

[46] K. R. O'Neal, B. S. Holinsworth, Z. Chen, P. K. Peterson, K. E. Carreiro, C. Lee, J. L. Manson, M.-H. Whangbo, Z. Li, Z. Liu, and J. L. Musfeldt. Inorg. Chem., **55**, 12172 (2016).

[47] J. A. Wilson and A. D. Yoffe. Adv. Phys., **18**, 193 (1969).

[48] D. Jariwala, V. K. Sangwan, L. J. Lauhon, T. J. Marks, and M. C. Hersam. ACS Nano, **8**, 1102 (2014).

[49] M. F. Khan, M. W. Iqbal, M. Z. Iqbal, M. A. Shehzad, Y. Seo, and J. Eom. Appl. Mater. & Interfaces, **6**, 21645 (2014).

[50] M. Pumera, Z. Sofer, and A. Ambrosi. J. Mater. Chem. A, **2**, 8981 (2014).

[51] G. Xu, J. Wang, B. Yan, and X. L. Qi. Phys. Rev. B, **90**, 100505(R) (2014).

[52] D. Lembke, S. Bertolazzi, and A. Kis. Accounts Chem. Res., **48**, 100 (2015).

[53] Y. Q. Zhu, T. Sekine, K. S. Brigatti, S. Firth, R. Tenne, R. Rosentsveig, H. W. Kroto, and D. R. M. Walton. J. Am. Chem. Soc., **125**, 1329 (2003).

[54] R. Tenne, L. Margulis, M. Genut, and G. Hodes. Nature, **360**, 444 (1992).

[55] L. Rapoport, Y. Bilik, Y. Feldman, M. Homyonfer, S. R. Cohen, and R. Tenne. Nature, **387**, 791 (1997).

[56] L. Rapoport, N. Fleischer, and R. Tenne. Adv. Mater., **15**, 651 (2003).

[57] Active Protection NANO materials. Lubricants. http://www.apnano.com/product/lubricant/ (accessed March 25, 2015).

[58] Nanotech Industrial Solutions. Products. http://nisusacorp.com/product/ (accessed March 25, 2015).

[59] L. Rapoport, N. Fleischer, and R. Tenne. J. Mater. Chem., **15**, 1782 (2005).

[60] A. R. Adini, M. Redlich, and R. Tenne. J. Mater. Chem., **21**, 15121 (2011).

[61] L. Joly-Pottuz, F. Dassenoy, M. Belin, B. Vacher, J. M. Martin, and N. Fleischer. Tribol. Lett., **18**, 477 (2005).

[62] H. E. Unalan, Y. Yang, Y. Zhang, P. Hiralal, D. Kuo, S. Dalal, T. Butler, S. N. Cha, J. E. Jang, K. Chremmou, G. Lentaris, D. Wei, R. Rosentsveig, K. Suzuki, H. Matsumoto, M. Minagawa, Y. Hayashi, M. Chhowalla, A. Tanioka, W. I. Milne, R. Tenne, and G. A. J. Amaratunga. IEEE Trans. Electron. Devices, **55**, 2988 (2008).

[63] Q. C. Sun, X. S. Xu, L. I. Vergara, R. Rosentsveig, and J. L. Musfeldt. Phys. Rev. B, **79**, 205405 (2009).

[64] B. Radisavljevic, A. Radenovic, J. Brivio, V. Giacometti, and A. Kis. Nat. Nanotechnol., **6**, 147 (2011).

[65] R. Levi, O. Bitton, G. Leitus, R. Tenne, and E. Joselevich. Nano Lett., **13**, 3736 (2013).

[66] R. Kreizman, O. Schwartz, Z. Deutsch, S. Itzhakov, A. Zak, S. R. Cohen, R. Tenne, and D. Oron. Phys. Chem. Chem. Phys., **14**, 4271 (2012).

[67] J. T. Ye, Y. J. Zhang, R. Akashi, M. S. Bahramy, R. Arita, and Y. Iwasa. Science, **338**, 1193 (2012).

[68] C. Zhang, S. Wang, L. Yang, Y. Liu, T. Xu, Z. Ning, A. Zak, Z. Zhang, R. Tenne, and Q. Chem. Appl. Phys. Lett., **100**, 243101 (2012).

[69] Q. Sun, L. Yadgarov, R. Rosentsveig, G. Seifert, R. Tenne, and J. L. Musfeldt. ACS Nano, **7**, 3506 (2013).

[70] Q. Sun, D. Mazumdar, L. Yadgarov, R. Rosentsveig, R. Tenne, and J. L. Musfeldt. Nano Lett., **13**, 2803 (2013).

[71] A. Bruno, C. Borriello, S. A. Haque, C. Minarini, and T. D. Luccio. Phys. Chem. Chem. Phys., **16**, 17998 (2014).

[72] T. Lorenz, M. Ghorbani-Asl, J.-O. Joswig, T. Heine, and G. Seifert. Nanotechnology, **25**, 445201 (2014).

[73] A. Steinhoff, J. H. Kim, F. Jahnke, M. Rösner, D. S. Kim, C. Lee, G. H. Han, M. S. Jeong, T. O. Wehling, and C. Gies. Nano Lett., **15**, 6841 (2015).

[74] K. D. Finkelstein, Q. Shen, and S. Shastri. Phys. Rev. Lett., **69**, 1612 (1992).

[75] X. G. Wang, W. Weiss, S. K. Shaikhutdinov, M. Ritter, M. Petersen, F. Wagner, R. Schlögl, and M. Scheffler. Phys. Rev. Lett., **81**, 1038 (1998).

[76] J. Chen, L. Xu, W. Li, and X. Gou. Adv. Mater., **17**, 582 (2005).

[77] J. Lian, X. Duan, J. Ma, P. Peng, T. Kim, and W. Zheng. ACS Nano, **3**, 3749 (2009).

[78] L. A. Marusak, R. Messier, and W. B. White. J. Phys. Chem. Solids, **41**, 981 (1980).

[79] P. Chen, O. Günaydın-Şen, W. J. Ren, Z. Qin, T. V. Brinzari, S. McGill, S.-W. Cheong, and J. L. Musfeldt. Phys. Rev. B, **86**, 014407 (2012).

[80] T. Kawamura, S. Endo, M. Kobayashi, and S. Narita. J. Phys. Soc. Japan, **53**, 3684 (1984).

[81] K. Iishi. Phys. Chem. Miner., **3**, 1 (1978).

[82] S. H. Lapidus, J. L. Manson, H. Park, A. J. Clement, S. Ghannadzadeh, P. Goddard, T. Lancaster, J. S. Möller, S. J. Blundell, M. T. F. Telling, J. Kang, M.-H. Whangbo, and J. A. Schlueter. Chem. Commun., **49**, 499 (2013).

[83] Schlueter, J. A. *et al.* Unpublished work.

[84] D. L. Huber. Small, **1**, 482 (2005).

[85] D. S. Mathew and R.-S. Juang. Chem. Eng. J., **129**, 51 (2007).

[86] A. S. Teja and P.-Y. Koh. Prog. Cryst. Growth Charact. Mater., **55**, 22 (2009).

[87] S. Laurent, D. Forge, M. Port, A. Roch, C. Robic, L. Vander Elst, and R. N. Muller. Chem. Rev., **108**, 2064 (2008).

[88] R. Lopez, L. C. Feldman, and R. F. Haglund. Phys. Rev. Lett., **93**, 20 (2004).

[89] B. Piccione, R. Agarwal, Y. Jung, and R. Agarwal. Philos. Mag., **93**, 2089 (2013).

[90] B. Potter and J. Simmons. Phys. Rev. B, **37**, 10838 (1988).

[91] S. K. Sahoo, S. Pal, P. Sarkar, and C. Majumder. Chem. Phys. Lett., **516**, 68 (2011).

[92] B. Xu and B. C. Pan. Phys. Rev. B, **74**, 2 (2006).

[93] E. Zahedi. Superlattices Microstruct., **50**, 491 (2011).

[94] S. Sarkar and K. Chattopadhyay. Physica E, **44**, 1742 (2012).

[95] C. Yang and S. Li. Key Eng. Mater., **444**, 133 (2010).

[96] M. Li and J. C. Li. Mater. Lett., **60**, 2526 (2006).

[97] R. Kodama. J. Magn. Magn. Mater., **200**, 359 (1999).

[98] A.-H. Lu, E. L. Salabas, and F. Schüth. Angew. Chemie Int. Ed., **46**, 1222 (2007).

[99] T.-J. Park, G. C. Papaefthymiou, A. J. Viescas, A. R. Moodenbaugh, and S. S. Wong. Nano Lett., **7**, 766 (2007).

[100] R. D. Zysler, D. Fiorani, A. M. Testa, L. Suber, E. Agostinelli, and M. Godinho. Phys. Rev. B, **68**, 212408 (2003).

[101] O. Yalçin, H. Bayrakdar, and S. Özüm. J. Magn. Magn. Mater., **343**, 157 (2013).

[102] C. Ma, J.-Q. Yan, K. W. Dennis, R. W. McCallum, and X. Tan. J. Appl. Phys., **105**, 033908 (2009).

[103] H.-M. Cheng, K.-F. Lin, H.-C. Hsu, C.-J. Lin, and L.-J. Lin. J. Phys. Chem. B, **109**, 18385 (2005).

[104] H. L. Liu, M. X. Kuo, J. L. Her, K. S. Lu, S. M. Weng, L. M. Wang, S. L. Cheng, and J. G. Lin. J. Appl. Phys., **97**, 113528 (2005).

[105] M. J. Seong, O. I. Miććić, A. J. Nozik, A. Mascarenhas, H. M. Cheong, O. I. Mićić, A. J. Nozik, A. Mascarenhas, and H. M. Cheong. Appl. Phys. Lett., **82**, 185 (2003).

[106] I. H. Campbell and P. M. Fauchet. Solid State Commun., **58**, 739 (1986).

[107] J. E. Spanier, R. D. Robinson, F. Zhang, S.-W. Chan, and I. P. Herman. Phys. Rev. B, **64**, 245407 (2001).

[108] P. Verma, L. Gupta, S. C. Abbi, K. P. Jain, and I. Introduction. J. Appl. Phys., **88**, 4109 (2000).

[109] J. L. Rendon and C. J. Serna. Clay Miner., **16**, 375 (1981).

[110] L. Wang, W. Yang, Y. Ding, Y. Ren, S. Xiao, B. Liu, S. V. Sinogeikin, Y. Meng, D. J. Gosztola, G. Shen, R. J. Hemley, W. L. Mao, and H. K. Mao. Phys. Rev. Lett., **105**, 1 (2010).

[111] S.-W. Park, J.-T. Jang, J. Cheon, H.-H. Lee, D. R. Lee, and Y. Lee. J. Phys. Chem. C, **112**, 9627 (2008).

[112] B. Wei, K. Zheng, Y. Ji, Y. Zhang, Z. Zhang, and X. Han. Nano Lett., **12**, 4595 (2012).

[113] X. Dou, K. Ding, D. Jiang, X. Fan, and B. Sun. ACS Nano, **10**, 1619 (2016).

[114] Q. C. Sun, X. Xu, S. N. Baker, A. D. Christianson, and J. L. Musfeldt. Chem. Mater., **23**, 2956 (2011).

[115] Q. C. Sun, S. N. Baker, A. D. Christianson, and J. L. Musfeldt. Phys. Rev. B, **84**, 014301 (2011).

[116] Q. C. Sun, C. S. Birkel, J. Cao, W. Tremel, and J. L. Musfeldt. ACS Nano, **6**, 4876 (2012).

[117] Q. Zhang, X. Liu, M. I. B. Utama, J. Zhang, M. de la Mata, J. Arbiol, Y. Lu, T. C. Sum, and Q. Xiong. Nano Lett., **12**, 6420 (2012).

[118] P. H. de Oliveira Neto, J. F. Teixeira, R. Gargano, and G. M. e Silva. J. Phys. Chem. Lett., **3**, 3039 (2012).

[119] A. M. Kelley. ACS Nano, **5**, 5254 (2011).

[120] J. Gao, H. Gu, and B. Xu. Accounts Chem. Res., **42**, 1097 (2009).

[121] S. Mornet, S. Vasseur, F. Grasset, and E. Duguet. J. Mater. Chem., **14**, 2161 (2004).

[122] Q. A. Pankhurst, J. Connolly, S. K. Jones, and J. Dobson. J. Phys. D Appl. Phys., **36**, R167 (2003).

[123] L. H. Reddy, J. L. Arias, J. Nicolas, and P. Couvreur. Chem. Rev., **112**, 5818 (2012).

[124] C. Sun, J. S. H. Lee, and M. Zhang. Adv. Drug Deliv. Rev., **60**, 1252 (2008).

[125] M. B. Gawande, P. S. Branco, and R. S. Varma. Chem. Soc. Rev., **42**, 3371 (2013).

[126] R. B. Nasir Baig and R. S. Varma. Chem. Commun., **49**, 752 (2013).

[127] S. Shylesh, V. Schünemann, and W. R. Thiel. Angew. Chemie Int. Ed., **49**, 3428 (2010).

[128] X. Zhou, W. Xu, G. Liu, D. Panda, and P. Chen. J. Am. Chem. Soc., **132**, 138 (2010).

[129] N. A. Frey, S. Peng, K. Cheng, and S. Sun. Chem. Soc. Rev., **38**, 2532 (2009).

[130] J. H. Jung, J. H. Lee, and S. Shinkai. Chem. Soc. Rev., **40**, 4464 (2011).

[131] X. Yan, Y. Song, C. Zhu, J. Song, D. Du, X. Su, and Y. Lin. ACS Appl. Mater. Interfaces, **8**, 21990 (2016).

[132] D. R. Absolom, W. Zingg, and A. W. Neumann. J. Biomed. Mater. Res., **21**, 161 (1987).

[133] T. A. Haas and E. F. Plow. Curr. Opinons Cell. Biol., **6**, 656 (1994).

[134] N. Lewinski, V. Colvin, and R. Drezek. Small, **4**, 26 (2008).

[135] G. Liu, J. Gao, H. Ai, and X. Chen. Small, **9**, 1533 (2013).

[136] J. Yang, S. Wang, R. Dong, L. Zhang, Z. Zhu, and X. Gao. Mater. Lett., **184**, 9 (2016).

[137] S. Kellnberger, A. Rosenthal, A. Myklatun, G. G. Westmeyer, G. Sergiadis, and V. Ntziachristos. Phys. Rev. Lett., **116**, 108103 (2016).

[138] C. Wang, J. Meyer, N. Teichert, A. Auge, E. Rausch, B. Balke, A. Hütten, G. H. Fecher, and C. Felser. J. Vac. Sci. Technol. B, **32**, 020802 (2014).

[139] S. Hihath, R. A. Kiehl, and K. van Benthem. J. Appl. Phys., **116**, 084306 (2014).

[140] H. Wang, H. Wang, T. Li, J. Ma, K. Li, and X. Zuo. Sensors Actuators B Chem., **239**, 1205 (2017).

[141] H. Zhang, L. Yu, Q. Li, Y. Du, and S. Ruan. Sensors Actuators B Chem., **241**, 109 (2017).

[142] A. Campion and P. Kambhampati. Chem. Soc. Rev., **27**, 241 (1998).

[143] X.-M. Qian and S. M. Nie. Chem. Soc. Rev., **37**, 912 (2008).

[144] Z.-Q. Tian, B. Ren, and D.-Y. Wu. J. Phys. Chemsitry, **106**, 9463 (2002).

[145] G. V. Chalapathi, M. Thaidun, D. Subramanyam, B. S. Rao, C. Balanarayana, and B. R. Kumar. Chalcogenide Lett., **12**, 181 (2015).

[146] P. Kaur, S. Kumar, A. Singh, C. Chen, C. Dong, T. Chan, K. Lee, C. Srivastava, S. Rao, and M. Wu. Superlattices Microstruct., **83**, 785 (2015).

[147] L. Pauling and S. B. Hendricks. J. Am. Ceram. Soc., **47**, 781 (1925).

[148] F. J. Morin. Phys. Rev., **78**, 819 (1950).

[149] S. Foner and Y. Shapira. Phys. Lett., **29A**, 276 (1969).

[150] I. Dzyaloshinsky. J. Phys. Chem. Solids, **4**, 241 (1958).

[151] T. Moriya. J. Appl. Phys., **39**, 1042 (1968).

[152] M. J. Massey, U. Baier, R. Merlin, and W. H. Weber. Phys. Rev. B, **41**, 7822 (1990).

[153] S.-H. Shim and T. S. Duffy. Am. Mineral., **87**, 318 (2001).

[154] Y. P. He, Y. M. Miao, C. R. Li, S. Q. Wang, L. Cao, S. S. Xie, G. Z. Yang, B. S. Zou, and C. Burda. Phys. Rev. B, **71**, 1 (2005).

[155] H. Liu, A. Caldwell, L. R. Benedetti, W. Panero, and R. Jeanloz. Phys. Chem. Miner., **30**, 582 (2003).

[156] S. Ono, T. Kikegawa, and Y. Ohishi. J. Phys. Chem. Solids, **65**, 1527 (2004).

[157] P. Schouwink, L. Dubrovinsky, K. Glazyrin, M. Merlini, M. Hanfland, T. Pippinger, and R. Miletich. Am. Mineral., **96**, 1781 (2011).

[158] J. Kuneš, D. M. Korotin, M. A. Korotin, V. I. Anisimov, and P. Werner. Phys. Rev. Lett., **102**, 1 (2009).

[159] P. Chen, N. Lee, S. McGill, S.-W. Cheong, and J. L. Musfeldt. Phys. Rev. B, **85**, 174413 (2012).

[160] D. D. Sell, R. L. Greene, and R. M. White. Phys. Rev., **158**, 489 (1967).

[161] L. L. Lohr Jr. Coord. Chem. Rev., **8**, 241 (1972).

[162] A. I. Galuza, A. B. Beznosov, and V. V. Eremenko. Low Temp. Phys., **24**, 726 (1998).

[163] D. C. Herbert. Phys. Rev. Lett., **22**, 1184 (1969).

[164] E. J. Samuelsen and G. Shirane. Phys. Status Solidi, **42**, 241 (1970).

[165] H. M. Lu and X. K. Meng. J. Phys. Chem. C, **114**, 21291 (2010).

[166] S.-H. Gee, Y.-K. Hong, J. C. Sur, D. W. Erickson, M. H. Park, and F. Jeffers. IEEE Trans. Magn., **40**, 2691 (2004).

[167] S. Hayashi and H. Kanamori. J. Phys. C Solid State, **13**, 1529 (1980).

[168] F. J. Owens and J. Orosz. Solid State Commun., **138**, 95 (2006).

[169] S. P. R. Ramesh, S. Sohila, C. Muthamizhchelvan, M. Rajalakshmi, S. Ramya. J. Mater. Sci. Mater. Electron., **22**, 1357 (2011).

[170] L. Lu, L. Li, X. Wang, and G. Li. J. Phys. Chem. B, **109**, 17151 (2005).

[171] N. Amin and S. Arajs. Phys. Rev. B, **35**, 4810 (1987).

[172] C. Diaz-Guerra, L. Perez, J. Piqueras, and M. F. Chioncel. J. Appl. Phys., **106**, 104302 (2009).

[173] Q. Liu, V. Barrón, J. Torrent, H. Qin, and Y. Yu. Phys. Earth Planet. Inter., **183**, 387 (2010).

[174] S. Mitra, S. Das, S. Basu, P. Sahu, and K. Mandal. J. Magn. Magn. Mater., **321**, 2925 (2009).

[175] J. M. Pastor, J. I. Pérez-Landazábal, C. Gómez-Polo, V. Recarte, S. Larumbe, R. Santamarta, M. Fernandes Silva, E. A. Gómez Pineda, A. A. Winkler Hechenleitner, and M. K. Lima. Appl. Phys. Lett., **100**, 1 (2012).

[176] T. P. Raming, A. J. S. Winnubst, C. M. van Kats, and A. P. Philipse. J. Colloid Interface Sci., **249**, 346 (2002).

[177] L. Suber, P. Imperatori, A. Mari, G. Marchegiani, M. V. Mansilla, D. Fiorani, W. R. Plunkett, D. Rinaldi, C. Cannas, G. Ennas, and D. Peddis. Phys. Chem. Chem. Phys., **12**, 6984 (2010).

[178] S.-B. Wang, Y.-L. Min, and S.-H. Yu. J. Phys. Chem. C, **111**, 3551 (2007).

[179] Y. Zhao, C. W. Dunnill, Y. Zhu, D. H. Gregory, W. Kockenberger, Y. Li, W. Hu, I. Ahmad, and D. G. McCartney. Chem. Mater., **19**, 916 (2007).

[180] L. Suber, A. G. Santiago, D. Fiorani, P. Imperatori, A. M. Testa, M. Angiolini, A. Montone, and J. L. Dormann. Appl. Organomet. Chem., **12**, 347 (1998).

[181] L. Suber, D. Fiorani, P. Imperatori, S. Foglia, A. Montone, and R. Zysler. ACS Sym. Ser., **11**, 797 (1999).

[182] J. C. Wildervanck and F. Jellinek. Z. Anorg. Allg. Chem., **328**, 309 (1964).

[183] W. Schutte, J. De Boer, and F. Jellinek. J. Solid State Chem., **70**, 207 (1987).

[184] E. Selvi, Y. Ma, R. Aksoy, A. Ertas, and A. White. J. Phys. Chem. Solids, **67**, 2183 (2006).

[185] J. Baglio, E. Kamieniecki, N. DeCola, C. Struck, J. Marzik, K. Dwight, and A. Wold. J. Solid State Chem., **49**, 166 (1983).

[186] P. C. Yen, Y. S. Huang, and K. K. Tiong. J. Phys. Condens. Matter, **16**, 2171 (2004).

[187] K. K. Kam and B. A. Parkinson. J. Phys., **86**, 463 (1982).

[188] A. Kuc, N. Zibouche, and T. Heine. Phys. Rev. B, **83**, 245213 (2011).

[189] T. Sekine, T. Nakashizu, K. Toyoda, K. Uchinokura, and E. Matsuura. Solid State Commun., **35**, 371 (1980).

[190] R. D. Luttrell, S. Brown, J. Cao, J. L. Musfeldt, R. Rosentsveig, and R. Tenne. Phys. Rev. B, **73**, 1 (2006).

[191] J. Zhang, Z. Y. Wu, K. Ibrahim, M. I. Abbas, and X. Ju. Nucl. Instrum. Meth. B, **199**, 291 (2003).

[192] C. S. Reddy, A. Zak, and E. Zussman. J. Mater. Chem., **21**, 16086 (2011).

[193] M. Shneider, L. Rapoport, A. Moshkovich, H. Dodiuk, S. Kenig, R. Tenne, and A. Zak. Phys. Status Solidi A, **210**, 2298 (2013).

[194] M. Naffakh and A. Díez-Pascual. Inorganics, **2**, 291 (2014).

[195] M. Stefanov, A. N. Enyashin, T. Heine, and G. Seifert. J. Phys. Chem. C, **112**, 17764 (2008).

[196] J. Cook, S. Rhyans, L. Roncase, G. Hobson, and C. Luhrs. Inorganics, **2**, 377 (2014).

[197] S. Brown, J. Cao, J. L. Musfeldt, M. M. Conner, A. C. McConnell, H. I. Southerland, J. L. Manson, J. A. Schlueter, M. D. Phillips, M. M. Turnbull, and C. P. Landee. Inorg. Chem., **46**, 8577 (2007).

[198] G. Seifert, H. Terrones, M. Terrones, and T. Frauenheim. Solid State Commun., **115**, 635 (2000).

[199] A. P. Nayak, T. Pandey, D. Voiry, J. Liu, S. T. Moran, A. Sharma, C. Tan, C.-H. Chen, L.-J. Li, M. Chhowalla, J.-F. Lin, A. K. Singh, and D. Akinwande. Nano Lett., **15**, 346 (2015).

[200] X. Fan, C.-H. Chang, W. T. Zheng, J.-L. Kuo, and D. J. Singh. J. Phys. Chem. C, **119**, 10189 (2015).

[201] N. Bandaru, R. S. Kumar, D. Sneed, O. Tschauner, J. Baker, D. Antonio, S.-N. Luo, T. Hartmann, Y. Zhao, and R. Venkat. J. Phys. Chem. C, **118**, 3230 (2014).

[202] J. S. Miller and A. J. Epstein. Angew. Chemie Int. Ed., **33**, 385 (1994).

[203] B. Pilawa. Ann. Phys., **8**, 191 (1999).

[204] P. A. Goddard, J. Singleton, P. Sengupta, R. D. McDonald, T. Lancaster, S. J. Blundell, F. L. Pratt, S. Cox, N. Harrison, J. L. Manson, H. I. Southerland, and J. A. Schlueter. New J. Phys., **10**, 083205 (2008).

[205] C. V. Topping. Angew. Chemie Int. Ed., **49**, 5228 (2010).

[206] J. S. Miller. Chem. Soc. Rev., **40**, 3266 (2011).

[207] J. S. Miller and M. Drillon. *Magnetism: Molecules to materials*, vol. 3. Wileey-VCH Verlag GmbH & Co. KGaA (2002).

[208] E. Coronado and P. Day. Chem. Rev., **104**, 5419 (2004).

[209] J. Mroziński. Coord. Chem. Rev., **249**, 2534 (2005).

[210] P. A. Goddard, J. L. Manson, J. Singleton, I. Franke, T. Lancaster, A. J. Steele, S. J. Blundell, C. Baines, F. L. Pratt, R. D. McDonald, O. E. Ayala-Valenzuela, J. F. Corbey, H. I. Southerland, P. Sengupta, and J. A. Schlueter. Phys. Rev. Lett., **108**, 1 (2012).

[211] J. S. Miller and J. L. Manson. Accounts Chem. Res., **34**, 563 (2001).

[212] T. Lancaster, P. A. Goddard, S. J. Blundell, F. R. Foronda, S. Ghannadzadeh, J. S. Möller, P. J. Baker, F. L. Pratt, C. Baines, L. Huang, J. Wosnitza, R. D. McDonald, K. A. Modic, J. Singleton, C. V. Topping, T. A. W. Beale, F. Xiao, J. A. Schlueter, A. M. Barton, R. D. Cabrera, K. E. Carreiro, H. E. Tran, and J. L. Manson. Phys. Rev. Lett., **112**, 207201 (2014).

[213] P. R. Hammar, M. B. Stone, D. H. Reich, C. Broholm, P. J. Gibson, M. M. Turnbull, C. P. Landee, and M. Oshikawa. Phys. Rev. B, **59**, 1008 (1999).

[214] C. S. Olson, C. L. Heth, F. L. Alema, S. H. Lapidus, P. W. Stephens, and K. I. Pokhodnya. J. Phys. Condens. Matter, **25**, 256004 (2013).

[215] J. L. Manson, S. H. Lapidus, P. W. Stephens, P. K. Peterson, K. E. Carreiro, H. I. Southerland, T. Lancaster, S. J. Blundell, A. J. Steele, P. A. Goddard, F. L. Pratt, J. Singleton, Y. Kohama, R. D. McDonald, R. E. Del Sesto, N. A. Smith, J. Bendix, S. A. Zvyagin, J. Kang, C. Lee, M.-H. Whangbo, V. S. Zapf, and A. Plonczak. Inorg. Chem., **50**, 5990 (2011).

[216] M. Kajňaková, M. Orendáč, A. Orendáčová, A. Vlček, J. Černák, O. V. Kravchyna, A. G. Anders, M. Bałanda, J. H. Park, A. Feher, and M. W. Meisel. Phys. Rev. B, **71**, 014435 (2005).

[217] C. Wynn, M. Gîrţu, J. Miller, and A. Epstein. Phys. Rev. B, **56**, 14050 (1997).

[218] Y. Numata, K. Inoue, N. Baranov, M. Kurmoo, and K. Kikuchi. J. Am. Chem. Soc., **129**, 9902 (2007).

[219] N. A. Fortune, S. T. Hannahs, Y. Yoshida, T. E. Sherline, T. Ono, H. Tanaka, and Y. Takano. Phys. Rev. Lett., **102**, 257201 (2009).

[220] J. L. Musfeldt, L. I. Vergara, T. V. Brinzari, C. Lee, L. C. Tung, J. Kang, Y. J. Wang, J. A. Schlueter, J. L. Manson, and M. H. Whangbo. Phys. Rev. Lett., **103**, 157401 (2009).

[221] E. Coronado, M. C. Giménez-López, T. Korzeniak, G. Levchenko, F. M. Romero, A. Segura, V. García-Baonza, J. C. Cezar, F. M. F. de Groot, A. Milner, and M. Paz-Pasternak. J. Am. Chem. Soc., **130**, 15519 (2008).

[222] J. G. Dasilva and J. S. Miller. Inorg. Chem., **52**, 1418 (2013).

[223] J. L. Musfeldt, Z. Liu, S. Li, J. Kang, C. Lee, O. Jena, J. L. Manson, J. A. Schlueter, G. L. Carr, and M.-H. Whangbo. Inorg. Chem., **50**, 6347 (2011).

[224] A. A. Yakovenko, K. W. Chapman, and G. J. Halder. Acta Crystallogr. B, **71**, 252 (2015).

[225] S. Ghannadzadeh, J. S. Möller, P. A. Goddard, T. Lancaster, F. Xiao, S. J. Blundell, A. Maisuradze, R. Khasanov, J. L. Manson, S. W. Tozer, D. Graf, and J. A. Schlueter. Phys. Rev. B, **87**, 241102(R) (2013).

[226] K. R. O'Neal, J. G. Cherian, A. Zak, R. Tenne, Z. Liu, and J. L. Musfeldt. Nano Lett., **16**, 993 (2016).

[227] T. V. Brinzari, K. R. O'Neal, J. L. Manson, J. A. Schlueter, A. P. Litvinchuk, Z. Liu, and J. L. Musfeldt. Inorg. Chem., **55**, 1956 (2016).

[228] al-Wahish, A.; O'Neal, K. R.; Lee, C.; Fan, S.; Hughey, K.; Yokosuk, M. O.; Clune, A.; Li, Z.; Manson, J. L.; Whangbo, M.-H.; Musfeldt, J. L. Submitted to *Phys. Rev. Lett.*

[229] J. L. Manson, C. R. Kmety, A. J. Epstein, and J. S. Miller. Inorg. Chem., **38**, 2552 (1999).

[230] C. J. Nuttall, T. Takenobu, Y. Iwasa, and M. Kurmoo. Mol. Cryst. Liq. Cryst., **343**, 227 (2000).

[231] T. Jestädt, M. Kurmoo, S. J. Blundell, F. L. Pratt, C. J. Kepert, K. Prassides, B. W. Lovett, I. M. Marshall, A. Husmann, K. H. Chow, R. M. Valladares, C. M. Brown, and A. Lappas. J. Phys. Condens. Matter, **13**, 2263 (2001).

[232] S. R. Batten and K. S. Murray. Coord. Chem. Rev., **246**, 103 (2003).

[233] A. Lappas, A. S. Wills, M. A. Green, K. Prassides, and M. Kurmoo. Phys. Rev. B, **67**, 144406 (2003).

[234] D. O. Demchenko, A. Y. Liu, E. Z. Kurmaev, L. D. Finkelstein, V. R. Galakhov, A. Moewes, S. G. Chiuzbăian, M. Neumann, C. R. Kmety, and K. L. Stevenson. Phys. Rev. B, **69**, 205105 (2004).

[235] T. V. Brinzari, J. T. Haraldsen, P. Chen, Q.-C. Sun, Y. Kim, L.-C. Tung, A. P. Litvinchuk, J. A. Schlueter, D. Smirnov, J. L. Manson, J. Singleton, and J. L. Musfeldt. Phys. Rev. Lett., **111**, 047202 (2013).

[236] J. L. Musfeldt, T. V. Brinzari, J. A. Schlueter, J. L. Manson, A. P. Litvinchuk, and Z. Liu. Inorg. Chem., **52**, 14148 (2013).

[237] J. L. Musfeldt, K. R. O'Neal, T. V. Brinzari, P. Chen, J. A. Schlueter, J. L. Manson, A. P Litvinchuk, and Z. Liu. In preparation.

[238] S. R. Batten, P. Jensen, B. Moubaraki, K. S. Murray, and R. Robson. Chem. Commun., 439–440 (1998).

[239] M. Kurmoo and C. J. Kepert. New J. Chem., 1515–1524 (1998).

[240] C. R. Kmety, Q. Huang, J. W. Lynn, R. W. Erwin, J. L. Manson, S. McCall, J. E. Crow, K. L. Stevenson, J. S. Miller, and A. J. Epstein. Phys. Rev. B, **62**, 5576 (2000).

[241] J. L. Manson, C. R. Kmety, F. Palacio, A. J. Epstein, and J. S. Miller. Chem. Mater., **13**, 1068 (2001).

[242] S. Hirai and W. L. Mao. Appl. Phys. Lett., **102**, 041912 (2013).

[243] S. Li, K. Wang, M. Zhou, Q. Li, B. Liu, G. Zou, and B. Zou. J. Phys. Chem. B, **115**, 8981 (2011).

[244] M. Mączka, T. A. Da Silva, W. Paraguassu, M. Ptak, and K. Hermanowicz. Inorg. Chem., **53**, 12650 (2014).

[245] A. Prescimone, C. Morien, D. Allan, J. A. Schlueter, S. W. Tozer, J. L. Manson, S. Parsons, E. K. Brechin, and S. Hill. Angew. Chemie Int. Ed., **51**, 7490 (2012).

[246] G. J. Halder, K. W. Chapman, J. A. Schlueter, and J. L. Manson. Angew. Chemie Int. Ed., **50**, 419 (2011).

[247] F. Aguado, F. Rodriguez, and P. Núñez. Phys. Rev. B, **76**, 094417 (2007).

[248] L. W. Finger and R. M. Hazen. J. Appl. Phys., **51**, 5362 (1980).

[249] Z. Dong, N. M. Seemann, N. Lu, and Y. Song. J. Phys. Chem. B, **115**, 14912 (2011).

[250] A. Liu and Y. Song. J. Phys. Chem. C, **116**, 2123 (2012).

[251] C. Slebodnick, J. Zhao, R. Angel, B. E. Hanson, Y. Song, Z. Liu, and R. J. Hemley. Inorg. Chem., **43**, 5245 (2004).

[252] A. Torabi, Y. Song, and V. N. Staroverov. J. Phys. Chem. C, **117**, 2210 (2013).

[253] K. K. Zhuravlev, K. Traikov, Z. Dong, S. Xie, Y. Song, and Z. Liu. Phys. Rev. B, **82**, 064116 (2010).

[254] E. D. Emmons, R. G. Kraus, S. S. Duvvuri, J. S. Thompson, and A. M. Covington. J. Polym. Sci. Pol. Phys., **45**, 358 (2007).

[255] T. Ravindran, A. Arora, and T. Mary. Phys. Rev. Lett., **84**, 3879 (2000).

[256] W.-P. Hsieh, P. Zalden, M. Wuttig, A. M. Lindenberg, and W. L. Mao. Appl. Phys. Lett., **103**, 191908 (2013).

[257] R. Zallen. Phys. Rev. B, **9**, 4485 (1974).

[258] D. Shakhvorostov, R. A. Nistor, L. Krusin-Elbaum, G. J. Martyna, D. M. Newns, B. G. Elmegreen, X.-H. Liu, Z. E. Hughes, S. Paul, C. Cabral, S. Raoux, D. B. Shrekenhamer, D. N. Basov, Y. Song, and M. H. Mu. Proc. Natl. Acad. Sci., **106**, 10907 (2009).

[259] C. Marini, M. Valentini, A. Perucchi, P. Dore, D. D. Sarma, S. Lupi, and P. Postorino. High Press. Res., **31**, 18 (2011).

[260] A. P. Nayak, S. Bhattacharyya, J. Zhu, J. Liu, X. Wu, T. Pandey, C. Jin, A. K. Singh, D. Akinwande, and J.-F. Lin. Nat. Commun., **5**, 3731 (2014).

[261] Z. Zhao, H. Zhang, H. Yuan, S. Wang, Y. Lin, Q. Zeng, G. Xu, Z. Liu, G. K. Solanki, K. D. Patel, Y. Cui, H. Y. Hwang, and W. L. Mao. Nat. Commun., **6**, 7312 (2015).

[262] H. B. Cui, D. Graf, J. S. Brooks, and H. Kobayashi. Phys. Rev. Lett., **102**, 10 (2009).

[263] K. A. Johnson and N. W. Ashcroft. Nature, **403**, 632 (2000).

[264] J. H. Eggert, F. Moshary, W. J. Evans, H. E. Lorenzana, K. A. Goettel, I. F. Silvera, and W. C. Moss. Phys. Rev. Lett., **66**, 193 (1991).

[265] A. F. Goncharov, J. S. Tse, H. Wang, J. Yang, V. V. Struzhkin, R. T. Howie, and E. Gregoryanz. Phys. Rev. B, **87**, 024101 (2013).

[266] E. Wigner and H. B. Huntington. J. Chem. Phys., **3**, 764 (1935).

[267] M. I. Eremets and I. A. Troyan. Nat. Mater., **10**, 927 (2011).

[268] C.-S. Zha, Z. Liu, M. Ahart, R. Boehler, and R. J. Hemley. Phys. Rev. Lett., **110**, 217402 (2013).

[269] C.-S. Zha, Z. Liu, and R. J. Hemley. Phys. Rev. Lett., **108**, 146402 (2012).

[270] C. Narayana, H. Luo, J. Orloff, and A. L. Ruoff. Nature, **393**, 46 (1998).

[271] P. Loubeyre, F. Occelli, and R. LeToullec. Nature, **416**, 613 (2002).

[272] T. Kenichi. J. Appl. Phys., **89**, 662 (2001).

[273] Y. Shen, R. S. Kumar, M. Pravica, and M. F. Nicol. Rev. Sci. Instrum., **75**, 4450 (2004).

[274] S. D. Jacobsen, C. M. Holl, K. A. Adams, R. A. Fischer, E. S. Martin, C. R. Bina, J.-F. Lin, V. B. Prakapenka, A. Kubo, and P. Dera. Am. Mineral., **93**, 1823 (2008).

[275] A. Jayaraman, S. K. Sharma, S. Y. Wang, and S.-W. Cheong. Phys. Rev. B, **55**, 5694 (1997).

[276] L. C. Ming, T. Eto, K. Takeda, Y. Kobayashi, E. Suzuki, S. Endo, S. K. Sharma, A. Jayaraman, and T. Kikegawa. J. Phys. Condens. Matter, **14**, 10475 (2002).

[277] R. M. Hazen and L. W. Finger. J. Appl. Phys., **56**, 1838 (1984).

[278] D. Errandonea, Y. Meng, M. Somayazulu, and D. Häusermann. Physica B, **355**, 116 (2005).

[279] M. N. Ali, J. Xiong, S. Flynn, J. Tao, Q. D. Gibson, L. M. Schoop, T. Liang, N. Haldolaarachchige, M. Hirschberger, N. P. Ong, and R. J. Cava. Nature, **514**, 205 (2014).

[280] T. Liang, Q. Gibson, M. N. Ali, M. Liu, R. J. Cava, and N. P. Ong. Nat. Mater., **14**, 280 (2014).

[281] M. Mochizuki. Phys. Rev. B, **92**, 224412 (2015).

[282] A. Sozinov, A. A. Likhachev, N. Lanska, and K. Ullakko. Appl. Phys. Lett., **80**, 1746 (2002).

[283] K. Ullakko, J. K. Huang, C. Kantner, R. C. O'Handley, and V. V. Kokorin. Appl. Phys. Lett., **69**, 1966 (1996).

[284] N. A. Spaldin. *Magnetic materials: Fundamentals and applications.* Cambridge University Press, 2 ed. (2010).

[285] S. Blundell. *Magnetism in condensed matter.* OUP Oxford (2001).

[286] A. N. Bogdanov, A. V. Zhuravlev, and U. K. Rößler. Phys. Rev. B, **75**, 094425 (2007).

[287] T. V. Brinzari, P. Chen, L.-C. Tung, Y. Kim, D. Smirnov, J. Singleton, J. S. Miller, and J. L. Musfeldt. Phys. Rev. B, **86**, 214411 (2012).

[288] E. Granado, A. García, J. Sanjurjo, C. Rettori, I. Torriani, F. Prado, R. Sánchez, A. Caneiro, and S. Oseroff. Phys. Rev. B, **60**, 11879 (1999).

[289] K. R. O'Neal, T. V. Brinzari, J. B. Wright, C. Ma, S. Giri, J. A. Schlueter, Q. Wang, P. Jena, Z. Liu, and J. L. Musfeldt. Sci. Rep., **4**, 6054 (2014).

[290] M. de Souza, P. Foury-Leylekian, A. Moradpour, J.-P. Pouget, and M. Lang. Phys. Rev. Lett., **101**, 1 (2008).

[291] M. Bassi, P. Camagni, R. Rolli, G. Samoggia, F. Parmigiani, G. Dhalenne, and A. Revcolevschi. Phys. Rev. B, **54**, R11030 (1996).

[292] Q. C. Sun, H. Sims, D. Mazumdar, J. X. Ma, B. S. Holinsworth, K. R. O'Neal, G. Kim, W. H. Butler, A. Gupta, and J. L. Musfeldt. Phys. Rev. B, **86**, 1 (2012).

[293] P. Chen, B. S. Holinsworth, K. R. O'Neal, T. V. Brinzari, D. Mazumdar, Y. Q. Wang, S. McGill, R. J. Cava, B. Lorenz, and J. L. Musfeldt. Phys. Rev. B, **89**, 165120 (2014).

[294] M. O. Yokosuk, A. Al-Wahish, S. Artyukhin, K. R. O'Neal, D. Mazumdar, P. Chen, J. Yang, Y. S. Oh, S. A. Mcgill, K. Haule, S.-W. Cheong, D. Vanderbilt, and J. L. Musfeldt. Phys. Rev. Lett., **117**, 147402 (2016).

[295] A. V. Kimel, R. V. Pisarev, F. Bentivegna, and T. Rasing. Ferroelectrics, **279**, 135 (2002).

[296] J. H. Hodak, A. Henglein, and G. V. Hartland. J. Chem. Phys., **111**, 8613 (1999).

[297] H. K. Mao, P. M. Bell, J. W. Shaner, and D. J. Steinberg. J. Appl. Phys., **49**, 3276 (1978).

[298] G. L. Carr, M. C. Martin, W. R. McKinney, K. Jordan, G. R. Neil, and G. P. Williams. Nature, **420**, 153 (2002).

[299] A. Zak, L. Sallacan-Ecker, A. Margolin, Y. Feldman, R. Popovitz-Biro, A. Albu-Yaron, M. Genut, and R. Tenne. Fullerenes, Nanotub. Carbon Nanostructures, **19**, 18 (2011).

[300] Z. Pu, M. Cao, J. Yang, K. Huang, and C. Hu. Nanotechnology, **17**, 799 (2006).

[301] C.-J. Jia, L.-D. Sun, Z.-G. Yan, L.-P. You, F. Luo, X.-D. Han, Y.-C. Pang, Z. Zhang, and C.-H. Yan. Angew. Chemie Int. Ed., **44**, 4328 (2005).

[302] T. J. Park and S. S. Wong. Chem. Mater., **18**, 5289 (2006).

[303] K. R. O'Neal, J. M. Patete, P. Chen, B. S. Holinsworth, J. M. Smith, N. Lee, S.-W. Cheong, S. S. Wong, C. Marques, M. C. Aronson, and J. L. Musfeldt. J. Chem. Phys., **141**, 044710 (2014).

[304] C. Loschen, J. Carrasco, K. M. Neyman, and F. Illas. Phys. Rev. B, **75**, 035115 (2007).

[305] J. P. Perdew, K. Burke, and M. Ernzerhof. Phys. Rev. Lett., **77**, 3865 (1996).

[306] G. Kresse and J. Hafner. Phys. Rev. B, **47**, 558 (1993).

[307] G. Kresse and J. Furthmüller. Phys. Rev. B, **54**, 11169 (1996).

[308] S. L. Dudarev, S. Y. Savrasov, C. J. Humphreys, and A. P. Sutton. Phys. Rev. B, **57**, 1505 (1998).

[309] P. E. Blöchl. Phys. Rev. B, **50**, 17953 (1994).

[310] G. Kresse and D. Joubert. Phys. Rev. B, **59**, 1758 (1999).

[311] T. J. Wieting and J. L. Verble. Phys. Rev. B, **3**, 4286 (1971).

[312] A. Molina-Sánchez and L. Wirtz. Phys. Rev. B, **84**, 155413 (2011).

[313] M. Viršek, A. Jesih, I. Milošević, M. Damnjanović, and M. Remškar. Surf. Sci., **601**, 2868 (2007).

[314] M. Staiger, P. Rafailov, K. Gartsman, H. Telg, M. Krause, G. Radovsky, A. Zak, and C. Thomsen. Phys. Rev. B, **86**, 165423 (2012).

[315] R. Zallen, M. L. Slade, and A. T. Ward. Phys. Rev. B, **3**, 4257 (1971).

[316] T. J. Wieting and J. L. Verble. Phys. Rev. B, **5**, 1473 (1972).

[317] J. L. Verble, T. J. Weitling, and P. R. Reed. Solid State Commun., **11**, 941 (1972).

[318] The $E_{2g}$ and $E_{1u}$ modes are excellent examples of this behavior, and they track each other very well.

[319] S. Brown, J. L. Musfeldt, I. Mihut, J. B. Betts, A. Migliori, A. Zak, and R. Tenne. Nano Lett., **7**, 2365 (2007).

[320] At 20 GPa the $a$ and $c$ parameters for bulk $WS_2$ are decreased from their ambient values by 3% and 10%, respectively, [201] leading to a unit cell volume of $\approx 88$ Å$^3$.

[321] L. S. Panchakarla, G. Radovsky, L. Houben, R. Popovitz-Biro, R. E. Dunin-borkowski, and R. Tenne. J. Chem. Phys. Lett., **5**, 3724 (2014).

[322] Y. Q. Zhu, T. Sekine, Y. H. Li, W. X. Wang, M. W. Fay, H. Edwards, P. D. Brown, N. Fleischer, and R. Tenne. Adv. Mater., **17**, 1500 (2005).

[323] M. Ghorbani-Asl, N. Zibouche, M. Wahiduzzaman, A. F. Oliveira, A. Kuc, and T. Heine. Sci. Rep., **3**, 2961 (2013).

[324] Interestingly, the strong hardening of the $A_{1g}$ mode and its possible contribution to the breakdown mechanism also present ways to block the tube breakdown. One strategy might be to fill the nanotubes, for example with fullerenes, providing structural support and preventing the tube walls from distorting. Nanotubes could also be natively filled by an oxide core if the synthesis is not fully completed. [327] Another option is to adopt a nanoscroll geometry, [321] for which compression might result in a tighter scroll curling instead of an overall shape distortion.

[325] The synthesis starts from formation of oxide whiskers which, in the later steps of the reaction, convert to $WS_2$ nanotubes by sulfidization from the outside in, thus some oxide could easily be rested in the core.

[326] We point out that the uniqueness of the $A_{1g}$ mode may also explain nanotube cutting under intense ultrasonic treatment. [327,328] Presumably, the compression wave obtained from the collapse of a nearby droplet exerts force on the tube. As the most pressure sensitive displacement, the $A_{1g}$ mode again forms a pinching point. If the force is strong enough, the tube cleaves into different segments, with little damage. [327,328] Strong evidence for this connection is shown in Fig. 4.3 (b), where compression up to 20 GPa has driven a cleavage similar to that seen [327,328] under ultrasonic treatment.

[327] A. Zak, L. Sallacan Ecker, R. Efrati, L. Drangai, N. Fleischer, and R. Tenne. Sensors & Transducers, **12**, 1 (2011).

[328] E. Zohar, S. Baruch, M. Shneider, H. Dodiuk, S. Kenig, R. Tenne, and H. D. Wagner. J. Adhes. Sci. Technol., **25**, 1603 (2011).

[329] N. Zibouche, A. Kuc, J. Musfeldt, and T. Heine. Ann. Phys., **526**, 395 (2014).

[330] We note that for these measurements the presence of a pressure medium ensures that the applied pressure is quasi-static.

[331] T. C. Choy. *Effective medium theory: Principles and applications; International series of monographs on physics.* Clarendon Press (1999).

[332] We can easily rule out several other more common assignments. There is, for instance, no evidence that the localized absorption is due to band gap closure and metallization. Such a feature should shift from the visible through the near infrared into the middle infrared to the far infrared before heading toward zero frequency. We find no evidence for such an effect. The development of the far infrared localized absorption is instead quite different. It becomes more prominent under compression but does not change position. Simple ligand to metal (or metal to ligand) charge transfer excitations can be ruled out for similar reasons. A pressure-induced increase in the number of point defects can, however, be detected in the infrared response and should be expected to scale as the number of defects. In our experience, these spectral features are narrow and of low intensity, [333] not strong and broad as observed in the high pressure spectrum of the $WS_2$ nanotubes. We therefore eliminate this assignment from consideration.

[333] V. C. Long, J. L. Musfeldt, K. Kamarás, G. B. Adams, J. B. Page, Y. Iwasa, and W. E. Mayo. Phys. Rev. B, **61**, 13191 (2000).

[334] G. L. Carr, S. Perkowitz, and D. B. Tanner. Infrared Millim. Waves, **13**, 171 (1985).

[335] We employ a two-dimensional percolation model because the applied pressure essentially compresses the nanotubes into a thin film.

[336] H.-K. Jang, J. E. Jin, J. H. Choi, P.-S. Kang, D.-H. Kim, and G. T. Kim. Phys. Chem. Chem. Phys., **17**, 6874 (2015).

[337] These values differ slightly depending on the exact amount of nanotubes loaded into the diamond anvil cell.

[338] G. Seifert, H. Terrones, M. Terrones, G. Jungnickel, and T. Frauenheim. Phys. Rev. Lett., **85**, 146 (2000).

[339] N. Zibouche, A. Kuc, and T. Heine. Eur. Phys. J. B, **85**, 49 (2012).

[340] G. L. Frey, R. Tenne, M. J. Matthews, M. S. Dresselhaus, and G. Dresselhaus. J. Mater. Res., **13**, 2412 (1998).

[341] L. Scheffer, R. Rosentzveig, A. Margolin, R. Popovitz-Biro, G. Seifert, S. R. Cohen, and R. Tenne. Phys. Chem. Chem. Phys., **4**, 2095 (2002).

[342] C. J. Ballhausen. *Introduction to ligand field thoery.* McGraw-Hill, New York (1962).

[343] The $d - d$ excitation was fit with a Gaussian curve, the area of which was converted into oscillator strength as $f = \frac{2c}{N_e \pi \omega_\rho^2} \int_{\omega 1}^{\omega 2} n\alpha(\omega) d\omega$, [344] where $N_e = 5$ is the number of electrons per Fe site, $n \simeq 2.23$ is the refractive index, $\omega_\rho$ is the plasma frequency $\omega_\rho \equiv \sqrt{\frac{e^2 \rho}{m \epsilon_0}}$, $e$ and $m$ are the charge and mass of an electron, $\epsilon_0$ is the vacuum dielectric constant, $\rho$ is the density of Fe sites, $c$ is the speed of light, and $\omega_1$ and $\omega_2$ are the frequency limits of integration.

[344] F. Wooten. *Optical properties of solids.* Academic Press, New York-London (1972).

[345] T. Tsuboi, M. Chiba, and Y. Ajiro. Phys. Rev. B, **32**, 354 (1985).

[346] A. U. Gehring and A. M. Hofmeister. Clays Clay Miner., **42**, 409 (1994).

[347] L. L. Lohr Jr. J. Chem. Phys., **50**, 4596 (1969).

[348] The previously published data are inconsistent with our data in two main ways. The first relates to the spectrum itself. The authors note that their oscillator strength is an order of magnitude higher than previous reports. [349] The spectra of Marusak *et al.* also display shoulders on either side of the electronic feature, which probably arise from sample impurities. [78] The second difference relates to fitting the temperature dependent oscillator strength trend. The absence of data below 100 K results in large error bars in the value of $f_0$ which is critical for an accurate fit. The functional form used by the previous authors does not fit to the oscillator strengths that we obtained, so we elected to use the more common model described in the text.

[349] G. Lehmann and H. Harder. Am. Mineral., **55**, 98 (1970).

[350] By taking the experimental frequencies of these two phonons for each sample, we can determine the weighted contribution of each based on the value of $\nu$ determined from our fitting. Doing so reveals thatthe weight shifts towards the lower frequency mode with the reduction of size.

[351] It is well known that electronic transitions can influence phonon behavior, such as resonant Raman, Fano lineshapes, or the Huang-Rhys factor in photoluminescence [395–397]. A good example is electron-molecular vibrational coupling in charge transfer salts, where the temperature dependent vibronic coupling constant directly affects the phonon oscillator strength [398–400]. Other examples of phonon mixing with $d$- and $f$-manifold crystal field excitations manifest as avoided crossings [235, 401].

[352] R. L. Greene, D. D. Sell, W. M. Yen, and A. L. Schawlow. Phys. Rev. Lett., **15**, 656 (1965).

[353] X. S. Xu, T. V. Brinzari, S. Lee, Y. H. Chu, L. W. Martin, A. Kumar, S. McGill, R. C. Rai, R. Ramesh, V. Gopalan, S. W. Cheong, and J. L. Musfeldt. Phys. Rev. B, **79**, 134425 (2009).

[354] The field-induced spectral trends in the bulk powder and hematite nanoparticles are similar but smeared out compared to what is observed in single crystals. [159] This is due to the intrinsic random crystallite orientation and the distribution of particle sizes - particularly for the highly directional collective excitations.

[355] The single crystal data is taken from the average of the three polarizations reported previously in Ref. 159.

[356] R. M. White and W. M. Yen. Low Temp. Phys., **31**, 777 (2005).

[357] D. D. Sell. J. Appl. Phys., **39**, 1030 (1968).

[358] In order to rule out shape effects, [174, 180] we focus our discussion on trends in the rhombohedral nanoparticles only.

[359] That magnon sideband softening trends mirror the size-dependent trends of the absorption difference is a perfect illustration of the common underlying mechanism.

[360] C. E. Patton. Phys. Rep., **103**, 251 (1984).

[361] V. V. Eremenko, Y. G. Litvinenko, and E. V. Matyushkin. Phys. Rep., **132**, 55 (1986).

[362] J. López-Sánchez, A. Serrano, A. Del Campo, M. Abuín, O. Rodríguez de la Fuente, and N. Carmona. Chem. Mater., **28**, 511 (2016).

[363] P. A. Fleury and R. Loudon. Phys. Rev., **166**, 514 (1968).

[364] The shift to higher frequency compared to the bulk value is in agreement with a previous report of magnon hardening in $\alpha$-Fe$_2$O$_3$ nanoparticles, [168] although trends in particles of similar shape have not yet been reported.

[365] Unfortunately, the fundamental excitons are not directly observed in the spectra due to their high directionality and the intrinsic random orientation of the nanoparticles, so no internal check of the trend is available at this time.

[366] M. Popova, A. Sushkov, S. Golubchik, M. Isobe, and Y. Ueda. Physica B, **284-288**, 1617 (2000).

[367] A. S. Krylov, S. N. Sofronova, I. A. Gudim, and A. N. Vtyurin. Solid State Commun., **174**, 26 (2013).

[368] Although the magnetic crossover is observed at low temperatures, our variable temperature measurements show minimal spectral changes down to 4 K, even through the orthorhombic ($Pmma$) to monoclinic ($P2_1/c$) transition takes place between 200 and 100 K. [82] This allows the use of room temperature, high pressure data to understand the low temperature magnetic crossover.

[369] E. Knittle, W. Phillips, and Q. Williams. Phys. Chem. Miner., **28**, 630 (2001).

[370] P. R. Naidu. Aust. J. Chem., **19**, 2393 (1966).

[371] F. D. Hardcastle and I. E. Wachs. J. Raman Spectrosc., **45**, 683 (1990).

[372] D. Cremer, A. Wu, A. Larsson, and E. Kraka. J. Mol. Model., **6**, 396 (2000).

[373] G. Aullón, D. Bellamy, L. Brammer, E. A. Bruton, and A. G. Orpen. Chem. Commun., 653–654 (1998).

[374] The newly formed O-H⋯Cl hydrogen bond decreases the angle of the F⋯H-O exchange pathway, making it even further away from the ideal 180° angle to

support ferromagnetism. This means that the new hydrogen bond pathway must be the driving mechanism of the magnetic crossover.

[375] P. Schobinger-Papamantellos, K. Buschow, and J. Rodríguez-Carvajal. J. Magn. Magn. Mater., **324**, 3709 (2012).

[376] S. B. Roy. J. Phys. Condens. Matter, **25**, 183201 (2013).

[377] J. L. Wang, L. Caron, S. J. Campbell, S. J. Kennedy, M. Hofmann, Z. X. Cheng, M. F. Md Din, A. J. Studer, E. Brück, and S. X. Dou. Phys. Rev. Lett., **110**, 217211 (2013).

[378] It is clearly a lower symmetry subgroup of *Pnma* at 300 K and *P2₁/c* below the structural phase transition temperature [82].

[379] A. Bousseksou, G. Molnár, and G. Matouzenko. Eur. J. Inorg. Chem., 4353–4369 (2004).

[380] J. M. Manriquez, G. T. Yee, R. S. McLean, A. J. Epstein, and J. S. Miller. Science, **252**, 1414 (1991).

[381] W. R. Entley and G. S. Girolami. Science, **268**, 397 (1995).

[382] S. Horiuchi, R. Kumai, and Y. Tokura. J. Am. Chem. Soc., **135**, 4492 (2013).

[383] P. Jain, V. Ramachandran, R. J. Clark, H. D. Zhou, B. H. Toby, N. S. Dalal, H. W. Kroto, and A. K. Cheetham. J. Am. Chem. Soc., **131**, 13625 (2009).

[384] C. Duboc. Chem. Soc. Rev., **45**, 5834 (2016).

[385] P. Jain, A. Stroppa, D. Nabok, A. Marino, A. Rubano, D. Paparo, M. Matsubara, H. Nakotte, M. Fiebig, S. Picozzi, E. S. Choi, A. K. Cheetham, C. Draxl, N. S. Dalal, and V. S. Zapf. npj Quantum Mater., **1**, 16012 (2016).

[386] L. Xin, Z. Fan, G. Li, M. Zhang, Y. Han, J. Wang, K. P. Ong, L. Qin, Y. Zheng, and X. Lou. New J. Chem., **41**, 151 (2017).

[387] A. J. Clune, K. D. Hughey, E. E. Gordon, C.-H. Lee, N. Abhyankar, N. S. Dalal, M.-H. Whangbo, J. Singleton, and J. L. Musfeldt. Magnetic field-temperature phase diagram of multiferroic $[(CH_3)_2NH_2]Mn(HCOO)_3$. In preparation.

[388] F. Ye, S. Chi, J. A. Fernandez-Baca, H. Cao, K.-C. Liang, Y. Wang, B. Lorenz, and C. W. Chu. Phys. Rev. B, **86**, 094429 (2012).

[389] H. J. Silverstein, E. Skoropata, P. M. Sarte, C. Mauws, A. A. Aczel, E. S. Choi, J. van Lierop, C. R. Wiebe, and H. Zhou. Phys. Rev. B, **93**, 054416 (2016).

[390] N. L. Ross, J. Ko, and C. T. Prewitt. Phys. Chem. Miner., **16**, 621 (1989).

[391] J. M. Longo and J. A. Kafalas. J. Solid State Chem., **3**, 429 (971).

[392] R. W. Kedzie, J. R. Shane, M. Kestigian, and W. J. Croft. J. Appl. Phys., **36**, 1195 (1965).

[393] J. L. Manson, Q.-Z. Huang, C. M. Brown, J. W. Lynn, M. B. Stone, J. Singleton, and F. Xiao. Inorg. Chem., **54**, 11897 (2015).

[394] A. C. McConnell, J. D. Bell, and J. S. Miller. Inorg. Chem., **51**, 9978 (2012).

[395] G. Stock and W. Domcke. J. Chem. Phys., **93**, 5496 (1990).

[396] U. Fano. Phys. Rev., **124**, 1866 (1961).

[397] K. Huang and A. Rhys. P. R. Soc. Lond. A Mat., **204**, 406 (1950).

[398] M. J. Rice. Phys. Rev. Lett., **37**, 36 (1976).

[399] M. J. Rice, V. M. Yartsev, and C. S. Jacobsen. Phys. Rev. B, **21**, 3437 (1980).

[400] A. Graja, P. V. Huong, and J. C. Cornut. Solid State Commun., **39**, 929 (1981).

[401] K. N. Boldyrev, T. N. Stanislavchuk, A. A. Sirenko, L. N. Bezmaternykh, and M. N. Popova. Phys. Rev. B, **90**, 121101(R) (2014).

# Vita

Ken O'Neal was born in Medina, Ohio. He attended Baldwin-Wallace University between 2007 and 2010, where he received a B.S. degree majoring in Chemistry. After a year of working at Arnco, Ken joined the research group of Dr. Janice L. Musfeldt in the summer 2011 pursuing his Ph.D. degree in the University of Tennessee. His research focuses on the spectroscopic investigations of nanomaterials and molecule-based magnets. Ken O'Neal received a Doctor of Philosophy Degree in Chemistry from the University of Tennessee in Spring of 2017.